THE UNIVERSITY *of* EDINBURGH

Structural and Magnetic Properties of the Geometrically Frustrated $3d$ and $5d$ $s = \frac{1}{2}$ Double Perovskites Sr_2CuWO_6, Ba_2YWO_6 and $LaSrMgWO_6$

Oliver Burrows

Doctor of Philosophy
The University of Edinburgh
August 2016

Lay Summary of Thesis

With the development of quantum mechanics in the early 20^{th} century, an understanding of the microscopic behaviour of magnetic materials was gained. With the revelations afforded by this discipline, however, came a tendency in some quarters towards a reductionist viewpoint of science: that chemistry was merely physics applied on a larger scale. Similarly, biology was considered by some to be be merely "scaled-up" chemistry, and psychology was simply a consequence of the rules governing biology, applied on the scale of an organism.

Such a simplistic argument ignores the concept of emergent phenomena. This expression refers to the idea that, as systems become more complex, behaviour is observed which *cannot* be predicted by a naïve application of the rules of the more basic system. A simple example of this is can be observed in the spontaneous breaking of symmetry, an effect which is not predicted by quantum mechanics. For instance, as water is cooled through 0 °C (at standard pressure), it undergoes a phase change from liquid, a state with infinite long-range symmetry in all directions, to solid ice: a crystalline state with high symmetry, but less than is observed in water.

This breaking of symmetry is also observed in magnetic materials: at high temperatures, many magnetic materials are paramagnetic - the electron spins of the materials align in a magnetic field, but when the field is removed, thermal energy allows them to orient themselves randomly. As the material is cooled, and drops below a characteristic temperature (known as the Néel temperature, T_N), the electron spins will align antiparallel ("up" and "down") with one another. This is a breaking of symmetry, analogous to that observed in water.

In some materials, the magnetic ions on which these electrons are localised can be arranged such that it is *impossible* for such an antiparallel arrangement of electrons to occur. For instance, on a triangle, it is impossible for all three

nearest-neighbour electrons to be aligned antiparallel with respect to one another: one bond must feature a parallel arrangement of electrons. Because all three bonds are equal, and the two possible states of each spin are of equal energy, this arrangement of atoms leads to a six-fold degeneracy of states, and a geometrically frustrated system. Geometric frustration can suppress the temperature at which symmetry breaking occurs, and give rise to exotic magnetic phenomena, which are often difficult to predict. This thesis studies three such materials through a range of experimental techniques, and attempts to explain the observed phenomena.

Abstract

Double perovskites with a single $s = \frac{1}{2}$ magnetic ion and rocksalt order can show geometric frustration, due to arrangement of electron spins such that they cannot satisfy all nearest-neighbour antiferromagnetic interactions simultaneously. This can give rise to exotic magnetic states at low temperature. Compounds with unpaired $4d$ and $5d$ electrons have in this respect been studied far less than $3d$ compounds. Here, results of studies on the compounds Sr_2CuWO_6, Ba_2YWO_6 and $LaSrMgWO_6$ are presented.

The synthesis of the previously reported compound $Ba_2Y_1WO_6$ ($W_5{}^+$, $5d^1$) was attempted by many methods, but yttrium deficiencies were present in all samples. This led to the series $Ba_2Y_xWO_6$ with $\frac{2}{3} \leq x \leq 0.8$, dependent on the synthesis conditions. The $x = \frac{2}{3}$ compound is known to exist as a metastable cubic phase and an 18H rhombohedral thermodynamic phase. The one-third vacant B sites on the $x = \frac{2}{3}$ cubic material are doped with lithium, resulting in the $Ba_2Y_{2/3}Li_xWO_6$ compound. This thesis focuses on the new $x = 0.75$ phase, and characterises its structural and magnetic properties.

The Jahn-Teller distorted Sr_2CuWO_6, with the Cu^{2+} ($3d^9$) magnetic ion, has an elongated c axis leading to separation of ab planes. This compound had been proposed as a pseudo-2D spin liquid model candidate, following a lack of evidence of transition to long-range order in SQUID magnetometry and heat capacity. However, recent μSR measurements *did* show a transition to long-range ordered state at 24 K. This thesis details further bulk and local probe measurements which indicate that the low-temperature state is type-2 antiferromagnetic, and which point to a thermally activated spin-liquid-like state which occurs between 24 K and ∼100 K.

$La_{0.5}Sr_{1.5}MgWO_6$, has also been synthesised. The 1:1 compound $LaSrMgWO_6$ had previously been reported as W^{5+} and described as "pseudo-cubic": X-ray

and neutron diffraction studies here characterise the low-temperature structure within the $P2_1/n$ monoclinic space group, and suggest that no ordering of the atoms on the A site is observed.

Declaration

I declare that this thesis was composed by myself, that the work contained herein is my own except where explicitly stated otherwise in the text, and that this work has not been submitted for any other degree or professional qualification except as specified.

(*Oliver Burrows, August 2016*)

To my mother, Linda Kathleen Gerrard (1956 – 2005)

Acknowledgements

First of all, I would like to thank my supervisor, Mark de Vries, for providing me with an interesting project, and for his advice and support throughout my Ph.D. I have found my time working with Mark to be extremely rewarding, as he has unfailingly taken the time to discuss ideas with me. We have worked collaboratively and constructively, on occasion exploring areas of the subject which were new to both of us. I would also like to thank my second supervisor, Professor Paul Attfield, for always taking the time to discuss any question I may have had regarding the work I was undertaking, and more general questions relating to the Centre for Science at Extreme Conditions. I would like to express my gratitude to Dr Chris Stock, both for his extremely helpful discussions regarding inelastic neutron scattering experiments, and for his work organising the weekly CSEC seminars, which gave an excellent insight into the wide range of work being carried out at the Centre.

I would also like to acknowledge the friends and colleagues I had the opportunity to meet with in Edinburgh. In particular, I would like to thank Dr Ángel Arévalo López, Dr Lucy Clark, and Dr Alex Sinclair for their friendship and advice throughout my Ph.D.: without them, I am sure that the journey to this point would have been significantly harder. The community of researchers at CSEC was a truly friendly group, with the interdisciplinary nature of the work being undertaken there showing a great deal of exciting research. I am particularly thankful to Dr Martin Mišek for his aid with SQUID experiments at all hours of the day.

I am also grateful to the project students I worked without throughout the course of my Ph.D.: Shabana Ahmed, Ian Bruce-Smith, Richard Duffy, Karl Hope, Dominic Jacobson, and Sarah Morrison. I was fortunate to work alongside so many diligent undergraduate students during my studies, whose efforts and aid in synthesising and characterising these materials are appreciated. I am thankful to all of the members of the wider School of Chemistry with whom I had the pleasure of interacting, including both academic and support staff. Whilst it would be impossible to list everyone here, I would particularly like to thank Denise Wilson, the Postgraduate Research Administrator, who keeps the department running smoothly from the perspective of a Ph.D. student. I would also like to thank the members of the Physical Chemistry Reading Group, for the weekly meetings which kept me abreast of all of the interesting work being carried out in

the School of Chemistry, of which I would otherwise have been unaware. I would like to thank Dr Mat Heal, and his research group Dr Chun Lin, Dr Chris Malley, Dr Riinu Ots, Ksenia Aleksankina, and Hao Wu, for allowing me to pollute their office environment with materials science!

Throughout my studies, I have been extremely fortunate in being granted beam time at both ISIS and ILL. I would like to thank all of the staff at these institutions for their help, and in particular Dr Ross Stewart, Dr Mark telling, Dr Marek Jura, and Dr Kevin Knight at ISIS, and Dr Emmanuelle Suard and Dr Gøran Nilsen at ILL, for all of their assistance in using these instruments. I would also like to thank Dr Finlay Morrison, at the University of St Andrews, for his aid in carrying out dielectric measurements on the various materials synthesised. Although results from these experiments are not presented in this thesis, they gave an interesting introduction to this sort of measurement.

I wish to express my gratitude to the University of Edinburgh and the Engineering and Physical Sciences Research Council for the funding I received throughout my Ph.D., and the Science and Technology Facilities Council and the Insitut Laue-Langevin for the invaluable time I spent using instruments at ISIS and the ILL. Not only did these give me essential data for completing my Ph.D., but I also gained an insight into the many interesting fields of study – outside the specialised world of materials science – which undertake work at these facilities.

From a personal point of view, I would like to thank my father and stepmother, John and Sheila, for their continual support and encouragement, throughout the first three years of my Ph.D., and the subsequent time I have spent writing this thesis. I would also like to thank a close friend, Kevin, for a conversation on a bridge long ago – which first set me on the path to study chemistry at undergraduate level. Finally, I wish to give thanks to three fellow students who have supported me throughout my undergraduate and postgraduate studies. Cicely, Keith and Nathan, I certainly could not have got this far without your friendship, both inside and outside the chemistry department.

Contents

List of Figures

List of Tables

Chapter 1

Introduction

1.1 More is different

In 1972, Philip Anderson wrote that "More is Different" [1]. He refuted the reductionist idea that scientific disciplines can each be thought of as an "applied" version of a simpler system: that chemistry is applied many-body physics, which is in turn applied particle physics, and so on, continuing to the idea that social sciences is simply applied psychology. The reductionist argument ignores the idea of "emergent phenomena": properties of systems which cannot be predicted from the behaviour of less-complicated systems. An example of this is the symmetry breaking observed in the crystallisation of a liquid into a solid. The infinite rotation, translation, reflection and rotational symmetry operations observed in a liquid (on large length scales) are reduced to only those permitted by the specific crystal which is formed: whilst these may be numerous in the case of highly symmetrical systems, they are still less than the infinite symmetry of a liquid.

The "More is Different" argument also applies to microscopic and macroscopic quantum states. Phenomena which occur in systems on a microscopic scale, such as quantum tunnelling, are different from those which occur on a macroscopic scale. Liquid helium is a superfluid, with different physical properties and behaviour from those seen in classical fluids (see Section 1.6). However, since this state is observed only at temperatures below 2.4 K, it is difficult to study the physics of the system. Model systems must therefore be designed in order to examine the emergent phenomena of such a macroscopic quantum system.

One example of such a system is a spin liquid, In classical electronic behaviour, electron spins freeze into a particular arrangement as a sample is cooled: this will normally be ferromagnetic or antiferromagnetic, depending on whether electron spins align parallel or antiparallel with respect to their nearest neighbours.

By carefully designing a system, it is possible to arrange electron spins on a lattice such that antiferromagnetic interactions are favoured over ferromagnetic interactions, and, furthermore, so that antiferromagnetic interactions cannot be simultaneously satisfied with respect to all nearest neighbours. This suppresses the temperature at which the electron spins freeze, and can cause freezing into a number of more exotic states – described below – or even prevent freezing entirely at *any* temperature: a quantum spin liquid.

This thesis will describe efforts to synthesise and study materials which are geometrically frustrated, and present results and conclusions based on these studies.

1.2 Magnetism in solids

1.2.1 Quantum numbers

The four quantum numbers, n, l, m_l and m_s, can be used to describe the state of electrons in an atom [2, 3]. The principal quantum number, n, denotes the principal electron shell, and has integer values greater than or equal to one. The principal quantum number indicates the most probable distance from the nucleus of electrons in that shell; thus, lower values of n indicate lower energy electrons, with $n = 1$ as the ground state. The principal quantum number also affects the maximum value for the orbital angular momentum quantum number, l.

The orbital angular momentum quantum number, l, indicates the subshell of the electrons. This has values between zero and $n - 1$, corresponding to the number of nodes in the orbital. $l = 0$ is an s-orbital, with no nodes; $l = 1$ a p-orbital, with one node; $l = 2$ a d-orbital, with two nodes, and so on. As mentioned above, $\mathbf{L}$ is a vector quantity: the direction component of this arises from the shape of the orbital.

m_l is the magnetic quantum number, with values between $-l$ and $+l$. The number

l	m_l	Orbital
0	0	s
1	0	p_y
	± 1	p_x, p_z[i]
2	0	d_{z^2}
	± 1	d_{xz}, d_{yz}[i]
	± 2	d_{xy}, $d_{x^2-y^2}$[i]

Table 1.1 Possible values of m_l for different l.

Symbol	Name	Permitted values
n	principal quantum number	$n \in \mathbb{N}$, $n \geq 1$
l	orbital angular momentum quantum number	$l \in \mathbb{N}$, $l \leq n-1$
m_l	magnetic quantum number	$m_l \in \mathbb{Z}$, $-l \leq m_l \leq +l$
m_s	spin angular momentum quantum number	$m_s = \pm\frac{1}{2}$

Table 1.2 Quantum numbers [2, 3].

of possible values of m_l is equal to the number of different orbitals for a given l, as shown in Table 1.1.

The spin quantum number m_s has $2s+1$ values between $-s$ and $+s$. Unlike n, l and m_l, these are *not* necessarily integers. For an electron, $s = \frac{1}{2}$, and $m_s = \pm\frac{1}{2}$. These represent the two possible spin orientations of an electron, "spin-up" and "spin-down".

The quantum numbers, and their possible values, are summarised in Table 1.2.

1.2.2 Spin-orbit coupling

In elements with low Z, the interaction between the spin and orbital components of an electron's wavefunction is negligible, and can often be ignored. For elements with higher Z, however, spin-orbit coupling is more significant.

In low-Z elements, the total magnetic moment quantum number, J, is determined as follows:

[i]The wavefunctions for $m_l \neq 0$ are complex. These are therefore combined to generate appropriate real wavefunctions. For $l = 1$, $m_l = \pm 1$ are combined to give the p_x and p_y orbitals. Similarly, for $l = 2$, $m_l = \pm 2$ are combined to give the d_{xy} and $d_{x^2-y^2}$ orbitals, and $m_l = \pm 1$ are combined to give the real d_{xz} and d_{yz} orbitals.

$$J = |L - S| \text{ where the electron shell is less than half full} \quad (1.1)$$
$$J = |L + S| \text{ where the electron shell is more than half full}$$

Where L and S are equivalent to l and s, but refer to the state of the whole syste rather than single electrons. The effects of strong spin-orbit coupling on the magnetic phases observed in geometrically frustrated materials have been studied somewhat, as in the Ir^{4+} ($5d^5$) double perovskites La_2ZnIrO_6 and La_2MgIrO_6 [4], which, like the W^{5+} ($5d^1$) compounds described in this thesis, has $j_{eff} = \frac{1}{2}$. This thesis attempts to continue studies on these strongly spin-orbit coupled materials, specifically Mott insulators, which display insulating behaviour despite the presence of partially-filled bands (see below).

1.2.3 Magnetic moments

The motion of an electron in an atom gives rise to a magnetic moment, μ [2]. This can be described thus:

$$\mu = \gamma \mathbf{L} \quad (1.2)$$

Where γ is the gyromagnetic ratio, a constant linking the magnetic moment and the orbital angular momentum, $\mathbf{L}$. $\mathbf{L}$ is quantised in units of $\hbar$:

$$\mathbf{L}^2 = l\,(l+1)\,\hbar^2 \quad (1.3)$$

where l is the orbital angular momentum quantum number, which takes integer values between 0 and n, the principal quantum number. $\mathbf{L}$ is a vector quantity, with m_l the magnetic quantum number (with integer values $-l \leq m_l \leq +l$) representing the projection of $\mathbf{L}$ along a given axis:

$$L_z = m_l \hbar \quad (1.4)$$

The magnitude of $\mathbf{L}$ is given by

$$|\mathbf{L}| = \sqrt{l\,(l+1)}\,\hbar \tag{1.5}$$

The Bohr magneton, μ_B, is a convenient unit for expressing magnetic moments. It is the magnetic moment which arises from the orbiting of an electron around a hydrogen atom, and can be calculated thus:

$$\mu_B = \frac{e\hbar}{2m_e} = 9.274 \times 10^{-24}\,\mathrm{A\,m^2} \tag{1.6}$$

The component of the magnetic moment associated with the orbital angular momentum which is projected along the z axis is thus (from Equations 1.2-1.6)

$$\mu_z = \gamma L_z = \gamma m_l \hbar = -m_l \mu_B \tag{1.7}$$

with the magnitude of the total magnetic dipole moment [2]:

$$|\mu| = \sqrt{l\,(l+1)}\,\mu_B \tag{1.8}$$

In an applied field, a magnetic moment will have a certain energy, depending on its alignment with respect to that field. The energy is at a minimum when the magnetic moment lies along the direction of the field, and maximised when the magnetic moment is antiparallel to the field. This energy can be given by:

$$E = \mu \cdot \mathbf{B} = -\mu B \cos\theta \tag{1.9}$$

An applied field will also cause precession (with frequency γ) around a cone with internal angle 2θ, known as Larmor precession, analogous to that observed in a gyroscope.

1.2.4 Bulk magnetism

The equations above describe the behaviour of unpaired electrons in isolated atoms. Whilst this is a fundamental introduction, it is important to consider

the behaviour of electrons in bulk solids, where their activity can be physically measured. The magnetic moment per unit volume of such a solid is its magnetisation, $\mathbf{M}$.

In a vacuum, the magnetic flux density $\mathbf{B}$ is related in a linear fashion to an applied field (the vector quantity $\mathbf{H}$) by [2]:

$$\mathbf{B} = \mu_0 \mathbf{H}, \tag{1.10}$$

where μ_0 is the vacuum permeability. In a solid, the relationship is less simple, given by:

$$\mathbf{B} = \mu_0 \left(\mathbf{H} + \mathbf{M} \right), \tag{1.11}$$

and, in the case where magnetisation is directly proportional to magnetic field, the magnetic susceptibility, χ, can be defined:

$$\mathbf{M} = \chi \mathbf{H} \tag{1.12}$$

In this case, Equation 1.11 can be expressed as follows:

$$\mathbf{B} = \mu_0 \left(1 + \chi \right) \mathbf{H} = \mu_0 \mu_r \mathbf{H}, \tag{1.13}$$

where $\mu_r = 1 + \chi$ is the relative permeability of the material.

Macroscopic magnetic arrangements

Bulk solids display diamagnetism and, if they have unpaired electrons, paramagnetism, antiferromagnetism, ferrimagnetism or ferromagnetism (Figure 1.1).

Diamagnetism is the weak repulsive interaction between a closed shell of electrons and a magnetic field. Diamagnetic contributions have been measured for many individual ions; these can be combined additively to estimate the diamagnetic response of any given solid. All materials have a (negative) diamagnetic contribution to their overall magnetic moment; however, in most

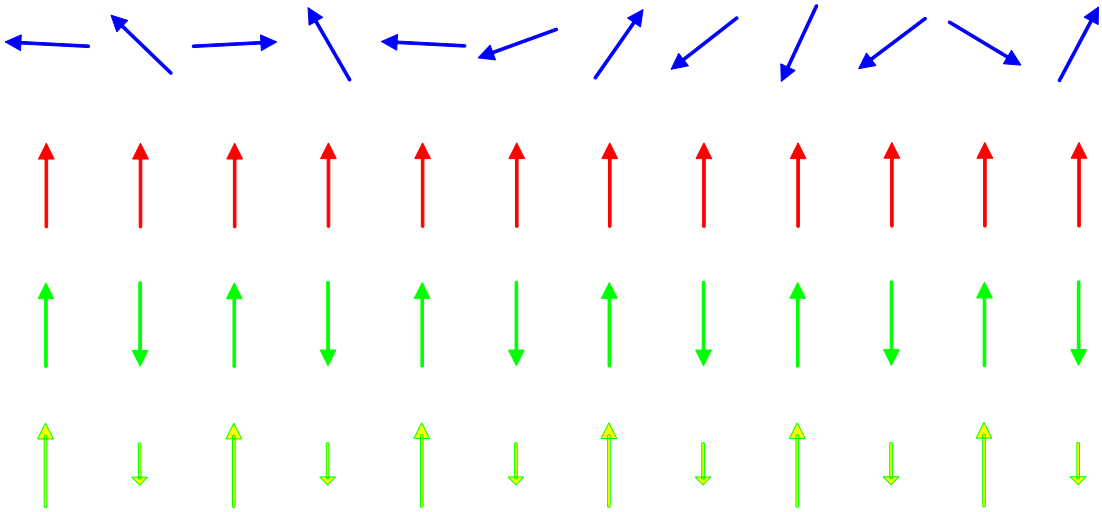

Figure 1.1 Qualitative example of bulk magnetism, showing paramagmetic (top), ferromagnetic (second), antiferromagnetic (third) and ferrimagnetic (bottom) electron spin alignment.

cases this is so small compared to the overall response that it can be neglected.

Paramagnetism is the most common form of magnetic behaviour at room temperature. Unpaired electrons in a paramagnet fluctuate rapidly and randomly in the absence of a magnetic field, due to the weakness of electron spin interactions relative to the temperature of the sample. As the sample is cooled, the electrons will gradually freeze into a different state, depending on the nature of the interactions.

Ferromagnetism occurs in a material with all electron spins aligned in the same direction, giving a net magnetisation even in the absence of a magnetic field. Ferromagnetism can be considered hard or soft: "hard" ferromagnets will retain the magnetisation even in the presence of an applied magnetic field in a different direction; whilst "soft" ferromagnets will easily change the direction of magnetisation. The hardness of a magnet can be determined from a hysteresis loop (Section 1.2.4).

Antiferromagnetism occurs when neighbouring electrons pair up with opposite spin: this results in a reduction of net magnetisation with decreasing temperature, as the two electron spin matrices are equal and opposite.

Ferrimagnetism is similar to antiferromagnetism, in that spins align in opposite directions, but differ in that two magnetic species are present. These could be different elements, or they could be the same element in different oxidation states. The effect of this is that opposing spins do not cancel each other perfectly, as in an antiferromagnet, so a net magnetisation remains present.

The type of magnetism can be determined by Superconducting QUantum Interference Device (SQUID) magnetometry (Section 1.2.4). This shows the behaviour of a sample as a function of temperature in an applied field. Figure 1.2 shows this behaviour qualitatively for a ferromagnet (a) and an antiferromagnet (b). In both cases, the sample is paramagnetic above a certain temperature. In the ferromagnet, this is the Curie temperature T_C: below this temperature the magnetisation rapidly increases, as electron spins align, either along a random axis, along a material-specific "easy axis", or along the direction of any applied field.

Above the Curie temperature, the material is paramagnetic. Here, spins are generally aligned in the direction of the magnetic field, but as the temperature is increased, or the field is reduced, the magnetisation reduces, as spins have enough thermal energy to overcome the cost of fluctuating in non-field-aligned directions.

The antiferromagnet, conversely, shows a *decrease* in magnetisation below the characteristic temperature, called the Néel temperature T_N. This is caused by the alignment of spins in an antiparallel arrangement. As with a ferromagnet, this alignment of spins will persist if the field is removed.

Measurement of the magnetic susceptibility of a material also allows determination of the Weiss constant, θ, for that material (Equation 1.22. In a pure Curie paramagnet, this is equal to zero, whilst ferromagnets have positive θ, and for antiferromagnets, $\theta < 0$ (Figure 1.2).

Measuring magnetic susceptibility

Magnetic susceptibility can be measured on a SQUID. These instruments use a superconducting ring with two Josephson junctions – insulating layers, or "weak links" – within the ring. A DC current is passed through the ring, and a magnetic field H applied to the sample. As the sample is moved through the SQUID ring (from below the centre of the ring to above it), a change in the current flowing through the ring is induced.

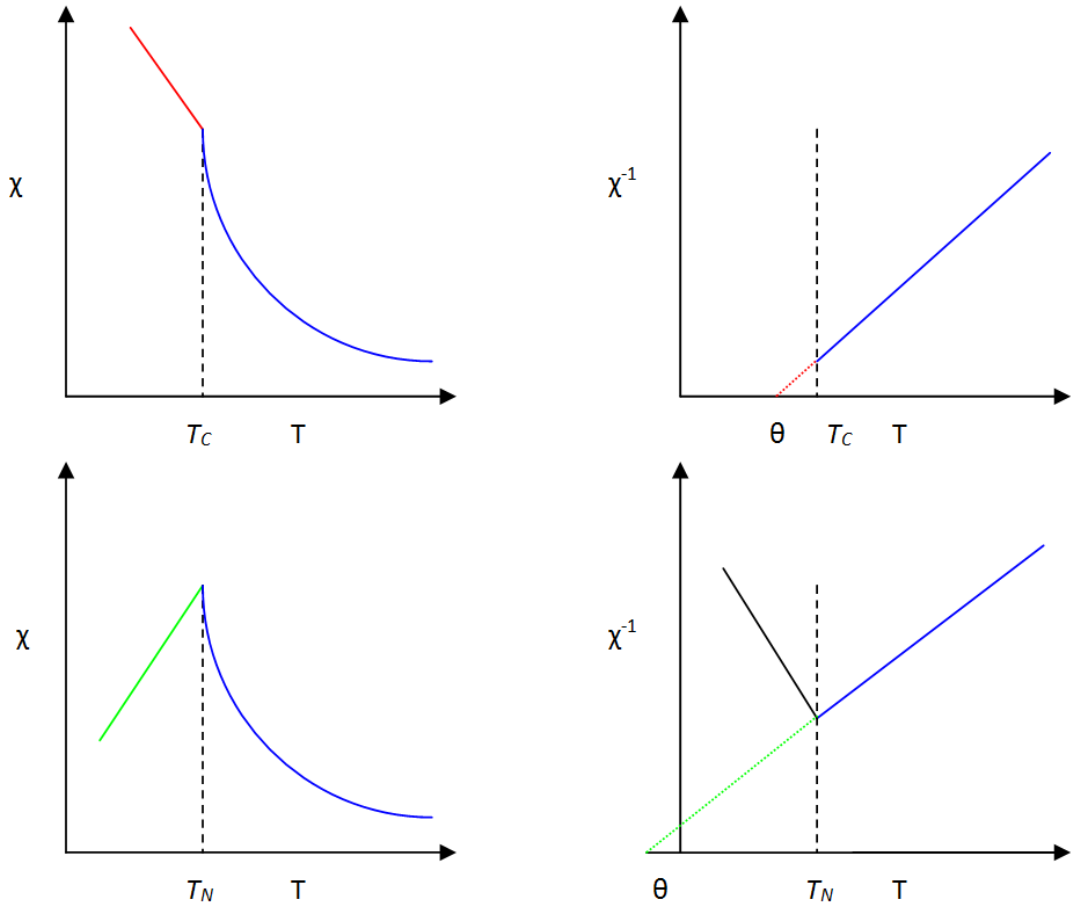

Figure 1.2 Qualitative example of (left) magnetic susceptibilty and (right) inverse magnetic susceptibilty measurements for (top) a ferromagnetic, and (bottom) an antiferromagnetic material.

This change in current is detected by the SQUID, and converted to a voltage which is proportional to the magnetic moment of the sample. The magnetisation M, of the sample is proportional to the magnetic moment, allowing the calculation of the magnetic susceptibility:

$$\mathrm{M} = \chi \mathrm{H} \tag{1.14}$$

In a paramagnetic sample, magnetic susceptibility is inversely proportional to temperature. This behaviour can be approximated by Curie's Law [2]:

$$\chi = \frac{C}{T} \tag{1.15}$$

Where C is the Curie constant. This can be derived from a semiclassical treatment of paramagnetism.

As described in Equation 1.9, the energy of a magnetic moment pointing at an angle θ to an applied field $\mathbf{B}$ (which will be considered here to be the z axis) is $-\mu B \cos\theta$, and the degree of the moment projected along z is $\mu B \cos\theta$. On a sphere with unit radius, the proportion of magnetic moments pointing at an angle between θ and $\theta + \mathrm{d}\theta$ is, by geometric consideration of the sphere, $\frac{1}{2}\sin\theta \mathrm{d}\theta$ (the area of the annulus, $2\pi \sin\theta$, divided by the surface area of the unit sphere, 4π.) (Figure 1.3).

From the statistical probability of a moment aligning itself at random at an angle θ, and the energy – from which the Boltzmann expression $e^{\frac{\mu B \cos\theta}{k_B T}}$ can be derived – the overall moment along $\mathbf{B}$ is [2]:

$$\begin{aligned} \langle \mu_z \rangle &= \frac{\int_0^\pi \mu \cos\theta e^{\frac{\mu B \cos\theta}{k_B T}} \frac{1}{2}\sin\theta \mathrm{d}\theta}{\int_0^\pi e^{\frac{\mu B \cos\theta}{k_B T}} \frac{1}{2}\sin\theta \mathrm{d}\theta} \\ &= \mu \frac{\int_{-1}^1 x e^{xy} \mathrm{d}x}{\int_{-1}^1 e^{xy} \mathrm{d}x} \end{aligned} \tag{1.16}$$

where $x = \cos\theta$ and $y = \frac{\mu B}{k_B T}$.

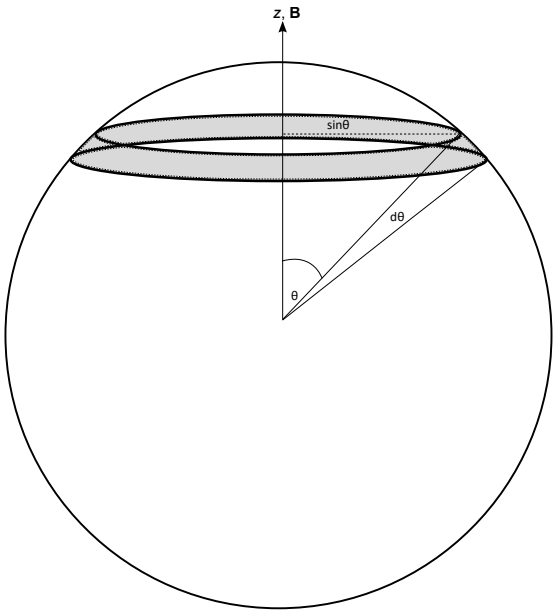

Figure 1.3 The statistical probability of a moment aligning between an angle θ and $\theta + \mathrm{d}\theta$ is given by the ratio of the area of the annulus, $2\pi \sin\theta \mathrm{d}\theta$ to the surface area of the unit sphere, 4π

From this, we can write the Langevin function:

$$\frac{\langle \mu \rangle}{\mu} = \coth y - \frac{1}{y} \equiv L(y) \tag{1.17}$$

At small y – where the field is small or temperature is large – this can be approximated with the following Taylor expansion[ii]

$$\coth y = \frac{1}{y} + \frac{y}{3} + O(y^3) \tag{1.18}$$

and thus,

$$L(y) = \frac{y}{3} + Oy^3 \tag{1.19}$$

Finally, the saturation magnetisation, M_S, is the magnetisation obtained when all magnetic moments are aligned, equal to $n\mu$ where n is the number of magnetic

[ii]Where $O(y^3)$ indicates that y^3 is the dominant term.

moments. The *obtained* magnetisation, M, is equal to $n\langle\mu_z\rangle$. Consequently,

$$\frac{M}{M_S} = \frac{\langle\mu_z\rangle}{\mu} \approx \frac{y}{3} = \frac{\mu B}{3k_B T} \tag{1.20}$$

Since, in small fields, $\chi = \frac{M}{H} \approx \mu_0 \frac{M}{B}$,

$$\chi = \frac{n\mu_0\mu^2}{3k_B T} = \frac{C}{T} \tag{1.21}$$

which is Curie's Law.

As can be seen from the derivation, this assumes independent, non-interacting magnetic moments. However, in many materials that is not the case. Where ferromagnetic or antiferromagnetic behaviour are observed, electrons are interacting with one another. In this case, an additional term, the Weiss constant θ is required:

$$\chi = \frac{C}{T - \theta} \tag{1.22}$$

In a paramagnet, $\theta = 0$; in a ferromagnet, $\theta > 0$, and in an antiferromagnet, $\theta < 0$ – as shown in Figure 1.2.

1.2.5 Goodenough-Kanamori superexchange

The nature of magnetic interactions between unpaired electrons in a dilute system – one in which not every atom has unpaired electrons – is governed by the Goodenough-Kanamori superexchange rules [5–7]. These are a simple set of rules which allow prediction of the interaction, based on the orbitals in which electrons are present. Figure 1.4 shows the basic rules for superexchange. Electrons in orbitals with good overlap will couple antiferromagnetically (a). Electrons in the same orbital must have opposite spin, by the Pauli exclusion principle [8]. Electrons in orbitals with orthogonal overlap will couple ferromagnetically (d). Electrons can also couple *within* an ion, for instance between a p_x and a p_y orbital on an oxygen: this allows 90° coupling (c).

In a magnetically active ion, one or more electrons will be unpaired: for instance, W^{5+} has a single unpaired electron in the $3d$ orbital set: specifically, when the

tungsten is octahedrally co-ordinated, the electron will sit in one of the t_{2g} orbitals which point between the x, y and z axes. As shown in Figure 1.4 e), the electron can interact with those of a neighbouring (non-magnetic) oxygen anion: in the case of this system, the interaction continues with a 90° angle to its nearest-neighbour W^{5+}, and antiferromagnetic coupling between the two ions is predicted.

1.3 Geometric frustration

At high enough temperatures, paramagnetism is observed for all magnetic compounds: at this point, the thermal energy present is high enough to overcome any energetic advantage gained by electron spin ordering to a macroscopic antiferromagnetic, ferromagnetic, or ferrimagnetic arrangement. As the temperature is lowered, a material approaches its ordering temperature – the Néel temperature in the case of antiferromagnetic materials, and Curie temperature in the case of ferromagnetic materials – below which spontaneous ordering occurs. This transition from the highly symmetric paramagnetic state to the ordered state, of lower symmetry, is known as *symmetry breaking*. As mentioned in Section 1.1, this is a process which cannot be explained by simple consideration of single-particle systems: it is an emergent phenomenon only observed in macroscopic measurements.

The Goodenough Kanamori rules detailed above describe a process for determining the alignment of electron spins in a given compound. However, it is naïve to assume that this is the whole picture, as many systems cannot be categorised so simply. A theoretical triangle of magnetic ions, in which electrons are expected to couple antiferromagnetically, will swiftly demonstrate the impossibility of using Goodenough-Kanamori superexchange to explain all electron spin alignments, as Figure 1.5 demonstrates.

A system in which superexchange rules cannot all be simultaneously satisfied is said to be *frustrated*. This can arise due to the positioning of atoms on a lattice, or due to competing nearest- and next-nearest-neighbour interactions. For instance, if three ions, each with a single unpaired electron, are placed on the corners of a triangle, it is impossible for them all to align antiferromagnetically with respect to one another: there will always be one nearest-neighbour interaction which is unsatisfied (Figure 1.5). This interaction could occur on any of the three sides of the triangle; since each electron spin can be either up or down, there are six

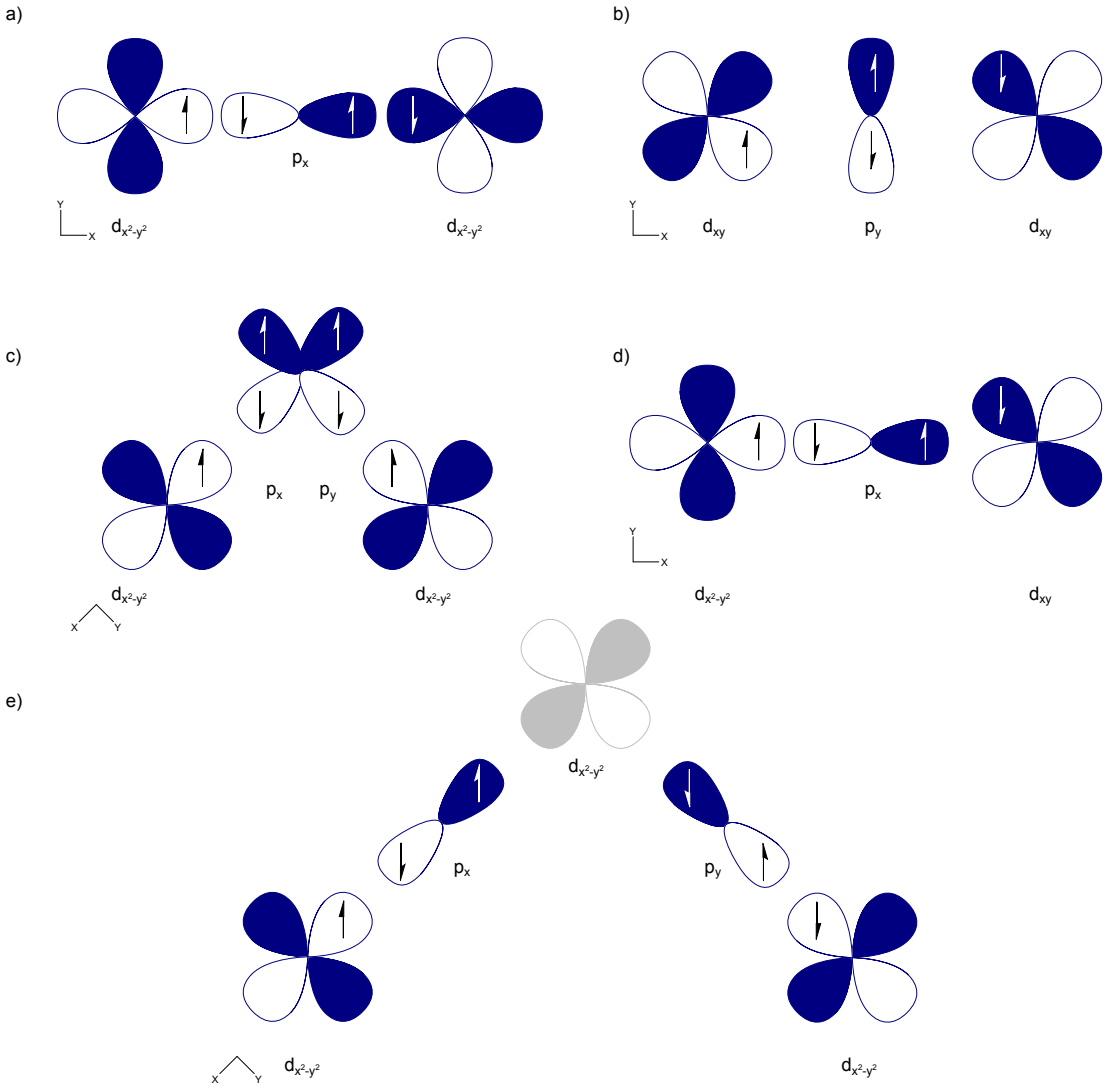

Figure 1.4 Goodenough-Kanamori superexchange. a) Superexchange between two e_g orbitals via an intermediate p orbital. b) Superexchange between two t_2g orbitals via an intermediate p orbital. c) Superexchange between two e_g orbitals via two intermediate p orbitals on one atom, at a 90° angle. d) Superexchange between an e_g and a t_2g orbital, via an intermediate p orbital. e) Superexchange between two e_g orbitals, via two intermediate atoms, with a non-magnetic (and non-participating) metal ion shown in grey. In coupling such as in c), ferromagnetic interactions are predicted; in all other situations, antiferromagnetic coupling is expected.

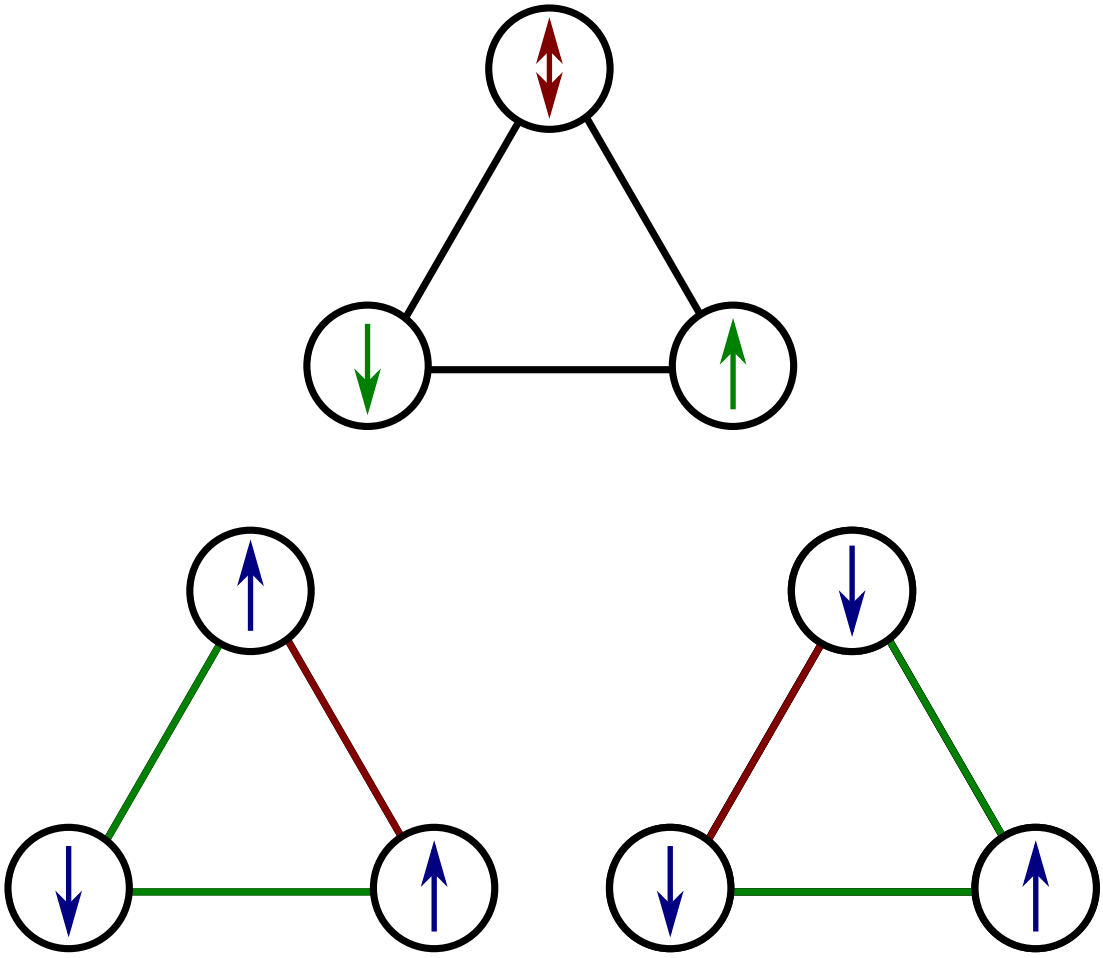

Figure 1.5 Demonstration of geometric frustration on a triangle. The top diagram shows two antiferromagnetically ordered electrons (green), whilst the third (red) cannot align antiferromagnetically with respect to both. Below, the results of the third electron aligning spin-up (left) and spin-down (right) are shown: in each case, two bonds are satisfied (green), whilst a third (red) is unsatisfied.

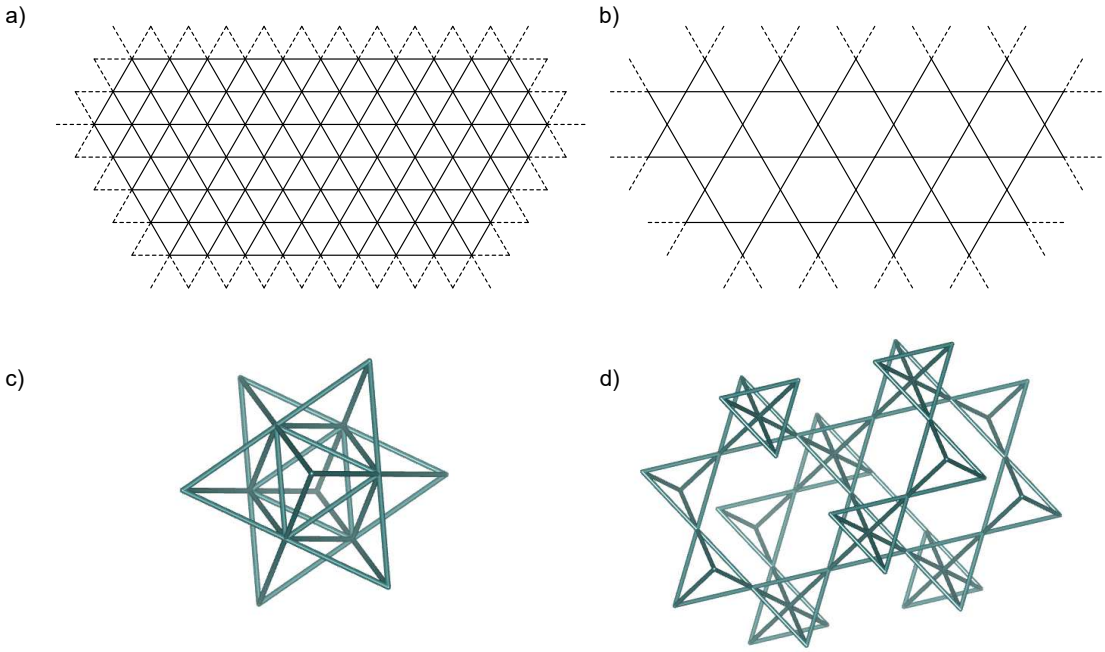

Figure 1.6 Two-dimensional triangle (a) and kagome (b) frustrated lattices, and the three-dimensional perovskite (c) and pyrochlore (d) equivalents.

degenerate spin configurations. As the number of atoms in this example increases, so too does the number of degenerate states. Figure 1.6 shows the extension of this in two and three dimensions.

With *four* magnetic ions, arranged on the corners of a tetrahedron, a similar conflict occurs: two of the six edges cannot be satisfied, leading to *twenty-four*-fold degeneracy on each tetrahedron. As with the two-dimensional system, this can be extended to a network of edge-sharing or corner-sharing tetrahedra – lattices which are seen in double perovskites (Figure 1.6 c)) and pyrochlores (Figure 1.6 d)) respectively – with a very large number of degenerate states.

Geometric frustration can also take place on a square lattice, where nearest-neighbour and next-nearest-neighbour interactions are of similar strength. This is discussed in detail in Chapter 3.

This high number of degenerate states leads to a suppression of the symmetry breaking temperature of the material, resulting in exotic magnetic states. In the extreme, this results in complete suppression of the freezing of spins, resulting in dynamic fluctuations down to $T = 0\,\mathrm{K}$: this is known as a *quantum spin liquid*. In other cases, disordered states with a high degree of degeneracy can be observed: these are all discussed in more detail below.

1.3.1 Quantifying frustration

One effect of the large degree of degeneracy is a lowering of the temperature at which spins freeze: this allows a quantitative value for the level of frustration to be calculated. If magnetometry data are fitted to a Curie-Weiss model (Section 1.2):

$$\chi = \frac{C}{T - \theta} \tag{1.23}$$

where χ is the magnetic susceptibility, C is the Curie constant, T is temperature, and θ is the Weiss temperature, the frustration can be defined as [9]:

$$f = \frac{|\theta|}{T_N} \tag{1.24}$$

Where T_N is the Néel freezing point of the system. In a non-frustrated antiferromagnet, $T_\theta = -T_N$ and $f = 1$; in a frustrated system, T_θ could be on the order of negative hundreds of kelvin, whilst T_N is only 80 K. Thus, a value for $f > 10$ can indicate strong frustration in a magnetic material; however, it should be noted that this value may be misleading in 1D and 2D systems, where T_N may be suppressed by thermal fluctuations, rather than frustration.

On a large scale, the degree of degeneracy can be calculated from [10]:

$$D = F - K \tag{1.25}$$

Where the terms have the values given in Table 1.3. This gives rise to an expression for the degree of over- or under-constraint of a given system:

$$\frac{D}{N} = \frac{q\,(n-1)}{b} - n \tag{1.26}$$

Again, the meanings of terms are given in Table 1.3. Where $\frac{D}{N} > 0$, a system is said to be underconstrained: there are fewer constraints than there are degrees of freedom, and consequently degeneracy is expected. In contrast, a compound with $\frac{D}{N} < 0$ is overconstrained, and no degeneracy is expected on a macroscopic scale.

Term	Value
D	Degeneracy of the ground state of the system
F	Degrees of freedom of the system
K	Constraints required to keep the system in the ground state
N	Number of building blocks (triangles, tetrahedra)
q	Number of shared sites per block
n	Degrees of freedom of each site
b	Number of blocks each shared site is shared between

Table 1.3 Terms for macroscopic degeneracy in systems.

1.3.2 Exotic magnetic states arising due to frustration

As described above, the existence of a geometrically frustrated lattice leads to a very large number of degenerate ground states for a magnetic material. This leads to a wide range of possible macroscopic magnetic ground states, depending on the strength of the interactions between the magnetic ions, and the geometry of the system.

As has been shown above, geometric frustration means that it is *impossible* for all electron spin interactions to be satisfied. The system must therefore adopt a compromise state. Depending on the precise nature of the electron spin interactions – including the strength of interactions, the geometric arrangement of spins, and the presence of any impurities on the magnetic sites of the lattice – this can take a wide variety of forms.

In 1973, Anderson proposed the existence of a "resonating valence bond" state [11]. In such a state, electrons are delocalised over the compound in a similar manner to those first proposed in the structure of benzene proposed by Kekule [12, 13].

Quantum spin liquid

As mentioned previously, a quantum spin liquid is a system with complete suppression of freezing of electron spins down to the lowest measured temperatures (on the order of tens of millikelvin). This has been proposed as the ground state of compounds such as herbertsmithite, a kagomé-lattice system with the composition $ZnCu_3(OH)_6Cl_2$ [14, 15]. The first proposed spin liquid was in the Mott-insulating organic compound ($\varkappa$-$(BEDT-TTF)_2Cu_2(CN)_3$) [16]:

a compound studied by ^{1}H NMR spectroscopy and found to have no long-range magnetic order down to a temperature of 32 mK.

Thermal spin liquid

A "thermal spin liquid", as described in Chapter 3, is a system in which electron spins are dynamic above a transition temperature, with correlation length decreasing as a function of temperature to an upper bound, above which no correlation is seen, and a paramagnetic magnetic state is observed. In Sr_2CuWO_6, these correlations are three dimensional. Below the transition temperature, type-2 antiferromagnetism is observed in Sr_2CuWO_6.

Valence bond crystal

In a valence bond solid, neighbouring spins pair up in an ordered fashion, forming a regular array of $s = 0$ spin pairs. Valence bond crystals have been suggested as the ground state for the hexagonal lattice compound $CuAl(AsO_4)O$ [17].

Valence bond glass

Here, electrons pair into $s = 0$ pairs, as seen in a valence bond solid; however, the pairing is random, rather than ordered. This system therefore has a large number of degenerate states. A consequence of the random pairing of electrons is that a fraction will be left without neighbours with which they can couple. This leads to a dispersion of unpaired "dangling" spins throughout the compound. This has been proposed as the ground state of Ba_2YMoO_6, a double perovskite with Mo^{5+} magnetic ions on a network of edge-sharing tetrahedra [18–20].

Valence bond liquid

A valence bond liquid, proposed for the honeycomb compound Li_2RuO_3 [21], features local, covalently-bonded spin-singlet states which persist above the transition temperature for the material. No ordering was observed in Li_2RuO_3 above a transition temperature of ~ 543 K, but ordering *was* observed on rapid cooling below that temperature: it was this observation which led the authors to

conclude that the persistent valence bonds were "liquid", rather than glassy in nature.

Spin glass

Similar to a valence bond glass, a spin glass has a large degree of degeneracy due to a random arrangement of static spins. Unlike a valence bond glass, however, there is no pairing up of adjacent spins – resulting in a truly random arrangement.

Spin ice

Spin ices have been observed in pyrochlores: compounds with a network of corner-sharing tetrahedra, such as $Ho_2Ti_2O_7$ [22]. Spin ices are so called due to their similarity with the structural features of water ice. Water ice has a network of hydrogen bonds, with each oxygen anion tetrahedrally co-ordinated by four hydrogen ions: two covalently bonded, and two hydrogen bonded. If the mid-points between neighbouring oxygen atoms are connected, a network of corner-sharing tetrahedra is formed: due to the difference in length of covalent bonds and hydrogen bonds, each hydrogen is slightly offset from the vertex of a tetrahedron, with two inside each tetrahedron, and two outside (Figure 1.7). In a spin ice, the easy axis for each electron spin is along the vector from the centre to the vertex of its tetrahedron. Each tetrahedron will have two electron spins pointing inwards, and two pointing out, analogous to the two-in, two-out arrangement of hydrogen atoms studied in water ice.

1.4 Band and Mott insulators

When two atoms bond to form a molecule, their atomic orbitals combine to form two discrete molecular orbitals: one bonding, and one anti-bonding. As increasing numbers of atoms combine, the number of molecular orbitals increases, and the gap between them decreases, as shown in Fugre 1.8. In the limit where a solid is formed, the orbitals form a continuous band, with a high degree of degeneracy in the middle of the energy band. As a result, in a solid with a partially filled band (i.e., a metal), electrons are free to move: this leads to conducting activity. Conversely, band insulators are those materials in which both the valence band

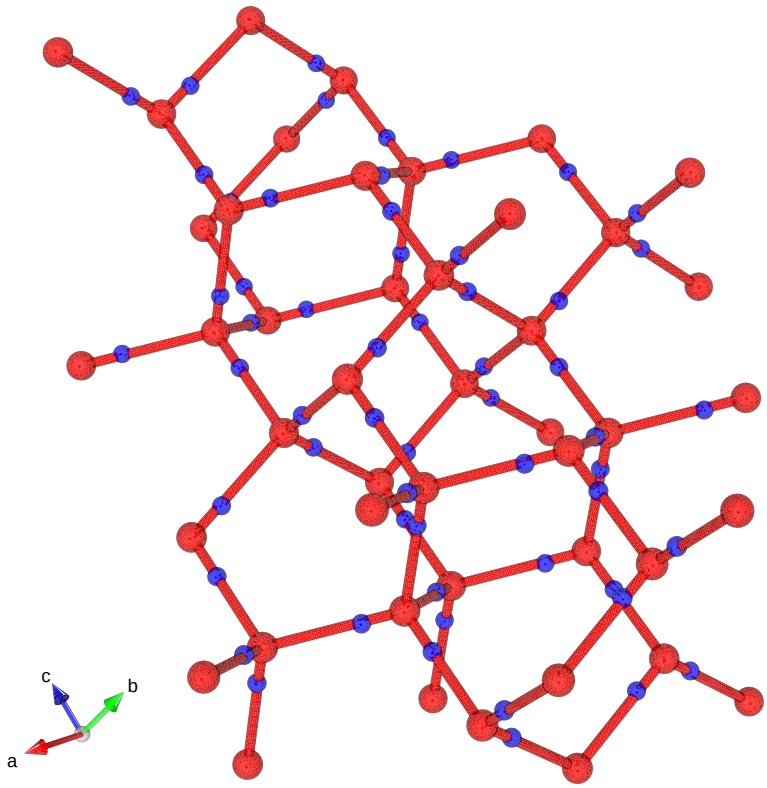

Figure 1.7 In water ice, each oxygen (red) ion is tetrahedrally bonded to four hydrogen ions (blue). Two of the bonds are close covalent bonds, and two are long hydrogen bonds. This leads to a large degree of degeneracy in the possible formation of ice. A similar phenomenon is seen in *spin* ices, where each magnetic ion has two electron spins pointing towards it, and two pointing away. As with water ice, this results in high degeneracy of states.

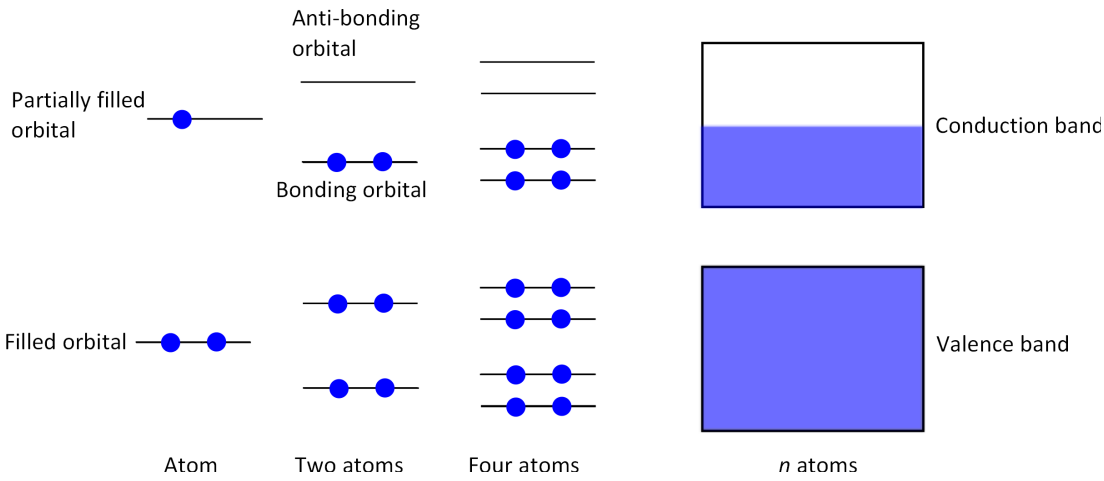

Figure 1.8 As increasing numbers of atoms bond in a solid, the energy gaps between adjacent orbitals decreases. In the limit, this becomes a continous band, with many degenerate states.

is full, and the conduction band is empty: in this case, there is an energy cost to electron movement. This can be overcome by exciting electrons from the valence band to the conduction band, leading to an increase in conductivity in band insulators with increasing temperature (in contrast to conductors, which show a *decrease* in conductivity with increasing temperature).

In some compounds, however, conducting behaviour is not observed, despite the presence of partially filled bands. High Coulomb repulsion between electrons in these compounds leads to an energy cost to having two electrons in the same orbital, reducing electron mobility and leading to insulating behaviour. A material which is expected to be a conductor by band theory, but which instead acts as an insulator, is known as a Mott Insulator [23, 24]. Spin-orbit coupling can act in concert with this to increase the localisation (Figure 1.9) [25]: in such a case, it is not accurate to speak of conduction and valence bands, as the high degree of localisation of electrons prevents the formation of these structures.

1.5 Double perovskites

The mineral perovskite, $CaTiO_3$, was discovered in 1839 by Gustav Rose [26]. The perovskite structure, ABO_3, consists of a transition metal ion surrounded by six oxygen ions, in octahedral co-ordination, with the A-site ion – typically an alkaline earth ion – located in the gaps between the octahedra (Figure 1.10).

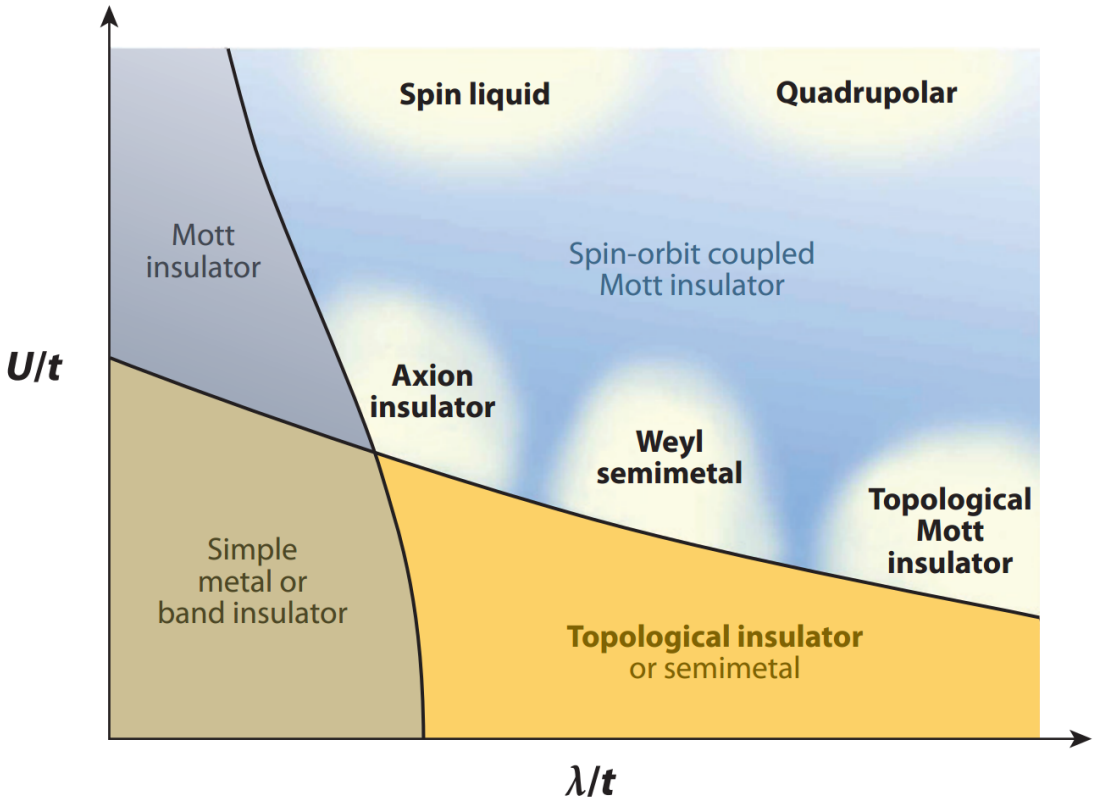

Figure 1.9 Sketch of a phase diagram for electronic materials, expressed in terms of the spin-orbit coupling (λ/t) and electron-electron repulsion (U/t). Figure from [25].

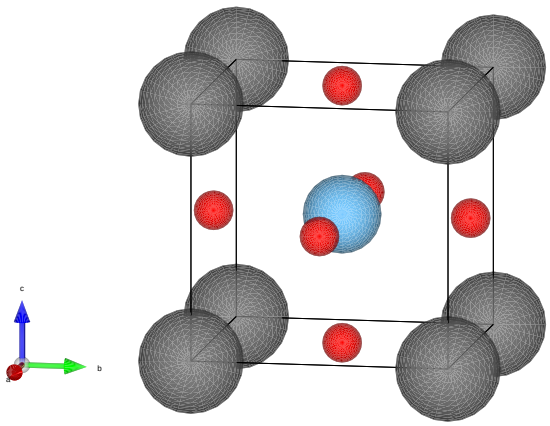

Figure 1.10 The perovskite structure. The B-site ion, in blue, sits in the centre of an ochtahedron of red oxygen anions. A-site ions (grey) occupy the insterstitial sites.

Double perovskites have the general formula $ABB'O_6$, where the A-site ion is typically once again an alkaline earth metal, but the B site is occupied by two distinct transition metal ions. Most commonly, these will be different elements, as in the well studied compound $SrFeMoO_6$, which displays collosal magnetoresistance at room temperature [27]. Compounds with B-sites distinguished by two ions of the same metal but different oxidation states have also been reported, however, such as $Ba_2Bi^{3+}Bi^{5+}O_6$ [28].

The general formula of double perovskites gives a clue as to the flexibility of their composition. The A and B sites can be occupied by a large number of different ions – and, in some cases, by *no* ions – giving rise to a vast number of different structures, whose structural and magnetic properties are dependent on their constituent ions and the interactions between them.

1.5.1 Structural distortions in double perovskites

As in single perovskites, the most simple unit cell of a double perovskite is cubic $Pm\overline{3}m$, with the B site randomly occupied by each of the possible ions. Often, however, a degree of ordering will be seen on the site, particularly if there is a large difference in size (greater than 0.26 Å) or charge (greater than two oxidation numbers) between the two sites [29, 30]. The most common arrangement of B-site ions is rocksalt ordering – though other patterns, such as columnar or lamellar ordering, have also been observed [31]. A more thorough exploration of ordering in double perovskites can be found in Chapter 5. A rocksalt-ordered double perovskite with no octahedral tilting (see below) will have a doubling of the unit cell in each direction (compared to a single perovskite), and space group $Fm\overline{3}m$.

Octahedral tilting

Distortions from the cubic structure are frequently observed. An indication of the likelihood of deviation (in both double and single perovskites) can be found from the Goldschmidt tolerance factor, which is a simple geometric calculation based on the relative sizes of the constituent ions [32]:

$$t = \frac{r_A + r_O}{\sqrt{2} \times \left(\frac{r_B}{2} + \frac{r_{B'}}{2} + r_O\right)}, \tag{1.27}$$

where r_n is the radius of ion n. This yields a value for t of one for a double perovskite which is expected to be cubic, with deviations above or below indicating a propensity for distortions from this high-symmetry structure. These distortions are caused by co-ordinated tilting of the BO_6 and $B'O_6$ octahedra, in order to accommodate larger or smaller ions into the interstitial sites.

The tilting of octahedra, and the effect of this tilting on the overall unit cell, has been described in detail by Glazer [33]. Each octahedron can rotate along the a, b and c axes of the unit cell, and looking along a given axis, in-phase or out-of-phase tilting can occur. Tilting along a given axis will be of the same angle for each octahedron, but may be the same *or* different angles as the tilting along different axes. This gives rise to a relatively simply notation to describe the nature of tilting within a structure. Each axis a, b and c is describes in terms of the angle of tilt, and whether the tilt is in-phase or out-of-phase. For instance, a compound with tilting $a^+b^+c^+$ demonstrates in-phase tilting along all three axes, leading to a compound with the orthorhombic space group $Immm$.

Where tilting along different axes occurs to the same degree, the axis label can be re-used. Thus, $a^+a^+a^+$ describes a compound with the same angle of in-phase tilting in each direction – leading to a unit cell which retains cubic symmetry, but is of the less symmetrical $Im\overline{3}$ space group.

The possibly variations can give rise to 23 distinct tilt systems, which are described in further detail in [33], with examples of double perovskites which display these systems.

Jahn-Teller effect

The Jahn-Teller effect arises in compounds with unpaired, degenerate d-orbital electrons. Is such systems, the degeneracy can be lifted by lengthening of either the equatorial or axial bonds. If the axial bonds are lengthened (known as an elongation distortion), orbitals with a z component will be lower in energy, due to a decreased overlap with the ligand orbitals (Figure 1.11). Conversely, orbitals which are solely within the xy plane will increase in energy, due to increased overlap with the ligand orbitals. The opposite is true in compound with lengthened equatorial bonds (known as a compression distortion).

Jahn-Teller distortions will only occur where a degeneracy would otherwise be observed: these are in compounds with electron configurations d^1, d^2, d^4, d^5

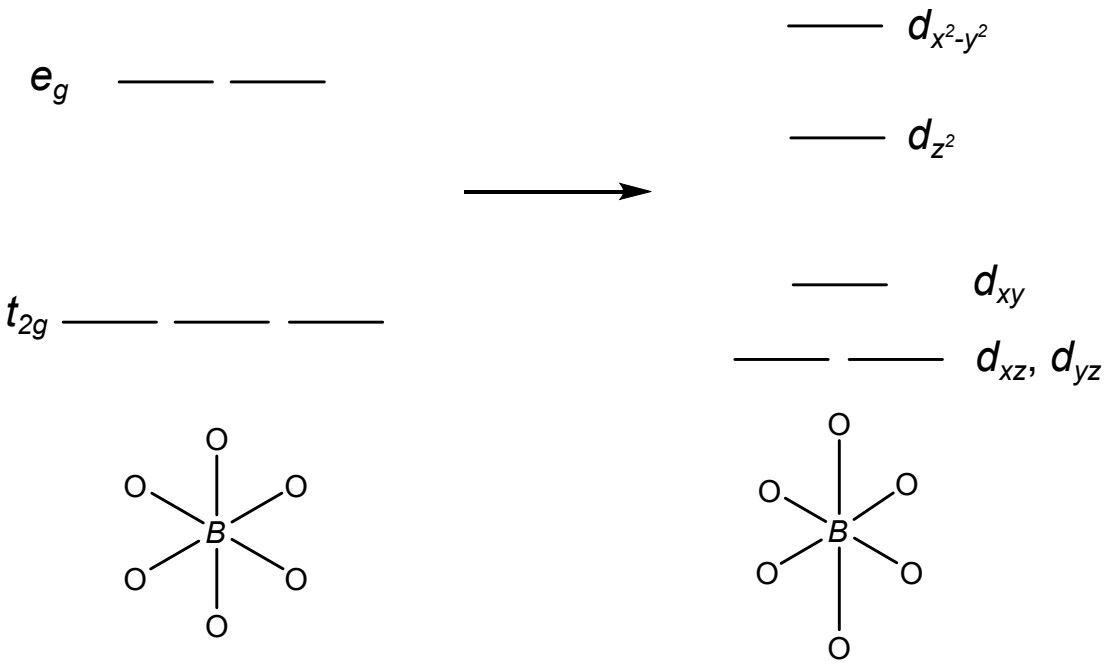

Figure 1.11 An elongation Jahn-Teller distortion gives rise to longer axial bonds and shorter equatorial bonds, resulting in lower energy for those d orbitals with a component in the z axis.

(low-spin only), d^6 (high-spin only), d^7, and d^9. Those compounds in which the degeneracy lies in the e_g orbital set tend to exhibit stronger Jahn-Teller distortions, due to the greater energy savings arising from distortion in this set.

Variable occupancies of A and B sites

Due to the flexibility of the perovskite structure, allowing for different elements of variable oxidation states, it is possible to synthesis a compound which is under-occupied on either the A or B site, leading to vacancies in the lattice structure. As discussed in detail in Chapter 4, vacancies can be either ordered or disordered: where vacancies order, this leads to a rhombohedral, layered structure.

Tungsten bronzes have the formula A_xWO_3, where A is an alkali metal, and $0 \leq x \leq 1$ [34]. This leads to vacancies in the (often non-cubic) perovskite structure and a mixed V/VI oxidation state of tungsten. One consequence of this is that superconductivity has been observed for sodium, potassium, caesium and rubidium tungsten bronzes, with critical temperatures up to 2.1 K [35, 36]. "Doping" the B-sites of the double perovskite structure with vacancies was therefore considered a route towards interesting behaviour: Chapter 4 shows some of the results of (initially unintentional) vacancy-doping of the Y site in

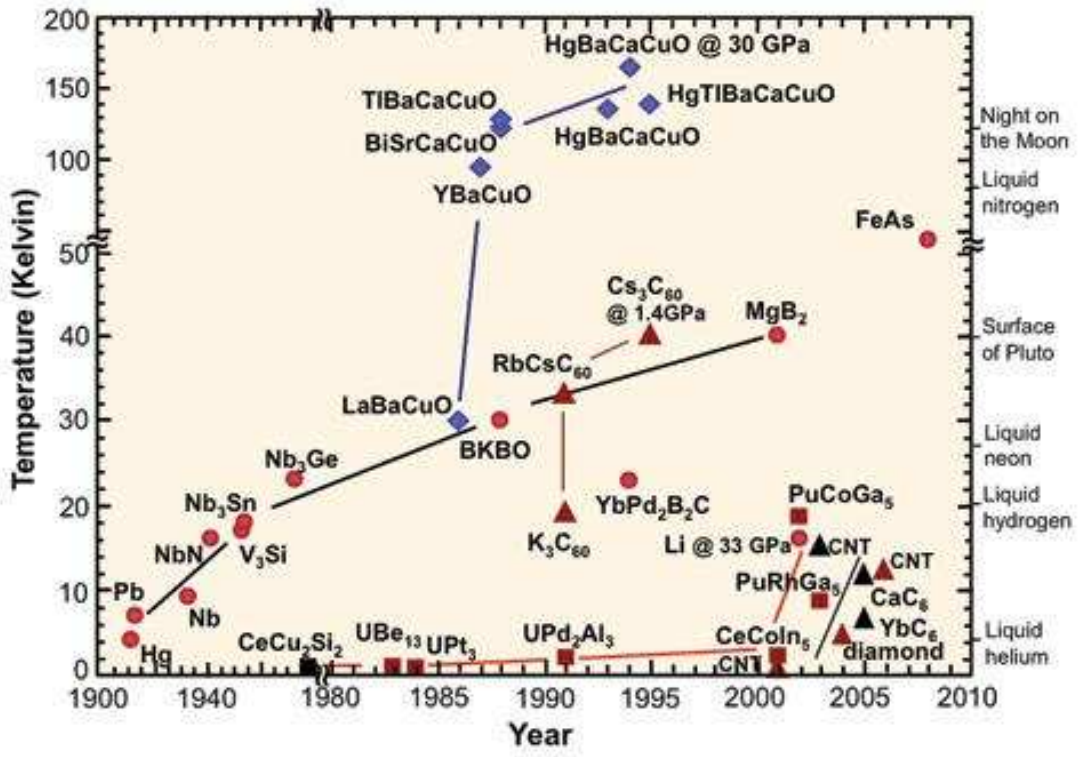

Figure 1.12 Since 1911, the critical temperature for superconductors has increased from 4.2 K in solid Hg to 134 K in HgBaCaCuO at 30 GPa. Image from [38]

Ba_2YWO_6.

1.6 Superconductivity

Although none of the compounds studied in this thesis exhibit superconducting behaviour, a very brief overview of the phenomenon is worthwhile, as an understanding of the mechanism is one of the overarching goals in this field of research.

Superconductivity was first discovered in solid mercury in 1911 by Heike Kamerlingh Onnes [37], and is a property with numerous applications today. Currently, superconductors are widely used in the fields of science, medicine and engineering; their usefulness is limited by the critical temperature of the superconducting material, T_c. Figure 1.12 shows the advance in critical temperature of superconductors between 1911 and 2010.

The mechanism of superconductivity at low temperature – below about 40 K – is governed by BCS theory (named for its discoverers, Bardeen, Cooper and Schrieffer) [39]. This theory posits the formation of ground-state electron pairs through electron-phonon interactions within a solid, leading to an energy gap for excitations: this energy gap means that low-energy excitations, such as electron scattering, are forbidden, resulting in superconducting behaviour.

Due to the energy scale of the electron-electron interactions, thermal excitations in the compound will break these interactions. A maximum theoretical temperature of around 40 K is therefore present: above this temperature, superconductivity must be caused by a different mechanism.

At cryogenic temperatures, helium displays superfluid behaviour through the formation of a Bose-Einstein condensate: a state of matter in which many bosons (such as helium-4 atoms) occupy the ground state [40, 41]. This has parallels to the idea of paired electrons occupying the ground state: indeed, helium-3, a much less abundant isotope of helium – is a fermion (as are electrons), and so can form a Bose-Einstein condensate only through pairing of ^{3}He atoms: this occurs through the mechanism described by BCS theory, at significantly lower temperatures than are observed in helium-4 superfluidity (2.491 mK for ^{3}He versus 2.17 K for ^{4}He).

The parallels between superfluidity and superconductivity make superfluids an interesting subject of study, in order to better understand superconductivity. Such an understanding would lead towards more intelligent, mechanism-driven design for high-temperature superconductors.

Quantum spin liquids, mentioned above in Section 1.3.2, are analogous in many ways to superfluids: they are the ground state of a material, with no ordering breaking of symmetry. Thus, suppressing the temperature at which symmetry is broken in a magnetic structure – by introducing geometric frustration to the material – may encourage the formation of quantum spin liquids. The aims of this thesis, therefore, were to gain a better understanding of symmetry breaking in geometrically frustrated double perovskites, leading to the formation of exotic magnetic states, in the ultimate hope of furthering understanding of the process which occur under these conditions.

Chapter 2

Analytical techniques

2.1 Diffraction studies

Diffraction of a beam of particles by matter is an important analytical technique, allowing determine of structural, magnetic, and dynamic properties of a sample. Two key techniques are discussed here: X-ray and neutron diffraction. The first of these is a simple bench-top technique, requiring little preparation save the synthesis of the sample. Neutron diffraction, on the other hand, requires the use of large-scale facilities (such as ISIS at the STFC Rutherford Appleton Laboratory (RAL) or the Institute Laue-Langevin (ILL)) which must be booked months in advance. These two methods complement each other, offering different insights into the physics of a sample.

Large-scale facilities also exist for the production of X-rays (Diamond at RAL, for instance): these are a great deal more intense than bench-top experiments, and have many uses which will not be covered here.

2.1.1 Physics of diffraction

Diffraction occurs due to the interaction between an incoming photon or neutron and regularly spaced atoms within a lattice. In the case of X-ray diffraction, the incoming photon interacts with the electron cloud of an atom, via the electromagnetic force. In neutron diffraction, the interaction is via the strong nuclear force, and occurs with the nucleus of an atom. Neutrons also have a

magnetic moment, so are able to interact with unpaired electrons in a sample. Thus, neutron diffraction is commonly used in the study of magnetism within a sample.

On encountering at atoms, an incoming particle is scattered. This results in a change in the velocity of the particle, from $\mathbf{k_i}$ to $\mathbf{k_f}$, which can be expressed as

$$Q = k_f - k_i, \tag{2.1}$$

where $\mathbf{Q}$ is the scattering vector. In an elastic scattering experiment, $|k_i| = |k_f|$; only the angle varies. $\mathbf{Q}$ can therefore be expressed solely in term of its magnitude, Q, with unit Å^{-1}. This is shown graphically in Figure 2.1 (top). The angle 2θ is also shown in this diagram: this is the scattering angle, and is commonly used to report diffraction results. Unlike Q, θ is dependent on wavelength. For this reason, Q is preferred when comparing results from different experiments. The two are linked mathematically by:

$$Q = \frac{4\pi \sin(\theta)}{\lambda} \tag{2.2}$$

Thus, different wavelengths can be used to probe different regions of Q, with long wavelengths resulting in lower Q and the examination of longer length scales, whilst shorter wavelengths provide high-resolution data at short length scales.

2.1.2 X-ray diffraction

X-rays are a form of electromagnetic radiation with a wavelength between 10 pm and 10 nm. Those used for X-ray diffraction are on the order of a few angstroms, which corresponds to the inter-atomic distance in crystalline solids. X-rays for diffraction are generated on a bench-top scale by the impact of electrons on a copper target. This produces Cu $K_\alpha 1$ radiation, with wavelength $\lambda = 1.5405\,\text{Å}$

X-ray diffraction took place on a Brucker D2 Phaser diffractometer, working in Bragg-Brentano (flat plate) geometry. Samples were on the order of 100 mg, powdered, and placed on a glass plate. Diffraction patterns were taken from 5° or 10° to 70°, in 0.03° intervals, with 0.5 s at each step.

X-rays interact with electron orbitals, rather than atomic nuclei. A consequence

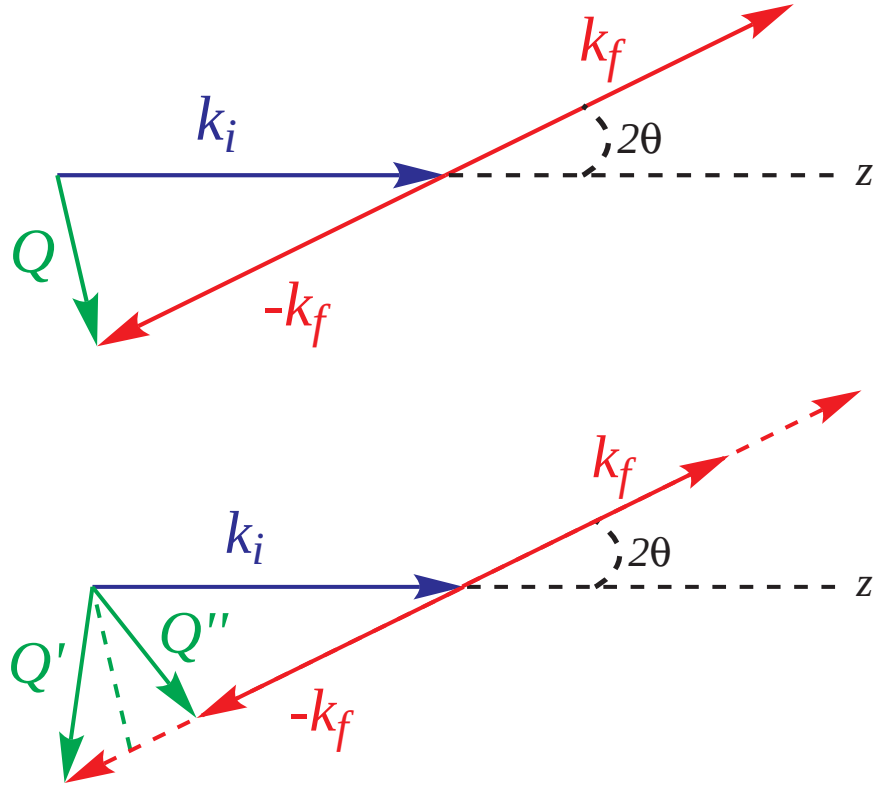

Figure 2.1 Scattering vector Q in (top) elastic and (bottom) inelastic neutron scattering. Elastic scattering has $|k_f| = |k_i|$, whilst in inelastic neutron scattering, $|k_f| \neq |k_i|$. In both cases, $Q = k_i - k_f$. Q' is the scattering vector where the neutron has gained energy from the sample, whilst Q'' is the scattering vector where energy has been lost from the incident neutron to the sample.

of this is that atoms with a high atomic number, Z, scatter X-rays more readily than do those of a lower atomic number: this means that refinement of parameters relating to atoms of low atomic number – such as O^{2-} in the perovskites discussed in this thesis – cannot be accurately carried out using bench-top instruments. In order to refine such parameters, synchrotron sources such as Diamond at RAL are required: these produce photon beams of extremely high intensity, allowing small differences to be discerned.

Another consequence of the interaction between X-rays and electron orbitals is that many more scattering events occur for a given mass of sample: this is a simple result of the larger scattering area of an electron cloud compared to a nucleus. As a result, X-ray diffraction patterns can be obtained in a relatively short space of time (on the order of 15 to 30 minutes for a simple pattern to check phase purity).

Finally, because X-rays interact with a large cloud, rather than a point, the intensity of diffraction decreases at higher angle. This is a consequence of the Fourier transform of a large scattering object.

The atomic form factor for X-rays, then, as a function of the wavelength λ and angle θ is:

$$f(\lambda, \theta) = Z \cdot g(Q) \cdot r_e \tag{2.3}$$

where Z is the atomic number, $g(Q)$ is a decaying function characteristic to each element, with a value of 1 at $Q = 0$ and tending towards zero as $Q \to \infty$, and r_e is the radius of an electron, 2.818×10^{-15} m [42].

2.1.3 Neutron scattering

Neutrons for scattering are produced in two ways: either by spallation, or through nuclear fission. Spallation sources, such as the ISIS experimental facility at RAL, work through the production of a stream of H^- ions, which are accelerated to $\sim 0.37c$ (the speed of light, $c \approx 3.00 \times 10^8\,\mathrm{m\,s^{-1}}$) in a linear accelerator, grouped into pulses, then injected into a synchrotron, where they are stripped of their electrons and further accelerated. This results in a stream of protons travelling at $\sim 0.84c$. A heavy metal target (tungsten at ISIS) in one of the two target

stations is then bombarded by these protons, producing pulses of neutrons by evaporation of neutrons from nuclei following spallation (the neutrons produced directly by spallation are of too high energy to be moderated effectively). The temperature of the target is moderated to 300 K, and neutrons can be further moderated to lower their temperature, depending on the desired energy.

Continuous neutron sources use nuclear fission to generate neutrons from enriched uranium. A typical decay reaction is [42]:

$$\mathrm{n} + {}^{235}\mathrm{U} \rightarrow {}^{236}\mathrm{U}\cdot \rightarrow {}^{134}\mathrm{Xe} + {}^{100}\mathrm{Sr} + 2\mathrm{n} \tag{2.4}$$

There are many different mechanisms, which together yield (on average) 2.5 neutrons per initial collision: this results in a self-sustaining continuous flow of neutrons. These neutrons have very high energy, so are collided with light atoms before being moderated in a similar manner to those produced by spallation sources.

By the de Broglie equation:

$$\lambda = \frac{h}{mv}, \tag{2.5}$$

where h is Planck's constant, 6.626×10^{-34} J s, and mv is the momentum of the particle (mass $\times$ velocity). Thus:

$$E = \frac{1}{2}mv^2 = \frac{h^2}{2m\lambda^2} \tag{2.6}$$

and, since for a particle

$$E = k_B T, \tag{2.7}$$

the desired wavelength of an incident neutron can be linked to its temperature. Moderators are therefore used to affect the temperature and wavelength of the neutrons. The moderators available at ISIS are water ($T = 300$ K; $\lambda = 1.77$ Å), liquid methane ($T = 100$ K; $\lambda = 3.08$ Å) and liquid hydrogen ($T = 20$ K; $\lambda = 6.89$ Å). Thus, neutrons and beamlines can be selected depending on the experimental conditions desired.

Elastic neutron diffraction

Elastic neutron diffraction is similar to X-ray diffraction, in that the incident particles (neutrons, rather than the photons in X-rays) interact with the atoms of a substance. However, neutrons interact with nuclei, rather than electrons. This results in an erratic change in intensity of scattering between elements, and indeed between different isotopes of the same element. Therefore, neutron diffraction can be used to determine the locations of light atoms far more easily than X-ray diffraction.

The nucleus of an atom is point like, whereas the electron cloud is much larger. Because the intensity of scattering as a function of angle is linked to the Fourier transform of the matrix of scattering objects, this point charge sees no decrease in structural form factor as a function of Q. Neutron diffraction data can therefore be collected to much higher Q than can X-ray data, resulting in better resolution of structures.

Neutrons possess a magnetic moment. As a result, they can interact with the magnetic moments in a sample. This interaction allows determination of static magnetic structure at appropriate temperatures, and also magnetic excitations through inelastic scattering (see below). Because magnetism is a result of the electrons in a sample, the magnetic form factor *does* decay at high angle.

Inelastic neutron scattering

Inelastic scattering arises when a transfer of energy occurs between incident neutron and the sample being studied. As a result, incident and scattered neutrons have different energies. A time-of-flight experiment allows this difference in energy to be measured by a change in speed: neutrons which have lost energy to the sample will be slower than those scattered elastically. This is shown in Figure 2.1 (bottom).

As discussed above, neutrons have energy on the order of meV, making them well suited to probing dynamic excitations: inelastic neutron scattering takes advantage of this to probe phonons and spin excitations within a sample.

2.1.4 Rietveld refinement

Rietveld refinement is a mathematical technique for refining X-ray and neutron powder diffraction data [43]. When diffraction patterns of powdered samples are measured, information on the orientation of the infinitely many crystallites present in the sample is lost. As a result, multiple sets of Miller indices may cause different peaks to occur at the same value of Q. Rietveld refinement uses a least-squares method to calculate expected intensity at all Q for a given model unit cell: this allows refinement of a model to the correct structure, for given instrument and sample parameters.

The least-squares function, M, to be minimised by Rietveld refinement is:

$$M = \sum_i W_i \left\{ y_i(\text{obs}) - \frac{1}{c} y_i(\text{calc}) \right\}^2 , \tag{2.8}$$

where $\sum_i$ is the sum over all independent observations, $y_i(\text{obs})$ and $y_i(\text{calc})$ are the observed and calculated intensities, respectively, and c is a scaling factor ($y_i(\text{calc}) = c \cdot y_i(\text{obs})$).

From this, a parameter for the quality of fit, R, can be defined:

$$R_{\text{profile}} = 100 \times \frac{\sum_i \left\{ y_i^2(\text{obs}) - \frac{1}{c} y_i^2(\text{calc}) \right\}}{\sum_i y_i^2(\text{obs})} \tag{2.9}$$

2.2 Magnetic susceptibility measurements

An overview of the theory of SQUID magnetometry was given in Section 1.2.4. All measurements described here took place on a Quantum Design Magnetic Properties Measurement System (MPMS) XL SQUID magnetometer, which can measure DC magnetisation in fields up to 7 T, over a temperature range 2 K to 400 K. Details of the treatment of each data set are given in individual chapters.

2.3 Heat capacity measurements

Heat capacity, C is the amount of heat, U, needed to effect a change in temperature, T, of a material. At constant pressure, p:

$$C_p = \left(\frac{\Delta U}{\Delta T}\right)_p \tag{2.10}$$

In order to measure heat capacity, heat is added to the sample via a puck at constant power for a period of time τ, and then allowed to cool for the same period of time. The resulting increase then decrease in temperature is monitored over time, and can be expressed in the case where there is good thermal contact between sample and puck as:

$$C_{\text{Total}}\frac{\delta T}{\delta t} = K_w(T - T_b) + P(t) \tag{2.11}$$

where K_w is the thermal conductance of the supporting wires, T_b is the temperature of the puck, and $P(t)$ is the heater power over time: this is constant (and non-zero) during the heating part, and zero during the cooling part.

This equation can be fitted to an exponential function, with τ equal to $\frac{C_{\text{Total}}}{K_w}$. This allows extraction of C_{Total}, which is the total heat capacity of the puck assembly.

When taking heat capacity measurements, the puck with a small amount of thermally conducting grease is first measured: this is the addenda, and can be subtracted from a subsequent measurement with the sample affixed to the puck, in order to give just the heat capacity of the sample. This is an extensive property, so must be divided by the number of moles of sample to give the intensive C_v (heat capacity for constant volume), in units of $\mathrm{J\,K^{-1}\,mol^{-1}}$.

From heat capacity, entropic quantities can be determined. Referring to Equation 2.10, taking small intervals:

$$C_p = \frac{\delta U}{\delta T} = \frac{\delta U}{\delta S} \cdot \frac{\delta S}{\delta T} = T\frac{\delta S}{\delta T} \tag{2.12}$$

Therefore,

$$\frac{C_p}{T} = \frac{\delta S}{\delta T} \tag{2.13}$$

Hence, a plot of $\frac{C_p}{T}$ vs T can be integrated, yielding the entropy of a system:

$$\int_0^T \frac{C_p}{T}\mathrm{dT} = \int_0^T \frac{\delta S}{\delta T}\mathrm{dT} = \Delta S \tag{2.14}$$

Heat capacity was measured on a Quantum Design Physical Property Measurement System (PPMS), which can measure at temperatures from 2 K to 300 K in fields up to 90 kOe.

2.4 Muon spin relaxation

Muons are unstable elementary particles, with average lifetime 2.20 µs [44]. Positive muons are generated at the ISIS neutron source by the impact of a proton beam (see above for information on the generation of a proton beam at ISIS) on a graphite target:

$$\begin{aligned} \mathrm{p}^+ + \mathrm{p}^+ &\rightarrow \mathrm{p}^+ + \mathrm{n} + \pi^+ \text{ or} \\ \mathrm{p}^+ + \mathrm{n} &\rightarrow \mathrm{n} + \mathrm{n} + \pi^+ \\ \pi^+ &\xrightarrow{t_{1/2}=26\,\mathrm{ns}} \mu^+ + \nu_\mu \end{aligned} \tag{2.15}$$

See Table 2.1 for explanation of the symbols used. This results in the formation of a beam of polarised muons, whose spin moments are aligned antiparallel to their momentum [45]. These muons impact upon the sample to be studied, coming to rest in environments which can be calculated: generally in areas of high electron density.

Muons in a sample will undergo Larmor precession: the rate of precession of each muon is determined by the local field which it experiences. When a muon decays, it produces a positron and two neutrinos. The direction of positron ejection is preferentially along the vector of the muon spin at the time of decay: this then

p^+	proton
n	neutron
π^+	positive pion
μ^+	positive muon
ν_μ	muon neutrino
e^+	positron
ν_e	electron neutrino
$\overline{\nu}_\mu$	muon antineutrino

Table 2.1 Subatomic and elementary particles.

impacts upon a positron detector, either in front of or behind the sample.

$$\mu^+ \xrightarrow{t_{1/2}=1.52\,\mu s} e^+ + \nu_e + \overline{\nu}_\mu \tag{2.16}$$

The asymmetry between counts on the forward and backward detectors is expressed as:

$$A(t) = \frac{B(t) - \alpha F(t)}{B(t) + \alpha F(t)} \tag{2.17}$$

Where $A(t)$ is the asymmetry at time t, $F(t)$ and $B(t)$ are the counts on the forward and backward detectors, respectively, and α is a calibration factor dependent on sample geometry and the sensitivities of the forward and backward detectors.

The asymmetry can be expressed in terms of muon polarisation:

$$P_z = \frac{A(t) - A_{\mathrm{bg}}}{A(0) - A_{\mathrm{bg}}} \tag{2.18}$$

Where A_{bg} is the background asymmetry.

A field can be applied to the sample, either transverse or longitudinal with respect to muon polarisation. Zero-field experiments can also be used, as described in Chapter 3. The polarisation can then be fitted to various decay functions, depending on the nature of the magnetic environments within the sample.

Due to the large number of muons and the pulsed source at MUSR, polarisation

can be measured with good statistical certainty up to long timescales - on the order of 16 µs. This contrasts with continuous muon sources, such as at the Paul Scherrer Institute (PSI), which allow analysis of muons at short timescales with very high resolution.

2.5 Data analysis tools

X-ray and neutron diffraction data were refined using the GSAS/ExpGUI [46, 47] software packages. Heat capacity data, magnetometry data, muon spin relaxation, and inelastic neutron scattering data were fitted to models using the LMFit package for IPython [48], and plotted in Grace [49].

Chapter 3

Thermal Spin Liquid in the Double Perovskite Sr_2CuWO_6

A paper based on this Chapter has been submitted for publication to Physical Review B. Neutron refinements of the magnetic space group detailed here were carried out by Gøran J. Nilsen.

3.1 Introduction

Double perovskite Mott-Hubbard insulators have attracted much attention because of the interesting, often geometrically frustrated, magnetic topologies and orbital degrees of freedom associated with high symmetry of the magnetic metal-ion environment [50]. This includes for example the cubic rocksalt-ordered double perovskites modelling fcc-lattice antiferromagnets with spin-orbital moments arising from Mo^{5+}, Ru^{6+}, Re^{6+}, Os^{7+} and W^{5+} [25]. Against this backdrop the double perovskites Ba_2CuWO_6 and Sr_2CuWO_6 [51] provide model systems with perhaps by now reassuringly familiar antiferromagnetically-coupled Cu^{2+} $J = S = 1/2$ spin moments, the W cations being in the nominally non-magnetic 6+ state [51–53]. Ba_2CuWO_6 has previously been shown to have a long-range ordered Néel ground state with $T_N = 28\,\mathrm{K}$ [54], but because of the absence of any anomaly or field-cooled zero-field cooled splittings in the magnetic susceptibility Sr_2CuWO_6 was put forward as a potential quantum spin liquid [53].

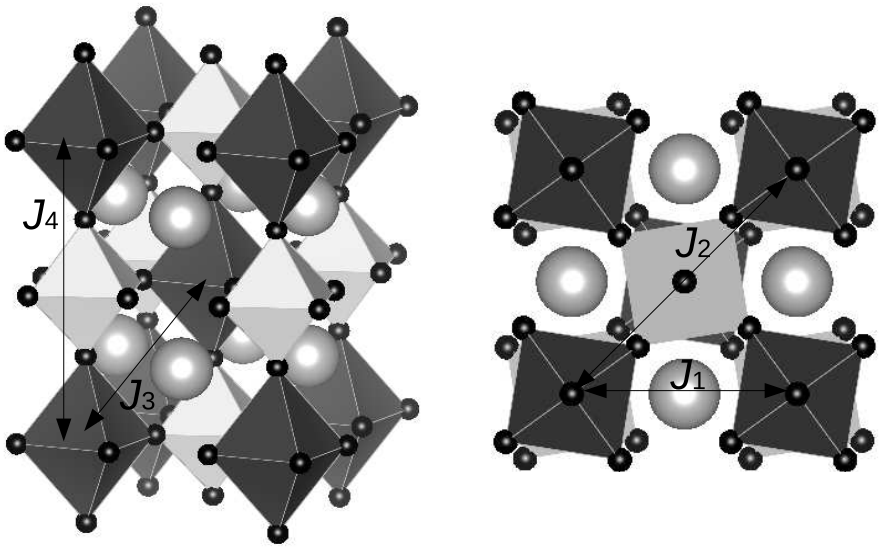

Figure 3.1 The Sr_2CuWO_6structure as seen from the side (c-axis pointing up) and from the top (along the c-axis). The arrows labelled $J_1 \ldots J_4$ are the exchange pathways as described in the text. J_1 coincides with the a-axis (= b-axis) and J_4 coincides with the c-axis.

Sr_2CuWO_6 undergoes a Jahn-Teller distortion from cubic ($Fm\bar{3}m$) to tetragonal (I4/mmm) at 920 °C, leading to an elongation of the c-axis ($c/a\sqrt{2} = 1.1$ for the body-centered tetragonal cell) [52]. At 670 °C there is a further transition from I4/mmm to I4/m with a modest rotation of the octahedra around the c-axis, leading to the structure shown in Figure 3.1. Subsequent studies on the magnetic properties of Sr_2CuWO_6 have focussed on the I4/m phase. The magnetic Cu(II) $d_{x^2-y^2}$ orbital is aligned in the a-b plane, causing some anisotropy between the in-plane and out-of-plane exchange constants. Figure 3.1 shows the four most important exchange interaction pathways; J_1 and J_3 are via Cu-O-O-Cu (90°) bonds in-plane and out-of plane respectively. J_2 and J_4 are via the Cu-O-W-O-Cu (180°) pathways in the a-b plane and along the c-axis, respectively. As remarked earlier [53], there is potential for geometrical frustration due to competing interactions along the different pathways. A recent μSR experiment has shown that there is long-range order below $T_N = 24\,\mathrm{K}$ [55], roughly an order of magnitude below the Weiss temperature. In the same study the exchange constants are estimated using DFT calculations combined with O K-edge X-ray absorption spectroscopy yielding (strongest first) $J_2 = -7.47\,\mathrm{meV}$, $J_4 = -4.21\,\mathrm{meV}$, $J_1 = -1.2\,\mathrm{meV}$ and $J_3 = -0.03\,\mathrm{meV}$ [55]. While this is at first sight consistent with the crystallographic structure, the implied 3D antiferromagnetism is difficult to reconcile with the magnetic properties which have previously been suggested to point to quasi-2D magnetism [55].

The Mermin-Wagner theorem [56] forbids magnetic ordering for $T > 0$ for any layered system where the interactions between $S = 1/2$ spins are strictly in the plane and short-ranged. In the case of the 2D square lattice of $S = 1/2$ spins with antiferromagnetic near-neighbour interactions the $T = 0$ ground state is expected to be long-range (Néel) ordered [57] and in all known cases a 3D Néel-ordered state sets in at some finite temperature due to 3D interlayer interactions, which are often orders of magnitude smaller than the dominant in-plane exchange interactions [58]. Reduced ordered moments due to quantum fluctuations have been observed in physical realisations including copperformate-tetradeuterate (CFTD) [59]. The spin-wave dispersion exhibits distinctive non-classical features indicative of emergent $S = 1/2$ quasiparticle excitations [60]. Furthermore, in many of these systems, including La_2CuO_4 [58], $Sr_2CuO_2Cl_2$ [61] and CFTD [62], strong dynamic correlations have been found to persist far above the ordering temperature. Long-ranged 2D dynamic correlations in the a-b planes, above T_N, could explain the absence of any clear signatures of Néel ordering in the bulk magnetism in Sr_2CuWO_6 [55].

To resolve the disparity between expected and observed magnetic properties, we studied the ground state magnetic structure and characterised the dynamics and magnetic correlations in the temperature range above the magnetic ordering transition and the Curie-Weiss regime. Heat capacity data was collected as a function of temperature to determine the entropy release at the Néel ordering transition.

3.2 Experimental details

Sr_2CuWO_6 was synthesised using standard solid state techniques. Stoichiometric quantities of $SrCO_3$, CuO and WO_3 were ground in an agate mortar in air, before being pressed into a pellet and calcined at 900 °C for two hours in air. The resulting compound was re-pelleted, then sintered at 1200 °C in air for 12 hours. Powder X-ray diffraction was used to identify the compound, and the sintering step was repeated until phase purity was achieved.

DC magnetic susceptibility measurements took place on a Quantum Design MPMS between 2 K and 400 K. Magnetization was measured as a function of temperature at a range of fields up to 7 T.

Heat capacity was measured on a Quantum Design PPMS, at temperatures between 2 K and 300 K with 0.2 K steps between 20 K and 30 K. A thin square pellet (1.5 mm by 1.5 mm, mass 9.5 mg) of sintered $Sr_2CuWO_6$was affixed using Apiezon N grease (Dow Corning). The heat capacity of the grease alone was measured prior to the heat capacity of sample and grease, so that the heat capacity of the small sample could be obtained.

High-resolution neutron diffraction took place in the D2B beamline at the ILL on a sample in a cylindrical vanadium can (internal diameter: 9.20 mm). At 3.5 K the neutron diffraction data collected at wavelengths 1.594 Å (germanium monochromator [335] reflection) and 2.398 Å ([331] reflection) were refined together. At 50 K a wavelength of 2.398 Å was used, and at 298 K, 1.594 Å.

X-ray and neutron diffraction data were refined using the GSAS/ExpGUI [46, 47] software. Magnetic analysis of neutron diffraction was carried out using Fullprof and MatLab [63].

Muon spin relaxation spectroscopy took place on the MuSR beamline at ISIS. Powdered sample was placed in a disc-shaped holder, and measured across a range of temperatures from 1.92 |kelvin to 199 K and longitudinal fields from 0 G to 200 G. Measurements for data presented here were taken for 38.4 million muon events in each case.

Inelastic neutron spectroscopy measurements took place on the MARI beamline at ISIS on a 60 g sample. The sample was placed in an aluminium foil envelope, which was rolled into annular configuration and placed in an aluminium can. The incident energy was 30 meV, and measurements were taken at temperatures between 5 K and 200 K.

3.3 Results

3.3.1 Bulk measurements

Magnetometry measurements indicate that the high-temperature state, above 100 K, is Curie-Weiss paramagnetic. The Curie constant $C = 0.54(1)$ emu K mol^{-1}, corresponding to an effective moment $\mu_{\text{eff}} = 2.08\,\mu_{\text{B}}$: this is a rather large value for Cu^{2+}, which possibly caused by the presence of a small number of W^{5+} ions due

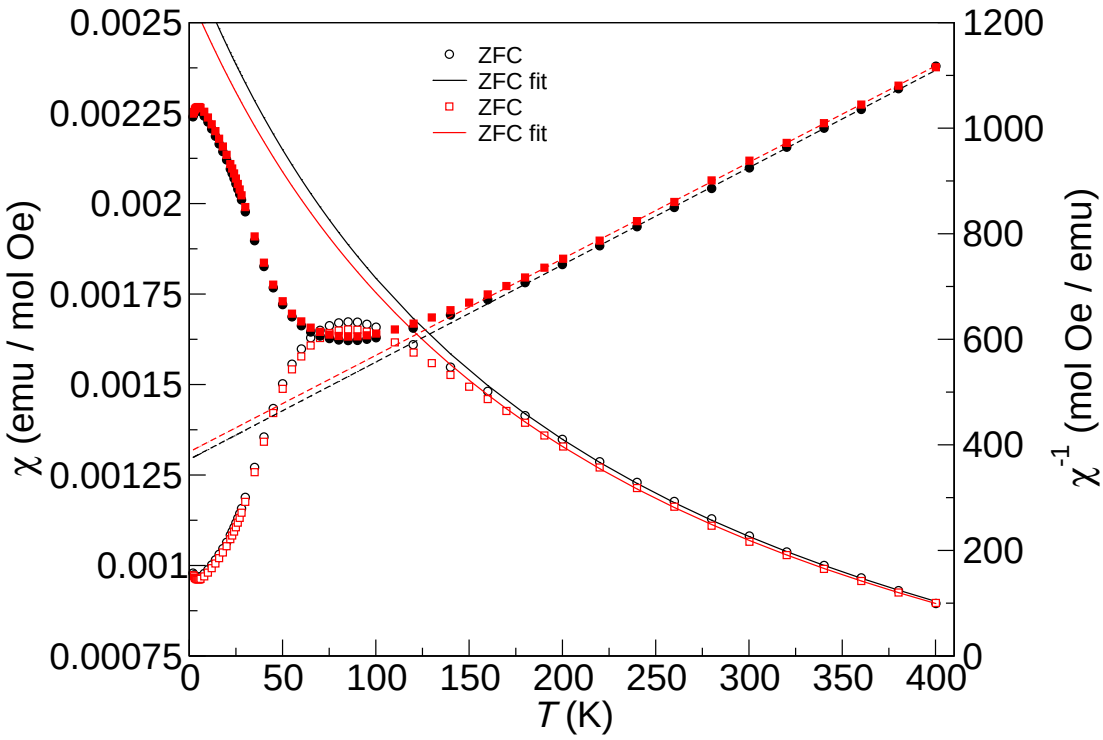

Figure 3.2 Magnetic susceptibility (left axis, open symbols) and inverse susceptibility (right axis, filled symbols) of Sr_2CuWO_6 in zero-field-cooled (circles) and field-cooled (square) measurements, with fits to Curie-Weiss paramagnetism above 170 K.

to hybridisation of electron orbitals between the two B sites in the material. The Weiss temperature θ_{CW} is -210 ± 10 K (Figure 3.2). This differs from the Weiss constants of -116 K and -118 K previously reported by Vasala *et al.* [53] and Iwanaga *et al.* [64], and is closer to the value of -230 K reported by Blasse [51]. As has been noted before [53], there is a broad maximum centred around 80 K and then again a slight upturn below 10 |kelvin that could be due to paramagnetic impurities, but no anomalies and no splitting between field-cooled and zero-field-cooled data. This has previously led to speculation that Sr_2CuWO_6 has a 2D spin-liquid magnetic ground state [53].

Our initial heat capacity data did not reveal any magnetic anomalies in the heat capacity (Figure 3.3). Following the muon spin relaxation spectroscopy experiment by Vasala *et al.* revealing a transition at 24 K, more detailed measurements were done around this temperature; with steps of 0.2 K between 20 K and 30 K. These data revealed a very small peak (Figure 3.3 inset) and the entropy release at the transition (on heating through it from 20 K to 26 K) is estimated at $0.3 \pm 0.2\%$ of the total magnetic entropy of $R \ln(2) = 5.76\,\mathrm{J\,K^{-1}\,mol^{-1}}$ form. unit (Figure 4.23).

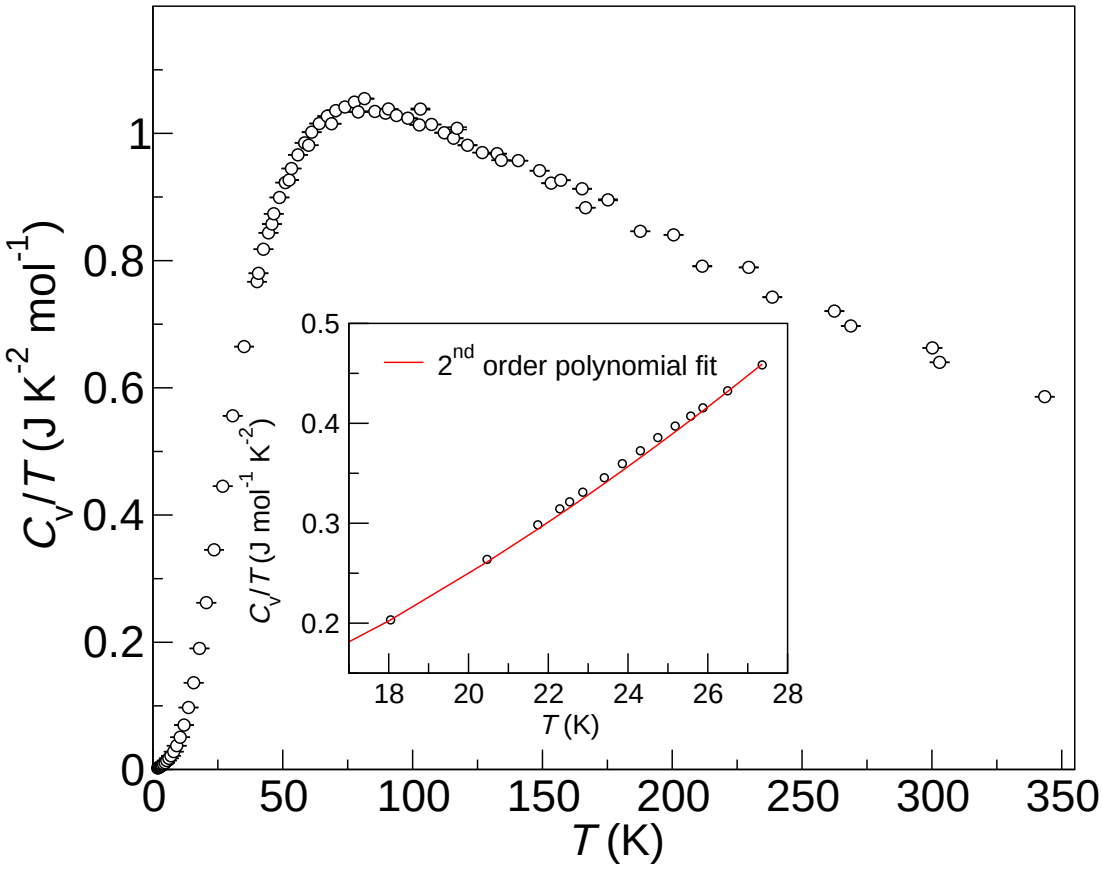

Figure 3.3 Heat capacity of Sr_2CuWO_6. Inset shows the region where a peak caused by the ordering seen in μSR is expected, compared to a background derived by fitting a 2nd-order polynomial to the data points surrounding the "peak".

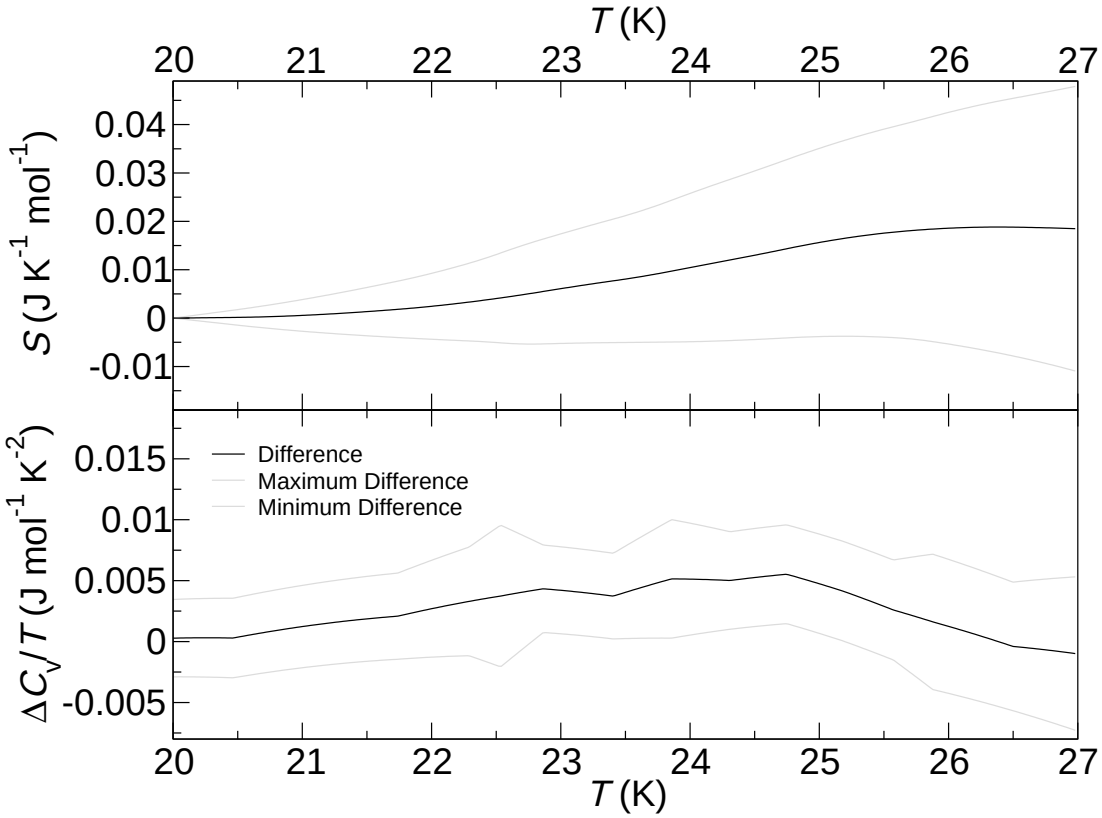

Figure 3.4 Estimate of the magnetic entropy release at the transition (top) as a function of temperature (top) based on the difference with the fitted background heat capacity (bottom).

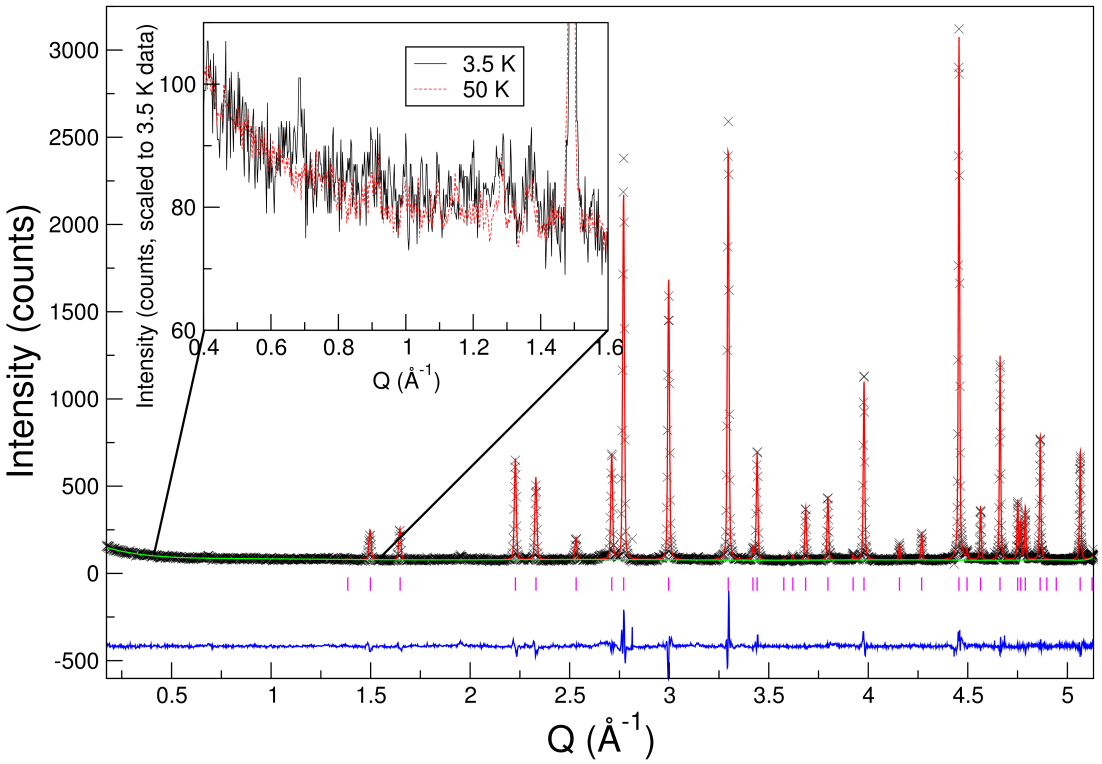

Figure 3.5 Neutron diffraction pattern of Sr_2CuWO_6 at 3.5 K, neutron wavelength 2.398 Å. Inset: Comparison of 3.5 K (solid line) and 50 K (dashed line) neutron diffraction patterns, showing the magnetic peak at $Q = 0.68\,\text{Å}^{-1}$.

3.3.2 Structural probes

Low-temperature neutron diffraction data of Sr_2CuWO_6 are shown in Figure 3.5. The compound refines to space group I4/m, as described in previous studies [53, 54]. Table 3.1 gives all details of the present refinement which is in good agreement with previous data. The data at 3.5 K show a very small additional peak at $Q = 0.68\,\text{Å}^{-1}$. Comparison with an extra measurement at 50 K, as shown in the inset of Figure 3.5, confirms that the reflection appearing at $0.68\,\text{Å}^{-1}$ is the only magnetic Bragg peak.

For comparison, the neutron diffraction pattern of Ba_2CuWO_6 in the magnetically-ordered state reveals two peaks [54], like in Sr_2CuWO_6 at $0.68\,\text{Å}^{-1}$, plus an additional reflection at $1.24\,\text{Å}^{-1}$. The magnetic reflections in Ba_2CuWO_6 were indexed as $\left(\frac{1}{2}, \frac{1}{2}, \frac{1}{2}\right)$ and $\left(\frac{1}{2}, \frac{1}{2}, \frac{3}{2}\right)$ on a face-centred unit cell, corresponding to $\left(\frac{1}{2}, 0, \frac{1}{2}\right)$ and $\left(\frac{1}{2}, 0, \frac{3}{2}\right)$ in the body-centred tetragonal setting, respectively.

The magnetic structure refinement points to type-2 antiferromagnetic order for

Table 3.1 Refinement results of Sr_2CuWO_6 at different temperatures. 3.5 K data were refined diffraction patterns from neutrons of wavelengths 1.594 Å and 2.398 Å simultaneously; 50 K data were refined from neutron diffraction data from neutrons of wavelength 2.398 Å; room temperature data were refined from neutron diffraction data from wavelength 1.594 Å.

T (K)	3.5	50	300
a (Å)	5.409 65(4)	5.410 65(3)	5.429 02(3)
c (Å)	8.413 68(7)	8.413 97(6)	8.416 14(8)
V (Å^3)	246.221(5)	246.320(4)	248.059(4)
Sr (0, 0.5, 0.25)			
B (Å^2)	0.11(4)	0.30(4)	0.44(2)
Cu			
B (Å^2)	0.33(7)	0.64(7)	0.13(4)
W			
B (Å^2)	0.42(9)	0.45(10)	0.07(6)
O1 (x, y, 0)			
x	0.2892(4)	0.2893(4)	0.2869(3)
y	0.2024(4)	0.2013(4)	0.2073(3)
B (Å^2)	0.21(3)	0.32(3)	0.38(2)
O2 (0, 0, z)			
z	0.2277(2)	0.2272(2)	0.2269(2)
B (Å^2)	0.02(5)	0.15(6)	0.73(3)
R_p (%)	7.09	4.24	4.97
R_{wp} (%)	8.96	5.75	6.80
R_{exp} (%)	5.53	1.64	2.50
χ^2	4.785	12.39	7.498

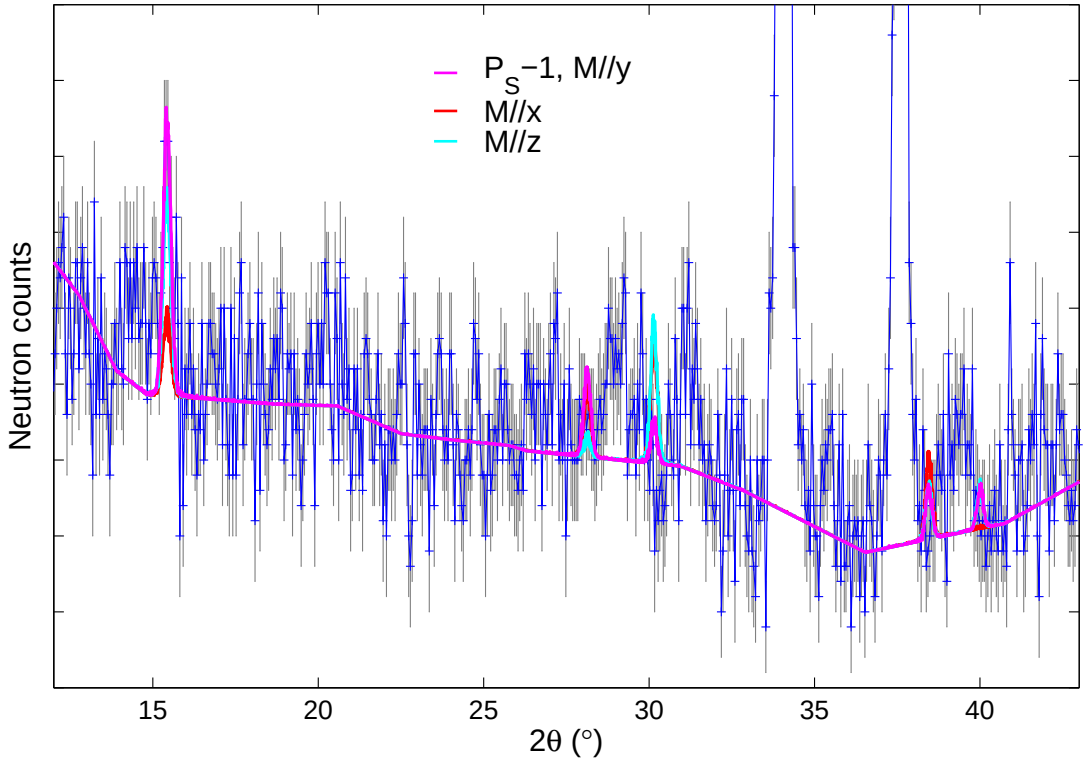

Figure 3.6 Low-temperature magnetic peak in Sr_2CuWO_6, with fit to $P_s\bar{1}$ magnetic space group.

which the reflection at $0.68\,\text{Å}^{-1}$ is again indexed with a $\left(\frac{1}{2}, 0, \frac{1}{2}\right)$ k-vector. The best fit was with moments [55] aligned along the b-axis, leading to orthorhombic magnetic space group $P_s\bar{1}$ (Figure 3.13). While Vasala *et al.* did not observe any magnetic Bragg peaks in their low-temperature neutron diffraction data, they did correctly predict the magnetic structure to be of type 2 with the aid of *ab initio* calculations combined with X-ray absorption-spectroscopy data [55].

3.3.3 Muon spin relaxation

The previous μSR study revealed a sharp magnetic transition and yielded the ordered moment as a function of temperature below $T_N = 24\,|\text{kelvin}$ [55]. This transition is also observed in our data (Figure 3.7) with a sharp drop in the $t = 0$ polarization between 25 K and 20 K. The present data, collected at the ISIS facility (which is a high-intensity pulsed source) is complementary to the data by Vasala *et al.* taken at PSI; the time resolution at MuSR at ISIS is lower, but the muon relaxation can be followed over much longer time scales (up to 16 µs) due to the much higher number of muons implanted with each pulse/time frame.

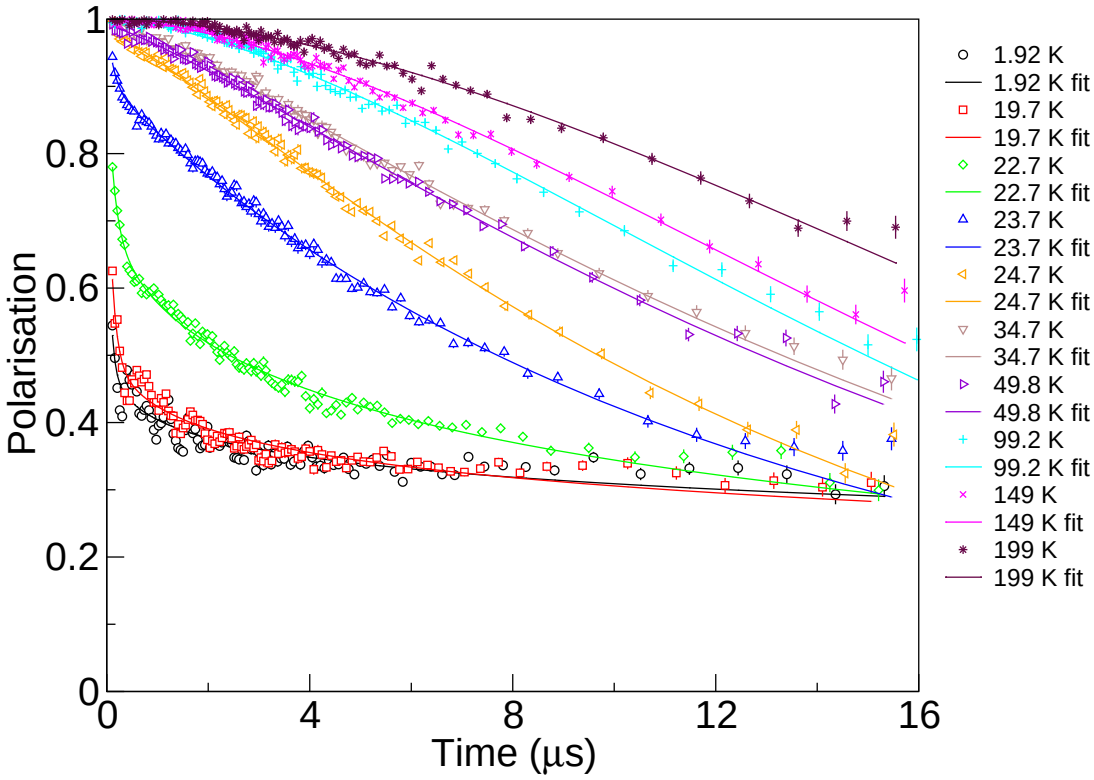

Figure 3.7 MuSR on Sr_2CuWO_6 in zero field. Fits are to a linear combination of stretched exponential and fast Lorentzian decay (Equation 3.1).

Between 20 K and 200 K the muon relaxation can be fitted with a linear combination of Lorentzian and stretched exponential decays;

$$P_z = K_1 \left(e^{-\lambda t}\right) + K_2 \left(e^{-(\sigma t)^{\beta}}\right), \tag{3.1}$$

with the additional constraint that $K_1 + K_2 = 1$. λ and σ are the Lorentzian and compressed exponential relaxation factors respectively, and β is the stretching exponent – in the present case, with $\beta > 1$ the relaxation is *compressed* exponential, approaching $\beta \approx 1.8$ at high temperatures ($\beta = 2$ would equate Gaussian relaxation). The results of the fits at temperatures between 2 K and 199 K are shown in Figure 3.8. Down to 24.7 K, right above the ordering transition, the Lorentzian component remains close to zero and the relaxation is well modelled by the compressed exponential. As the system is cooled from 200 K there is a steady increase in σ and a gradual reduction in β, providing evidence of a gradual slow-down of the spin dynamics that starts at temperatures far above T_N.

Below $T_N = 24$ K a significant contribution from fast Lorentzian relaxation can be

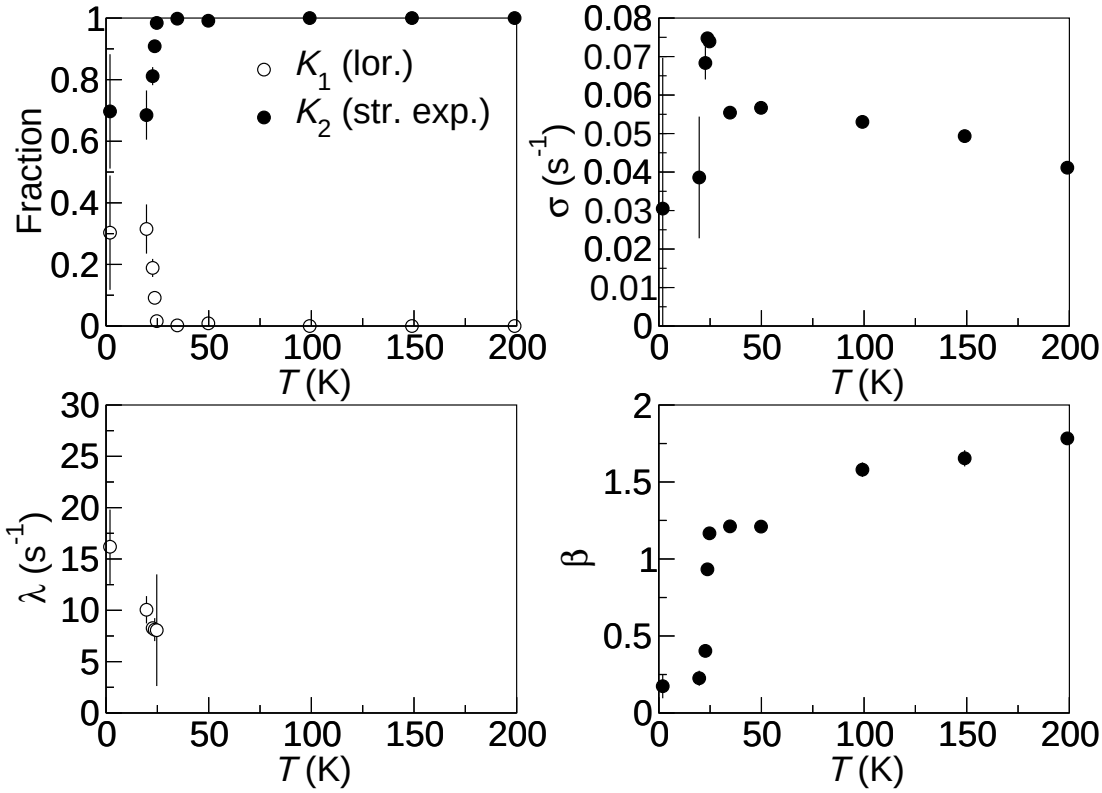

Figure 3.8 Parameters to fits of muSR data for Sr_2CuWO_6 (see Figure 3.7).

seen, and the stretching exponent β drops sharply to values below 1. Considering both the muon relaxation curves of Figure 3.7 and the fit data of Figure 3.8 it is clear that while the two components in Equation 3.1 accurately model two types of muon relaxation present in the sample above T_N, this is no longer the case below 20 K. In the 3D-ordered state strongly damped oscillations are observed, but in this case not with sufficient resolution to determine the ordered moment as a function of temperature, as was done by Vasala *et al.* [55]. The strong damping of the oscillations points to a wide distribution of local fields around the non-zero mean value. This is indicative of a fair amount of magnetic disorder, which is due to the presence of many small magnetic domains, as we will see later. The relaxation to $1/3^{\text{rd}}$ of the initial polarisation shows that one-third of the moments are aligned parallel or antiparallel with the initial muon polarisation, as expected for static moments in a powder sample with no preferential crystallographic and therefore magnetic orientation.

3.3.4 Inelastic neutron scattering

Inelastic neutron scattering measurements were carried out to characterise the dynamic magnetic correlations as a function of temperature. 30 meV neutrons were used ($\lambda = 1.65\,\text{Å}$) and the neutron spectrum taken at 5 K is shown in Figure 3.9. The two bands below $1.5\,\text{Å}^{-1}$, rising up to approximately 14 meV, are of magnetic origin – no structural reflections occur at these wave numbers. We focus in particular on the part of the magnetic dispersion rising up from approximately $Q = 0.68\,\text{Å}^{-1}$, where the $\left(\frac{1}{2}, 0, \frac{1}{2}\right)$ reflection is located at the elastic line. In Figure 3.10 the inelastic scattering in this area is shown as a function of temperature.

The energy window for neutrons at these short wave numbers is rather narrow regardless of the energy of the incident neutrons, but with 30 meV neutrons a significant section of the magnetic spin-wave dispersion and dynamic magnetic correlations can still be observed. The zero-energy-transfer origin of the dispersion, and center of mass, appears to be at about $0.62\,\text{Å}^{-1}$, somewhat below the elastic magnetic reflection at $0.68\,\text{Å}^{-1}$. Figure 3.11 shows the neutron scattering intensity integrated over energies from 4 to 6 meV and corrected for the magnetic form factor, showing the same mismatch. The reason for the mismatch is that the dispersion observed here does *not* correspond to the 3D spin-waves in the *ordered* phase. The energy scale of the 3D ordering is up to ~ 2 meV and the signal up to that energy is swamped by the elastic line and hence is invisible here. The dispersion observed here corresponds to 2D dynamic antiferromagnetic correlations – the energy scale of 14 meV (≈ 162 K) is of the order of the in-plane magnetic exchange interactions. It is then not surprising that the dispersion curves remain practically unchanged on heating above the ordering transition, with strong correlations visible even at 50 K and still just about visible at 100 |kelvin.

The energy-integrated scattering shown in Figure 3.11 exhibits a peak shape that is characteristic of 2D correlations in a powder sample, as described by Warren [65, 66];

$$I = \frac{C\left(1 - 2\left(\frac{\lambda q}{4\pi}\right)^2 + 2\left(\frac{\lambda q}{4\pi}\right)^4\right)\sqrt{\frac{\xi}{\lambda\sqrt{\pi}}} \times \int_0^{20} F(a)\,\mathrm{d}x}{\left(\frac{\lambda q}{4\pi}\right)^{\frac{3}{2}}} + K \tag{3.2}$$

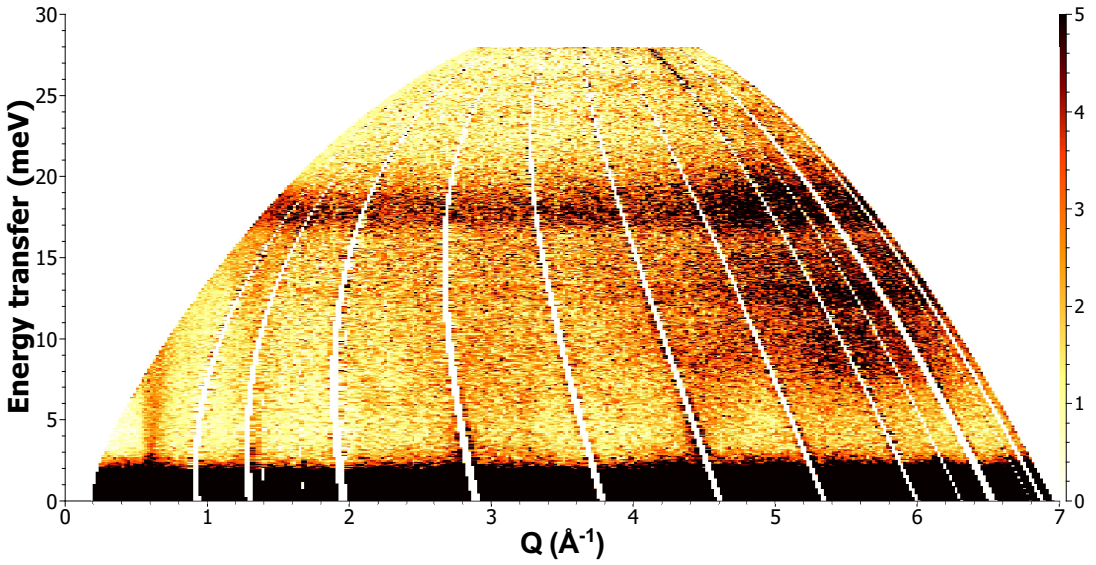

Figure 3.9 Full inelastic neutron scattering spectrum of Sr_2CuWO_6 at 5 K.

where

$$F(a) = e^{-\left(x^2-a\right)^2} \tag{3.3}$$

and

$$a = \frac{\xi\sqrt{\pi}\,(q-q_0)}{2\pi} \tag{3.4}$$

and $\lambda = 1.65\,\text{Å}$ is the neutron wavelength. The wave vector obtained from the fit $q_0 = 0.592(2)\,\text{Å}^{-1}$ corresponds to the in-plane $\left(\frac{1}{2}, 0, 0\right)$ antiferromagnetic wave vector. This is a strong indication that above T_N the correlations are 2D, in the $a-b$ planes, and persist, if weakly, up to 100 K. The fits yield a lower limit to the correlation length ξ as a function of temperature, shown in Figure 3.12.

3.4 Discussion

The presence of 2D dynamic antiferromagnetic correlations above T_N and up to $\sim 100\,\text{K}$, as observed in the neutron spectra of Figures 3.10 and 3.11, explains the absence of an anomaly at T_N in the magnetic susceptibility. We can conclude that below the broad maximum in the magnetic susceptibility data (Figure 3.2)

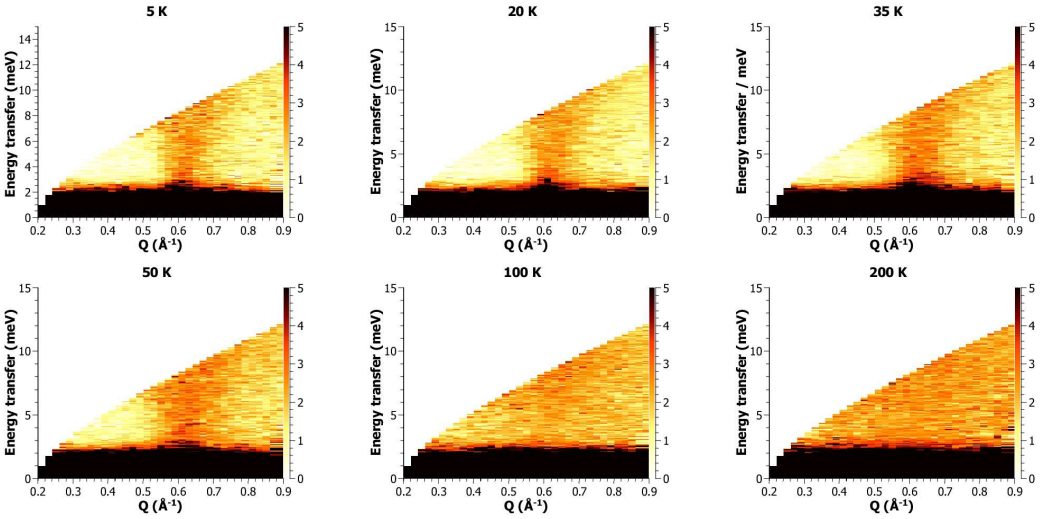

Figure 3.10 Inelastic neutron scattering spectrum of Sr_2CuWO_6 at a range of temperatures, showing strong scattering at $Q = 0.63\,\text{Å}^{-1}$ below 100 K.

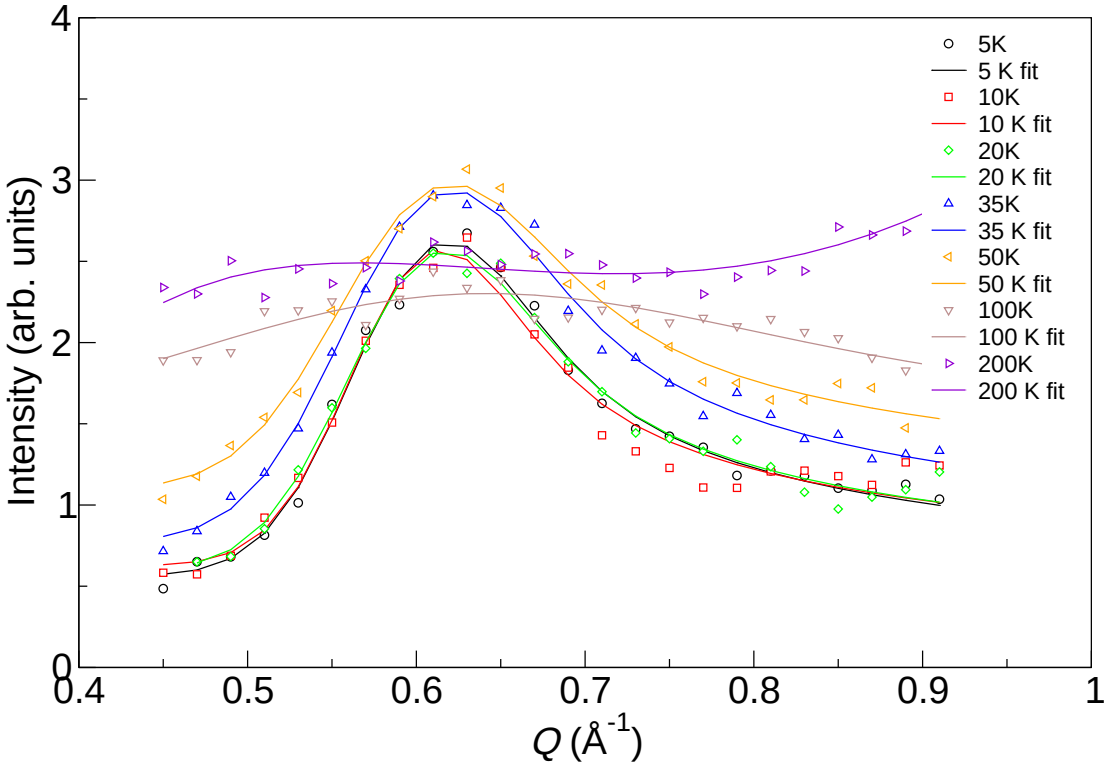

Figure 3.11 Warren function (Equation 3.2) fit to inelastic peak below 100 K, integrated between 4 meV and 6 meV.

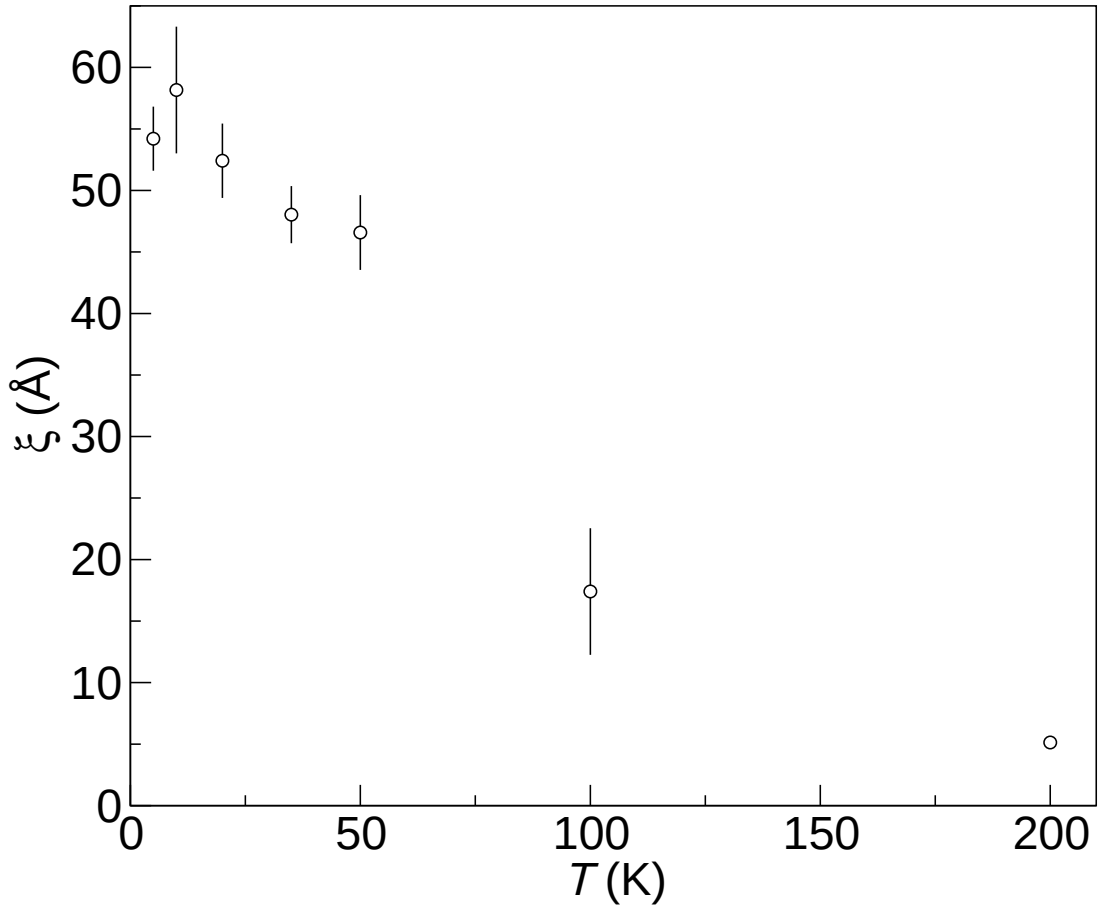

Figure 3.12 Change in correlation length in Warren function with temperature.

at 100 K antiferromagnetic spin correlations start to grow as the temperature is lowered, while not far above 100 K Curie-Weiss paramagnetism sets in. The μSR data show that there is a gradual slowing down of spin fluctuations with increasing 2D spatial correlations, but that the spins remain dynamic until cooled below T_N.

These observations are also consistent with the very small peak that can just be discerned in the heat capacity data between 20 K and 26 K, peaking at $\sim$ 24 |kelvin. The (2D) magnetic wave vector in the 2D layers is $\left(\frac{1}{2}, 0\right)$ and this leads to three distinct ways an ordered 2D layer can be stacked on the preceding one along the c-axis: shifted by 1/2 a phase along the magnetic k-vector, and rotated by 90° around the c-axis. The entropy associated with the 2D- to 3D-ordering transition can then be calculated as follows: the total number of distinct configurations of l 2D ordered layers $\Omega(l) = 3^{l-1}$, and hence the entropy of the 2D- to 3D-ordering transition as a function of l is given by

$$S_{\text{2D-3D}}(l) = \ln[\Omega(l)] = \ln(3^{l-1}) = (l-1)\ln(3) \quad \propto n^{\frac{1}{3}} \ln(3), \tag{3.5}$$

where n is the total number of magnetic $S = 1/2$ spins in a sample grain or in the coherent volume. Note that we see from the approximate equation at the right-most side that this entropy is subextensive.

If we assume that the coherent volume below the transition contains an equal number of spins along each crystallographic axis then the total magnetic entropy of that volume can be written as

$$S_{\text{magnetic}}(l) = l^3 \ln(2) \tag{3.6}$$

and the ratio

$$S_{\text{2D-3D}}(l)/S_{\text{magnetic}}(l) = \frac{l-1}{l^3}\frac{\ln(3)}{\ln(2)} \tag{3.7}$$

The experimentally-obtained ratio of 0.003 (0.3%) yields $l = 15$, which translates to a correlation length of 63 Å along the c-axis and 81 Å in the $a-b$ plane. This is consistent with the broad magnetic $\left(\frac{1}{2}, 0, \frac{1}{2}\right)$ reflection shown in Figure 3.6. It is also reassuringly close to the lower limit of the correlation length in the $a-b$ plane just above the transition (55 Å), as obtained from the Warren fits. This then implies that below T_N small 3D magnetic domains are present, with the in-plane component of the magnetic k vector variably aligned along the crystallographically equivalent a- and b-axes. As mentioned earlier, the presence of these small AF domains also explains the strong damping of the

muon oscillations below T_N.

The available data are fully consistent and readily explained by the presence of strong 2D correlations persisting above T_N, in what could be described as a "thermal spin liquid". While this is in line with earlier proposals [55] it is not clear how this phase arises if the computational exchange constants [55] are correct – in particular if J_4 is indeed as strong as -4.21 meV (49 K), 56% of the dominant J_2 exchange. This would not be a quasi-2D system and could be expected to show 3D Néel ordering around at least 50 K. Note that the two interpenetrating 3D sublattices arising from the J_2 and J_4 bonds only (Figure 3.13) are not by themselves frustrated. When they order fully antiferromagnetically, each with a wave vector $\left(\frac{1}{2}, \frac{1}{2}, \frac{1}{2}\right)$, there is a two-fold degeneracy arising from the relative phase of the two sublattices. Both degenerate states are type-2 antiferromagnetic, with the in-plane antiferromagnetic phase vector aligned along the a or the b axis. This degeneracy is not lifted by inclusion of the much weaker J_1 and J_3 because for each J_1 edge with antiferromagnetically aligned spins at the vertices there is a J_1 edge with ferromagnetically aligned spins.

Hence, the observed type-2 antiferromagnetism is consistent with the predicted exchange constants, but the dynamic correlations in the "2D thermal spin liquid" state above T_N are not. In the archetypical quasi-2D antiferromagnet La_2CuO_4 the ratio between the interplane exchange constant and the main in-plane exchange interaction $J_\perp/J_1 = 10^{-5}$. This is hugely different from the ratio between the predicted J_4 and J_2 for Sr_2CuWO_6, considering that the ratio of the Néel temperature T_N over J_1 in La_2CuO_4; 300 K / 1345 K = 0.22, is only slightly less than T_N over J_2 in Sr_2CuWO_6. Furthermore, the short-ranged correlations evident above T_N in Sr_2CuWO_6 are 2D and strongly reminiscent of the magnetism in La_2CuO_4 above 300 K. Hence, it is very unlikely that the theoretically-predicted value for $J_4 = -4.21$ meV is correct.

One possible explanation for the computational overestimate lies in the role of the W $5d^1$ orbital. The W cations are part of the J_2 and J_4 interaction pathways and XAS by Vasala *et al.* [55] indicates that there is some overlap between the Cu $3d$ – O $2p$ bands and the W $5d$ – O $2p$ bands. It may then be of relevance that the magnetism of W $5d^1$ electrons in an octahedral crystal field is described by a Kugel-Khomski Hamiltonian in the limit of strong spin-orbit coupling, as described in detail by Gang-Chen *et al.* [50]. This gives rise to a magnetic Hamiltonian in which the exchange pathway itself depends on the orientation of the magnetic (spin-orbital) moments. Combined with the solid orbital ordering

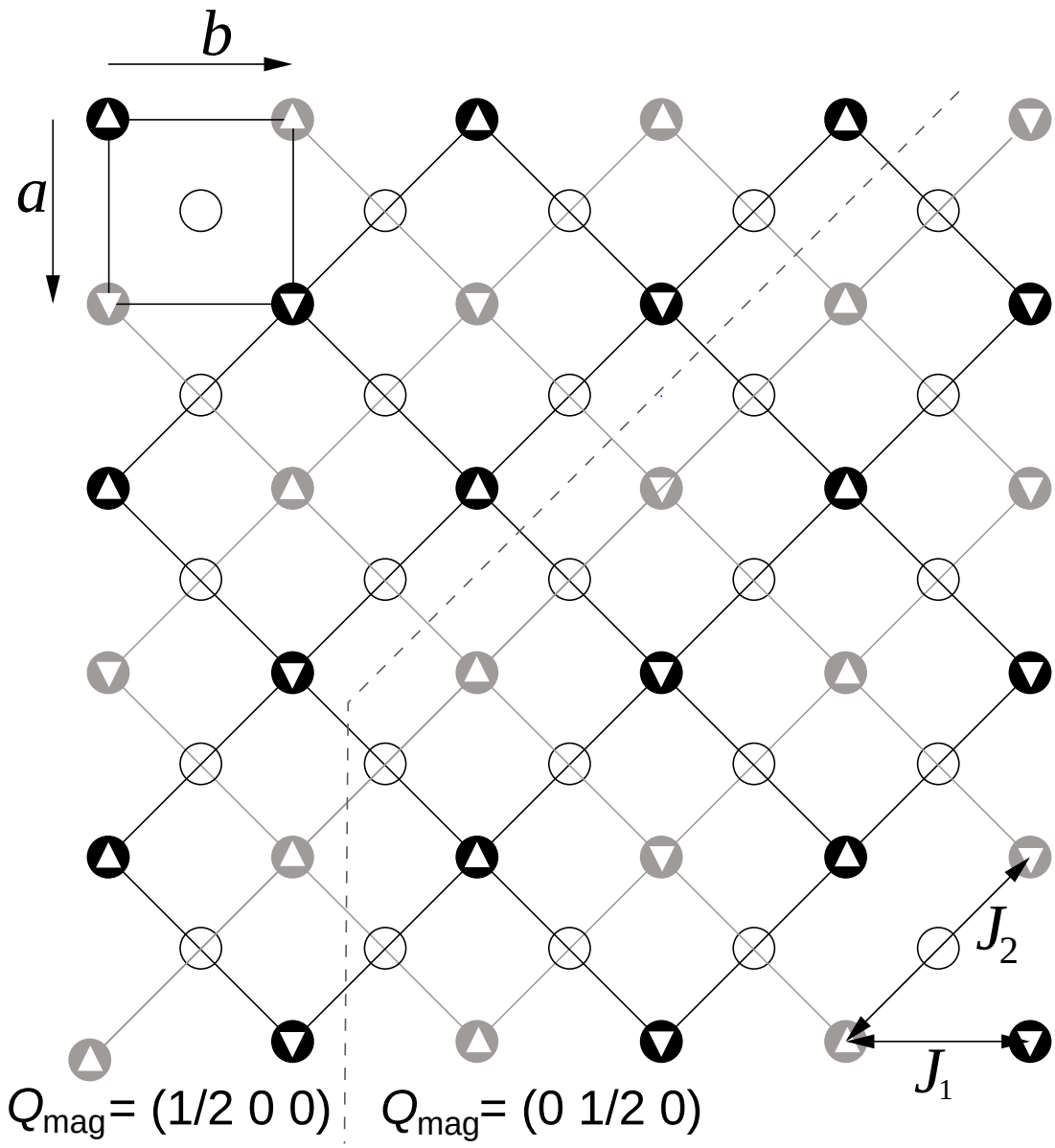

Figure 3.13 A single layer with W(VI) (open circles) and Cu(II) (circles with up/down triangle, i.e. spin inside) showing the spin configuration in a [001] (a-b) plane. The same structure is also repeated in the [110] plane, which fully defines the type-2 antiferromagnetic structure. The dark and light lines represent the strong Cu-O-W-O-Cu J_2 exchange interactions, forming the two independent Cu(II) sublattices with dark and light circles. The dark sublattice is perfectly AF ordered. On the light (crystallographically equivalent) sublattice there is a phase shift causing a domain wall (broken line). At the domain wall on the light sublattice, the composite 2D magnetic wave vector rotates by 90°, pointing along the a-axis (right) and pointing along the b-axis (left). A possible change in spin orientation across the domain wall is not taken into consideration.

of the magnetic Cu^{2+} $d_{x^2-y^2}$ orbital in the $a-b$ plane, perhaps the strongly spin-orbit-coupled magnetism of the W cation causes a much greater difference between J_2 and J_4 interactions. This is something that might be worth exploring in further detail. Further neutron spectroscopy experiments, from which the exchange constants could be determined via spin-wave modelling, would also be beneficial but probably only if done using large single crystals which are presently not available.

With regards to the muon relaxation in the thermal spin liquid regime, it is worth noting that compressed exponential relaxation has been observed in other spin liquid phases, for example in $SrCr_8Ga_4O_{19}$ (SCGO) [67], herbertsmithite ($ZnCu_3(OH)_6Cl_2$) [68] and the double perovskite Ba_2YMoO_6 [19]. In SCGO the compressed exponential approaches Gaussian as the temperature is lowered and it is thought to arise from a dynamical and heterogeneous ground state with a mixture of unpaired spins and spins paired into spin-singlet dimers, so that any particular muon environment fluctuates between magnetic and non-magnetic at a time scale shorter than the muon lifetime. This inevitably gives rise to a lifetime faster than that observed for the other examples and in Sr_2CuWO_6 there is no evidence of spin-singlet dimers, as they would be manifest in neutron spectroscopy data as near-neighbour antiferromagnetic correlations only. This also rules out any fundamental similarity with the spin liquid states in herbertsmithite and Ba_2YMoO_6 as both states are thought to be dominated by near-neighbour spin-singlet [14] and spin-orbital singlet dimers [19], respectively. In Ba_2YMoO_6 the compressed exponential muon relaxation is the result of two distinct muon environments: those adjacent to unpaired (dangling) fluctuating spins and those sitting elsewhere in the material, surrounded by non-magnetic spin-orbital singlet pairs. Hence there is a rather large variety of scenarios that give rise to compressed exponential relaxation and they have to be considered case by case. No further parallels can be drawn between the case of Sr_2CuWO_6 and the others.

3.5 Conclusions

Below 24 K the quasi-2D square lattice antiferromagnet Sr_2CuWO_6 freezes into a 3D-ordered Néel state with k-vector $\left(\frac{1}{2}, 0, \frac{1}{2}\right)$, pointing to type-2 antiferromagnetic order (magnetic space group $P_s\bar{1}$) as predicted previously based on X-ray absorption spectroscopy combined with computational studies [55]. Further results by Vasala *et al.* suggest that Sr_2CuWO_6 displays type-2 antiferromagnetic

long-range order at 3 K, as confirmed here [69]. They find the propagation vector $k = \left(0, \frac{1}{2}, \frac{1}{2}\right)$, identical by symmetry to the $k = \left(\frac{1}{2}, 0, \frac{1}{2}\right)$ result described here. As often for quasi-2D antiferromagnets with $S = 1/2$, neutron spectroscopy shows that dynamic 2D correlations are detectable far above T_N; in this case up to ~ 100 K, a temperature that is comparable to the energy scale of the main exchange interaction estimated at -86 K and coinciding with the maximum in the magnetic susceptibility. Furthermore, μSR shows a pronounced slowing down taking place well before T_N is reached on cooling.

The pronounced 2D character of the magnetism is however surprising in the light of the exchange constants one might expect considering the structure of Sr_2CuWO_6. Perhaps the spin-orbit coupling in the $5d^1$ band of the W cations on the dominant exchange interaction pathway, not taken into account in the reported calculations [55], can explain the large difference between in-plane and out-of-plane exchange interactions implied by the above observations.

Chapter 4

The Series of Double Perovskites $Ba_2Y_xWO_6$ ($\frac{2}{3} \leq x \lesssim 0.80$)

4.1 Introduction

The Mo^{5+} ($4d^1$, $S = \frac{1}{2}$, $J = \frac{3}{2}$) double perovskite Ba_2YMoO_6 has been studied in great detail by dc and ac susceptibility, structural probes, transport property measurements, and muon spin resonance [18–20, 70], in order to determine the effect of spin-orbital coupling in molybdenum on the geometric frustration observed in the compound. It has been suggested that the electron spins in Ba_2YMoO_6 freeze into a valence-bond-glass configuration at low temperature ($T_N = 1.3\,\mathrm{K}$), with adjacent electron spins pairing up randomly [18, 20]. This results in "dangling" spins distributed randomly throughout the material, which have no unpaired neighbours: these paramagnetic spins account for around 8 % of molybdenum moments.

The tungsten analogue Ba_2YWO_6 is also cubic and was first reported in 1972 [71]. In the stoichiometric form this material has (or is expected to have) $5d^1$, $S = \frac{1}{2}$, and $J = \frac{3}{2}$ due to exceptionally strong spin-orbit coupling present in the $5d$ series. Despite the presence of an unpaired electron on the tungsten, Ba_2YWO_6 is a Mott insulator, with strong localisation of electrons.

Like Ba_2YMoO_6, Ba_2YWO_6 has a network of edge-sharing tetrahedra between each of the B and B' sites. The magnetic B' site is thus expected to show antiferromagnetic behaviour, by superexchange along a B'-O-O-B' pathway [5, 7].

Within this Chapter, the many approaches used in attempting to synthesise the stoichiometric material, $Ba_2Y_1WO_6$, are detailed, along with magnetic and structural studies on the series of compounds with variable yttrium content ($Ba_2Y_xWO_6$, $\frac{2}{3} \leq x \lesssim 0.80$), which have average tungsten oxidation states between 6+ and 5.45+. In addition, the synthesis of the related material Ba_2NdWO_6, and lithiation of the band insulating material $Ba_2Y_{\frac{2}{3}}WO_6$ are discussed.

4.1.1 B-site deficiencies in double perovskites

Hexagonal perovskites of the form $A_nB_{n-1}C_{3n}$ have been studied for many years [72], and have been recognised as potential dielectric resonators [73]. The $x = \frac{2}{3}$ member of the $Ba_2Y_xWO_6$ series of compounds detailed in this Chapter is an $n = 6$ member of the hexagonal perovskite family.

Hexagonal perovskites can be categorised according to the type of stacking observed in between AO_3 layers [72]. The stacking can be either cubic-type (c), with offset, vertex-sharing octahedra, or hexagonal-type (h), [72], in which $BO_{6/2}$ octahedra stack directly above one another, sharing faces. A double perovskite can thus be described in terms of this stacking, rather than in terms of the $BO_{6/2}$ octahedra often used in cubic perovskites. This classification allows subdivision into two general classes of double perovskite: "shifted" and "twinned" structures [74].

"Shifted" perovskite structures have a general arrangement of layers $(hhc_{n-2})_3$, with a layer of ordered B-site vacancies between the h layers. This leads to a shift in the cubic stacking of the corner-sharing octahedra of one-third of a unit cell in the $(01\bar{1}0)$ direction. The number of cubic-stacked layers is related to n in the general $A_nB_{n-1}C_{3n}$ formula: there are $n-1$ layers of corner-sharing octahedra, and thus $n-2$ (c) layers [74].

"Twinned" perovskites have partially occupied $BO_{6/2}$ layers, leading to a general arrangement $(hc_x)_m$ and interwoven hexagonal- and cubic-type stacking [74].

The type of stacking which is seen can be dependent on elemental composition or stoichiometry: for $n \leq 6$, shifted-type compounds are always seen [72]; for $n \geq 7$, twinned structured are possible, but require in most cases a tolerance factor $t \geq 1.05$. The Goldschmidt tolerance factor is calculated by the ratio of

ionic radii [32]:

$$t = \frac{r_A + r_O}{\sqrt{2}(r_B + r_O)} \tag{4.1}$$

where r_A and r_O are the radii of the A-site ion and oxygen ion respectively, and r_B is the average of the radii of the B-site ions (weighted to occupancy where appropriate).

For instance, $Ba_6TiNb_4O_{18}$, with $n = 6$ and $t = 1.0469$, has a shifted-type structure $(hhcccc)_3$ [75], whilst $Ba_8Ti_3Nb_4O_{24}$, with $n = 8$ and $t = 1.0511$ has a twinned-type structure $(hccc)_2$ [76] (Figure 4.1). This rule does not always hold true: the $n = 8$ compound $Ba_8Ta_6NiO_{24}$, has twinned $(cchc)_2$ stacking, but a tolerance factor of only 1.04 [77]. It is likely that this structure arises due to the particular arrangement of B-site cations with respect to one another: no $Ta^{5+}-Ta^{5+}$ pairs are found in the compound, due to the high positive charge density on the tantalum [74].

4.2 Experimental methods

4.2.1 Syntheses

$Ba_2Y_{0.75}WO_6$

Ba_2YWO_6 was synthesised from $BaCO_3$, Y_2O_3 and WO_3 in a standard solid state reaction, as previously used in the synthesis of Ba_2YMoO_6 [18]. Stoichiometric quantities of the reagents were ground together in an agate pestle and mortar, pressed into a pellet, then calcined at 900 °C for two hours, producing the intermediate $BaWO_4$. The pellet was then crushed and re-ground, then sintered in a 5 % H_2/N_2 gas mixture at 1200 °C for 12 hours. This step was repeated with intermediate grindings until X-ray diffraction showed no further improvement in sample quality. All syntheses were carried out on a 0.5 g scale, unless otherwise mentioned.

Initial X-ray diffraction measurements indicated that the target compound, Ba_2YWO_6, had been obtained (Figure 4.2), and magnetic and transport measurements were carried out accordingly. Subsequent neutron diffraction results

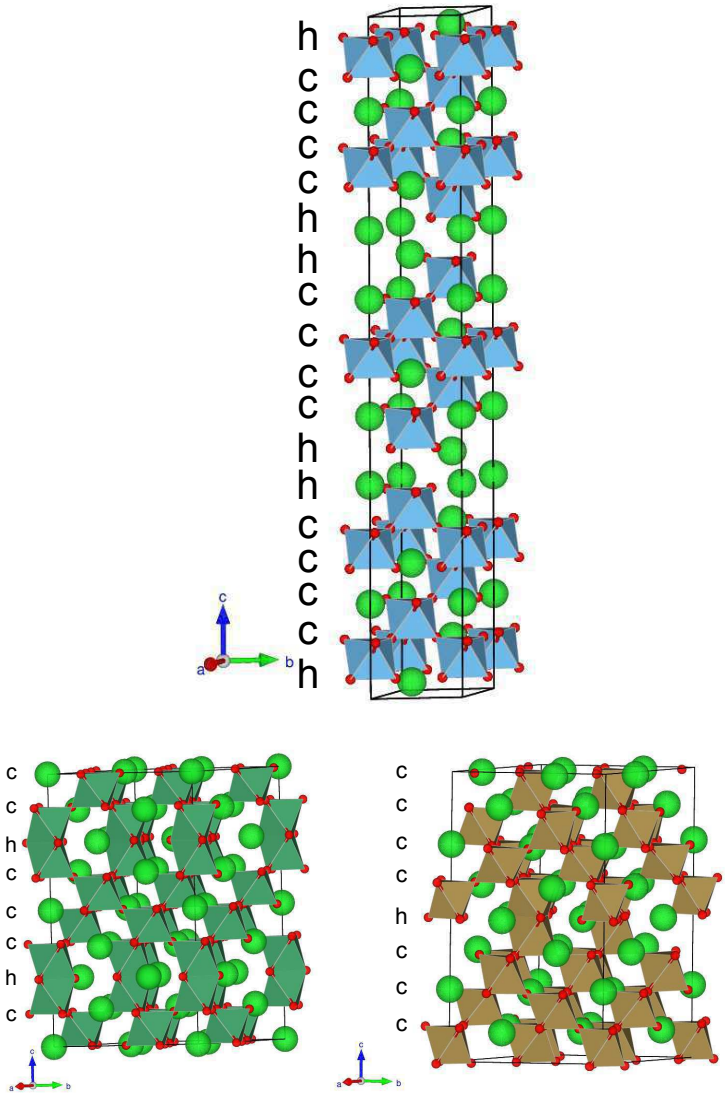

Figure 4.1 Comparison of hexagonal perovskites. Top: $Ba_6TiNb_4O_{18}$ [75]; bottom left: $Ba_8Ti_3Nb_4O_{24}$ [76]; bottom right: $Ba_8Ta_6NiO_{24}$ [77]. Octahedra represent mixed-occupancy B sites.

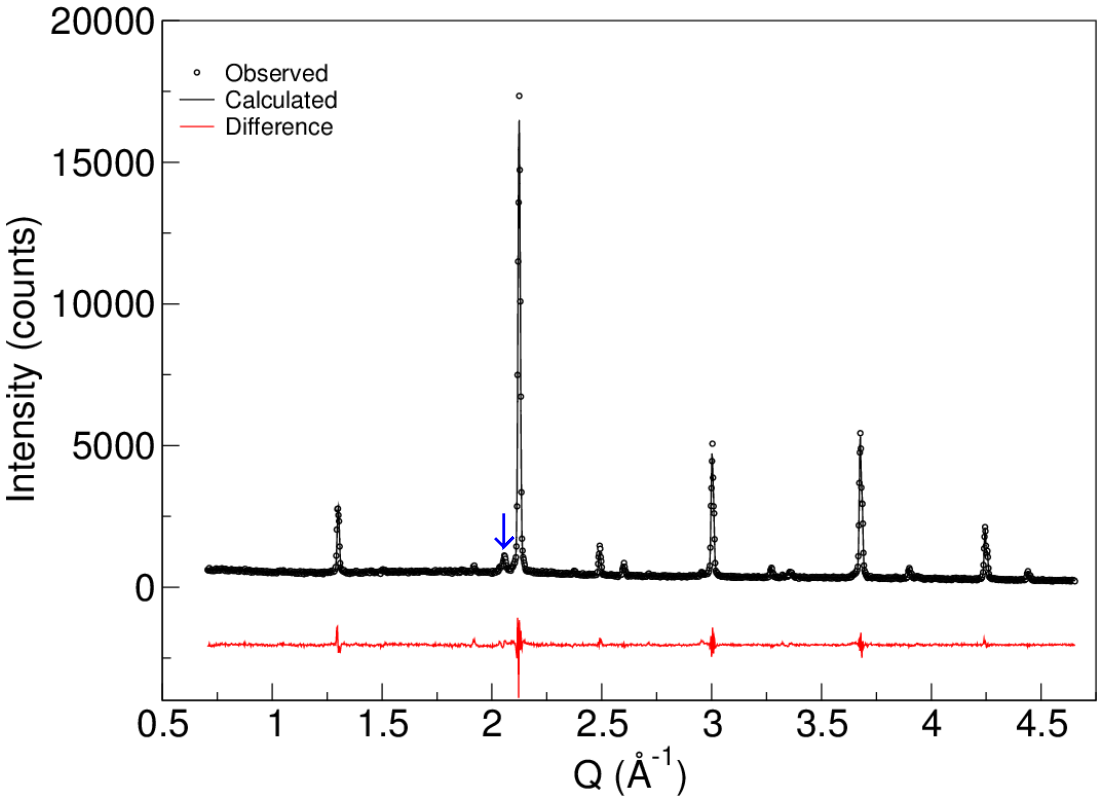

Figure 4.2 Fit of X-ray diffraction data of $Ba_2Y_{0.75}WO_6$, using $Ba_2Y_1WO_6$ as the model, $\chi^2 = 3.036$. A small Y_2O_3 impurity can be seen (blue arrow).

showed that the stoichiometry of the compound was in fact $Ba_2Y_{0.75}WO_6$: this was not seen in X-ray diffraction measurements due to the difficulty of refining yttrium occupancy in this compound – no improvement in quality of fit indicators was seen when the occupancy of any atom was allowed to vary.

Synthesis of the band insulator $Ba_2Y_{\frac{2}{3}}WO_6$

It was known from neutron diffraction measurements on $Ba_2Y_{0.75}WO_6$ that B-site vacancies are possible in $Ba_2Y_xWO_6$. Such vacancies have been reported previously, both in $Ba_2Lu_{\frac{2}{3}}WO_6$ [78] and $Ba_2Y_{\frac{2}{3}}WO_6$ [79].

Stoichiometric quantities of $BaCO_3$, Y_2O_3 and WO_3 were ground together, calcined in air at 900°C for two hours, then re-ground and sintered in air at 1200°C. An initial short sinter (up to four hours) resulted in formation of a cubic phase, with disordered yttrium vacancies, whilst longer or repeated sinters led to ordering of the vacant sites and formation of a layered unit cell, with space group $R\bar{3}m$ (Figure 4.3).

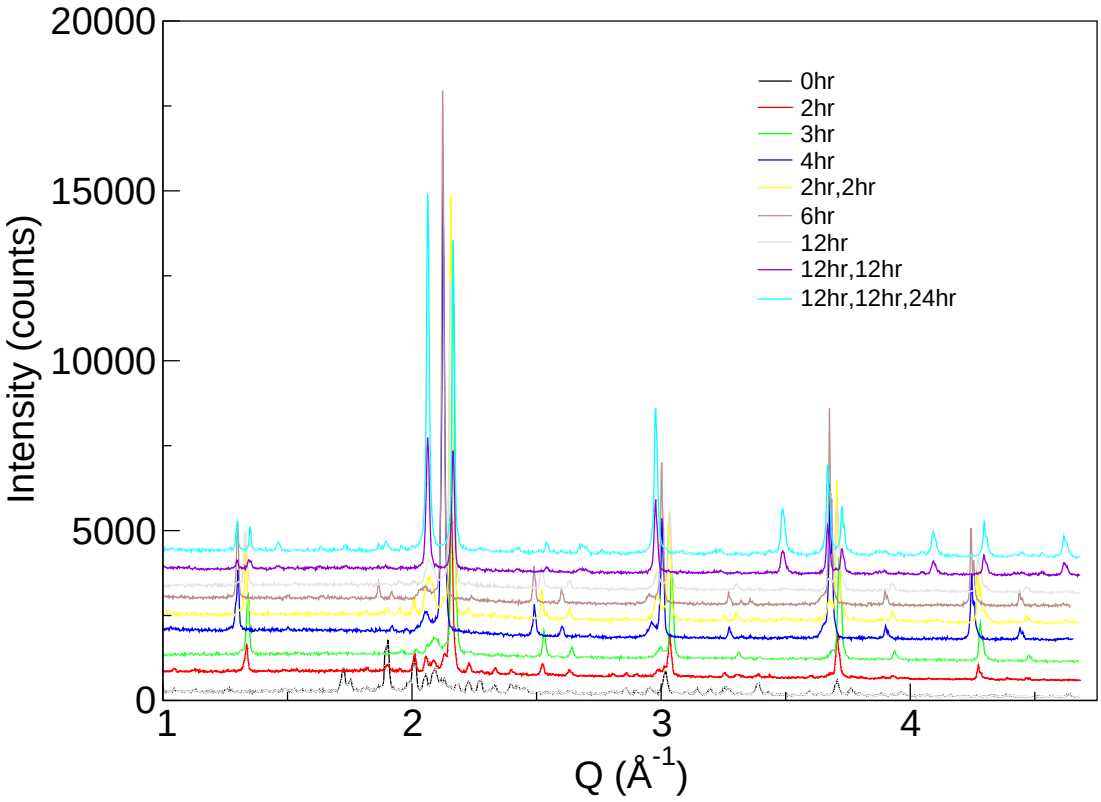

Figure 4.3 Evolution of $Ba_2Y\frac{2}{3}WO_6$ from cubic to rhombohedral phase as a function of sintering time. Where multiple times are listed, these represent multiple sintering steps with intermediate re-grindings.

Synthesis of $Ba_2Y_{0.85}WO_6$ through variation of sintering atmosphere

Attempts were made to synthesise the stoichiometric compound $Ba_2Y_1WO_6$ by varying the level of hydrogen gas in the synthesis atmosphere. This was achieved by mixing bottles of H_2 and Ar gas through a Y-shaped junction, according to the following equation:

$$[H_2] = \frac{f\,(H_2 \times 0.26)}{f\,(H_2 \times 0.26) + f\,(Ar \times 1.18)} \times 100\,\% \tag{4.2}$$

Where $f\,(H_2)$ and $f\,(Ar)$ are the apparent percentages of flow of H_2 and Ar repectively, read from flow metres, and 0.26 and 1.18 are conversion factors for the two gases [80], which take into account the effect of specific gravity on a gas on its flow rate. This gives a percent composition of the synthesis gas.

From a series of syntheses, 7.5% H_2/Ar was found to be most effective, giving apparent 85% yttrium occupancy (as found by X-ray diffraction, Section 4.3.1). Higher H_2 concentrations lead to broad, asymmetric peaks and high amorphous background contribution (Figure 4.4).

In their original synthesis of Ba_2YWO_6, Kamata *et al.* used "wet hydrogen" as the reducing atmosphere [71]. This method was attempted, bubbling hydrogen gas through water before introducing it into the furnace; however, no improvement in sample quality was seen over the use of 5 % H_2/Ar gas as described above.

Other attempted synthesis methods for $Ba_2Y_1WO_6$

Syntheses with increasing hydrogen concentration showed improvement in yttrium occupancy up to a certain point; beyond this, elemental tungsten was produced alongside non-stoichiometric $Ba_2Y_{1-\delta}WO_6$. A constant-oxidation synthesis, where the net oxidation state of the tungsten in the sample was not permitted to change over the course of the synthesis, was attempted.

$BaCO_3$ was calcined at 900 °C in air for two hours. This was added to a mixture of Y_2O_3 and tungsten oxides. WO_2 and WO_3 were mixed in a 1:1 ratio in order that the total mass of tungsten was stoichiometric and the net tungsten oxidation state was 5+. This mixture was pressed into a pellet, and sealed in a quartz tube under vacuum. The tube was then heated in a furnace at 1200 °C for 12 hours.

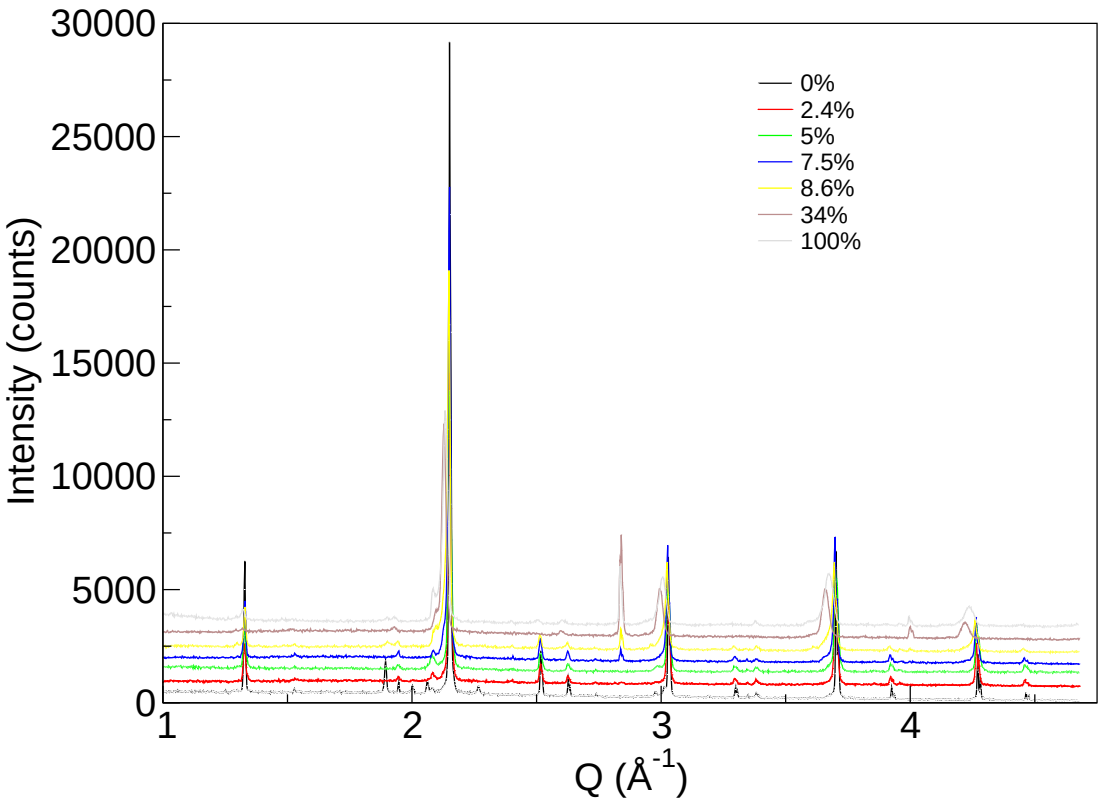

Figure 4.4 Effect of increasing hydrogen concentration on XRD pattern of $Ba_2Y_xWO_6$, with W^0 impurity at 2.8 $Å^{-1}$.

This synthesis was not successful: the resulting pellet was white, indicating a band insulator (W^{6+}), and X-ray diffraction showed a mix of many phases.

The synthesis was repeated, with the $BaCO_3$ and WO_3 calcined together before stoichiometric quantities of Y_2O_3 and WO_2 were added. This is because the calcination stage of the synthesis produces $BaWO_3$, rather than simply BaO. This synthesis was also unsuccessful, yielding a mixture containing rhombohedral $Ba_2Y_{\frac{2}{3}}WO_6$ as seen in Figure 4.5.

Similar synthesis were attempted with first aluminium, then tungsten metal powder (as described by Gardner and Danielson [81]) used as reducing agents in the quartz tube: these also failed to give the desired compound, showing a large W^0 impurity. Syntheses using a tungsten metal tube *within* the quartz tube, similar to that used in the synthesis of NaW_xO_3 [34], also showed this impurity.

A final attempt was made to synthesise $Ba_2Y_1WO_6$ using a large excess of tungsten metal, in contact with a pellet of stoichiometric quantities of $BaCO_3$, Y_2O_3, and a mixture of WO_3 and W, which was sintered in flowing Ar gas. This

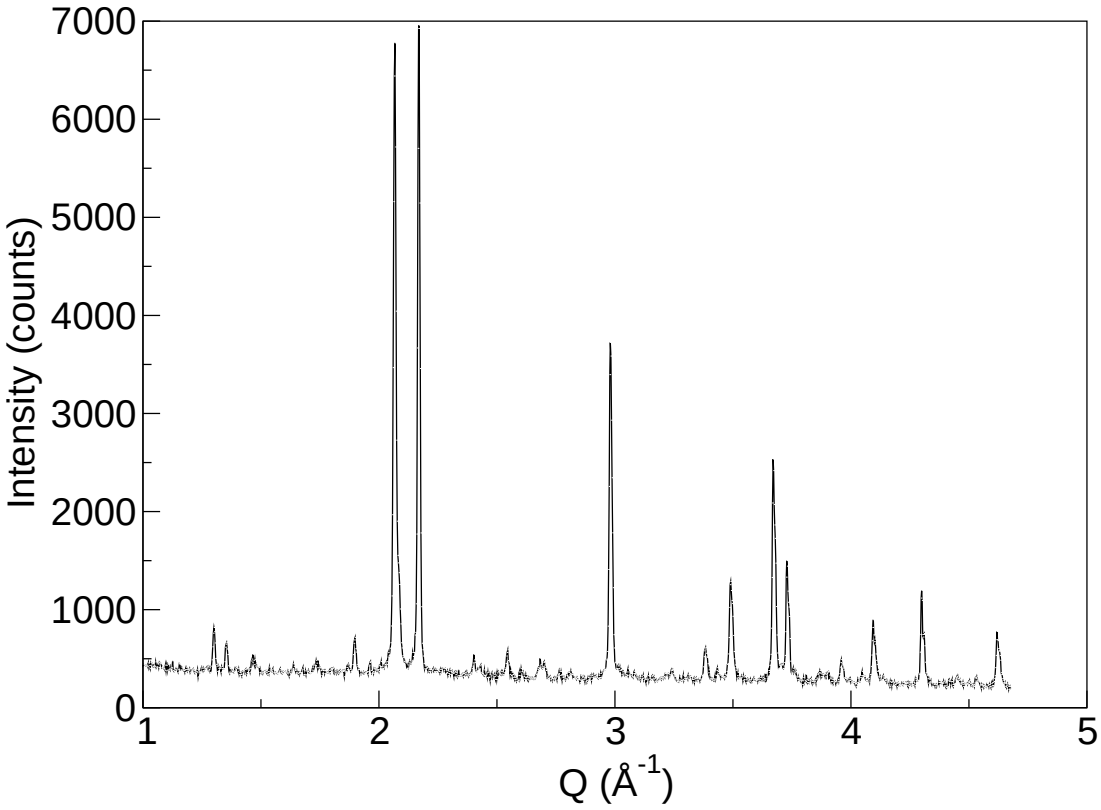

Figure 4.5 Product of unsuccessful synthesis attempt, showing rhombohedral $Ba_2Y_{\frac{2}{3}}WO_6$, with many other impurities.

resulted in difficulty in separating the final pellet from the surrounding W^0, and a large tungsten impurity in the product.

From the synthesis methods attempted, it became apparent that no synthesis method would yield a sample of $Ba_2Y_1WO_6$. Those methods relying on reducing gases resulted in only partial occupancy on the yttrium site, or, at higher H_2 concentrations, W^0 impurities. Synthesis in sealed quartz tubes, with or without the presence of oxygen "getters" in the form of pure Al or W, had the same effect, as did the final synthesis, with the pellet in physical contact with a tungsten metal excess. As will be described below, the effective range for yttrium occupancy in $Ba_2Y_xWO_6$ therefore appears to be $\frac{2}{3} \leq x \leq 0.78$.

Lithiation of $Ba_2Y_{\frac{2}{3}}WO_6$

Cubic $Ba_2Y_{\frac{2}{3}}WO_6$ was synthesised as described above, with a four-hour sinter step. Following this, an appropriate mass of $LiCO_3$, calculated in order to give the stoichiometry $Ba_2Li_{\frac{1}{6}}Y_{\frac{2}{3}}WO_6$ or $Ba_2Li_{\frac{1}{3}}Y_{\frac{2}{3}}WO_6$, was ground together with the pellet. The mixture was pressed into a new pellet, and sintered in 5 % H_2/N_2 for 12 hours at 1200 °C.

Synthesis of Ba_2NdWO_6

Like Ba_2YWO_6, Ba_2NdWO_6 has tungsten in the 5+ ($5d^1$) oxidation state. In this compound the neodymium ion is also magnetic: Nd^{3+} has electron configuration $[Xe]4f^3$. The introduction of valence f electrons into the system will have an effect on the magnetic properties of the compound: the aim was to investigate these, gaining an insight into the consequences of two strongly spin-orbit-coupled magnetic ions within a frustrated double perovskite lattice.

$BaCO_3$, Nd_2O_3 and WO_3 were ground together in stoichiometric quantities for a pellet of mass 0.5 g, calcined in air at 900 °C and, after regrinding, sintered in 5% H_2/N_2 gas at 1300 °C. Purity was assessed by X-ray diffraction, and the final step repeated with grindings until no improvement in the pattern was seen.

4.2.2 Analytical techniques

Neutron diffraction of $Ba_2Y_{0.75}WO_6$

High-resolution neutron diffraction on a powdered sample of $Ba_2Y_{0.75}WO_6$ was carried out on the HRPD beamline at ISIS. 4.7 g of sample was prepared as a 5 mm disc. The beamline is located 95 m from the target, allowing high resolution in backscattering geometry. The jaws of the guide were set at 15.05 mm by 19.98 mm, and data recorded as detailed in Appendix B, Table B.4.

Neutron diffraction of $Ba_2Y_{0.78}WO_6$ and $Ba_2Y_{\frac{2}{3}}WO_6$

$Ba_2Y_{0.78}WO_6$ and $Ba_2Y_{\frac{2}{3}}WO_6$ (cubic and rhombohedral phases) were measured on the D2B beamline at ILL, Grenoble. Sample masses were 2.24 g for $Ba_2Y_{0.78}WO_6$, 0.36 g for cubic $Ba_2Y_{\frac{2}{3}}WO_6$, and 1.82 g for rhombohedral $Ba_2Y_{\frac{2}{3}}WO_6$. Diffraction patterns of $Ba_2Y_{0.78}WO_6$ were taken at 3.5 K and 100 K using neutrons of 2.398 Å, and 3.5 K and 300 K using neutrons of wavelength 1.594 Å. Cubic $Ba_2Y_{\frac{2}{3}}WO_6$ was measured at 3.5 K and 300 K with 1.594 Å neutrons; rhombohedral $Ba_2Y_{\frac{2}{3}}WO_6$ was measured at 300 K only, using 1.594 Å neutrons.

Heat capacity measurements

Heat capacity measurements were carried out on a Quantum Design Physical Property Measurement System. A 14.4 mg sample of $Ba_2Y_{0.75}WO_6$ was prepared as a square plate, measuring no more than 1.5 mm × 1.5 mm, and affixed to a puck using Apiezon N grease. The heat capacity of the grease on the sample stage was first measured, as an addenda, before measurements of the sample were taken in zero-field and 9 T conditions. By subtracting the addenda measurement, the heat capacity of the $Ba_2Y_{0.75}WO_6$ sample was determined.

SQUID measurements

Magnetic susceptibility measurements were carried out on a Quantum Design Magnetic Property Measurement System XL. Samples were placed in a gelatin capsule and suspended within a straw.

Temperature-dependent measurements were carried out on cubic $Ba_2Y_{\frac{2}{3}}WO_6$, $Ba_2Y_{0.75}WO_6$, $Ba_2Y_{0.78}WO_6$, and Ba_2NdWO_6 (masses: $Ba_2Y_{\frac{2}{3}}WO_6$: 229.81 mg; $Ba_2Y_{0.75}WO_6$: 144.82 mg; $Ba_2Y_{0.78}WO_6$: 229.81 mg; Ba_2NdWO_6: 99.4 mg). In all cases, the magnetisation in an applied field was measured as the temperature was swept from 2 K to 400 K. Field-cooled and zero-field cooled measurements were taken for all samples: unless otherwise specified, these were identical at all temperatures. Details of the individual sweeps can be found in Appendix B, Table B.5.

Field-dependent measurements were taken from 0 kOe to 70 kOe, at a number of different temperatures between 2 K and 300 K. Full details are in Table B.5.

4.3 Results

4.3.1 X-ray diffraction

Ba_2YWO_6 compounds

X-ray diffraction was carried out on Ba_2YWO_6 compounds in order to determine the purity of the end products. The pattern of $Ba_2Y_{0.75}WO_6$ can be seen in Figure 4.2.

For the synthesis of the compound with variable yttrium occupancy, Figure 4.4 shows the XRD patterns without fits, demonstrating the change in peak quality as a function of H_2 concentration. At high H_2 concentrations in the synthesis atmosphere, a large peak, corresponding to metallic W^0, can be seen at $Q = 2.81\,\text{Å}^{-1}$. In addition to the appearance of this peak, a deterioration in the quality of those peaks which correspond to the $Ba_2Y_xWO_6$ phase can be clearly seen, with broadening and asymmetry peaks readily discernible, particularly at higher angle.

Key trends from this series of syntheses are seen in Figure 4.6. It can be seen that the refined Y-site occupancy does indeed increase with greater H_2 gas concentration in the synthesis atmosphere, but so too does the fraction of W^0 present. It should be noted that, since Y is relatively light compared to the other elements present, refinement of yttrium occupancy by XRD has a large error associated with it: far greater precision can be (and was) obtained through

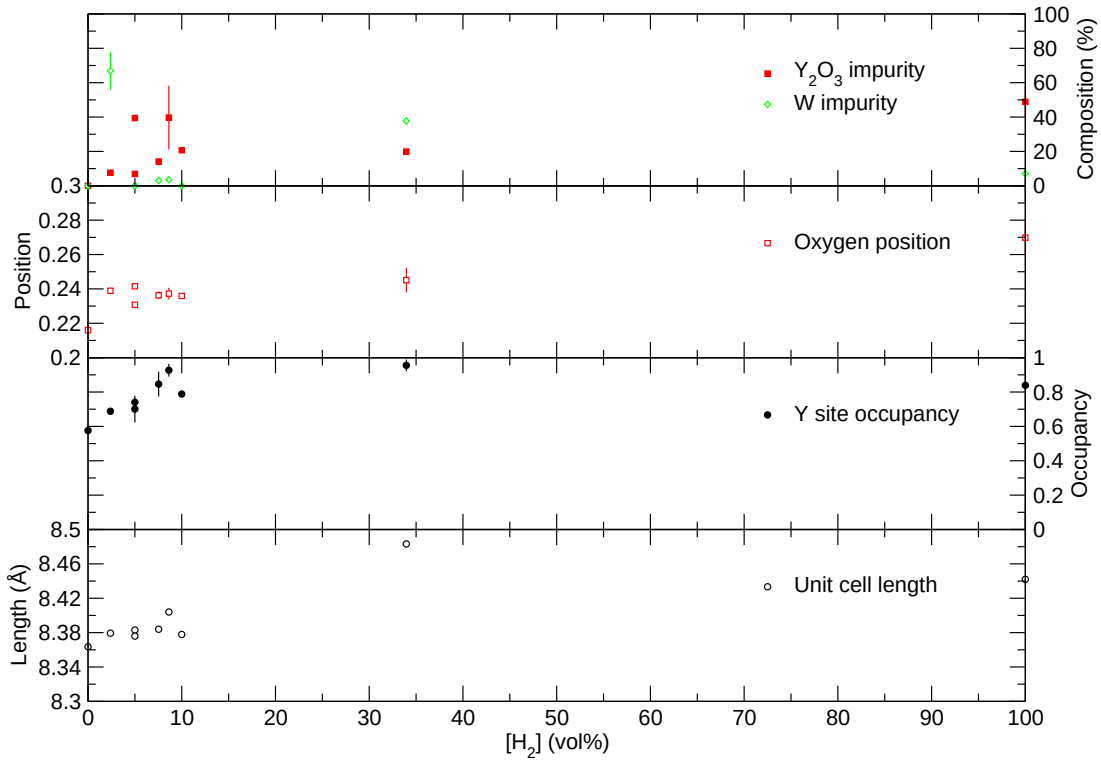

Figure 4.6 Refined model parameters for $Ba_2Y_xWO_6$ in different synthesis atmospheres.

neutron diffraction. From the results of these refinements, it was decided that the 7.5 % H_2 concentration gave the sample of greatest quality, after taking into account the refined yttrium occupancy of 85 %, and the phase fractions of Y_2O_3 and W^0 present – 15 % and 5 %, respectively. It was therefore this sample which was taken to ILL for high-resolution neutron powder diffraction measurements on D2B.

$Ba_2Y_{\frac{2}{3}}WO_6$ was also examined by X-ray diffraction, and was found to exist in one of two phases, depending on the number and length of sintering steps. Figure 4.3 shows the effect of these on the overall pattern. Analysis of the peak splitting here allowed determination of the shape of the unit cell of the non-cubic phase: since the (111) and (220) peaks split, but the (400) does not, the unit cell is rhombohedral. This has a lengthening of the body diagonal, leading to splitting of the (111) reflection to a (111) and $(11\bar{1})$ of different lengths.

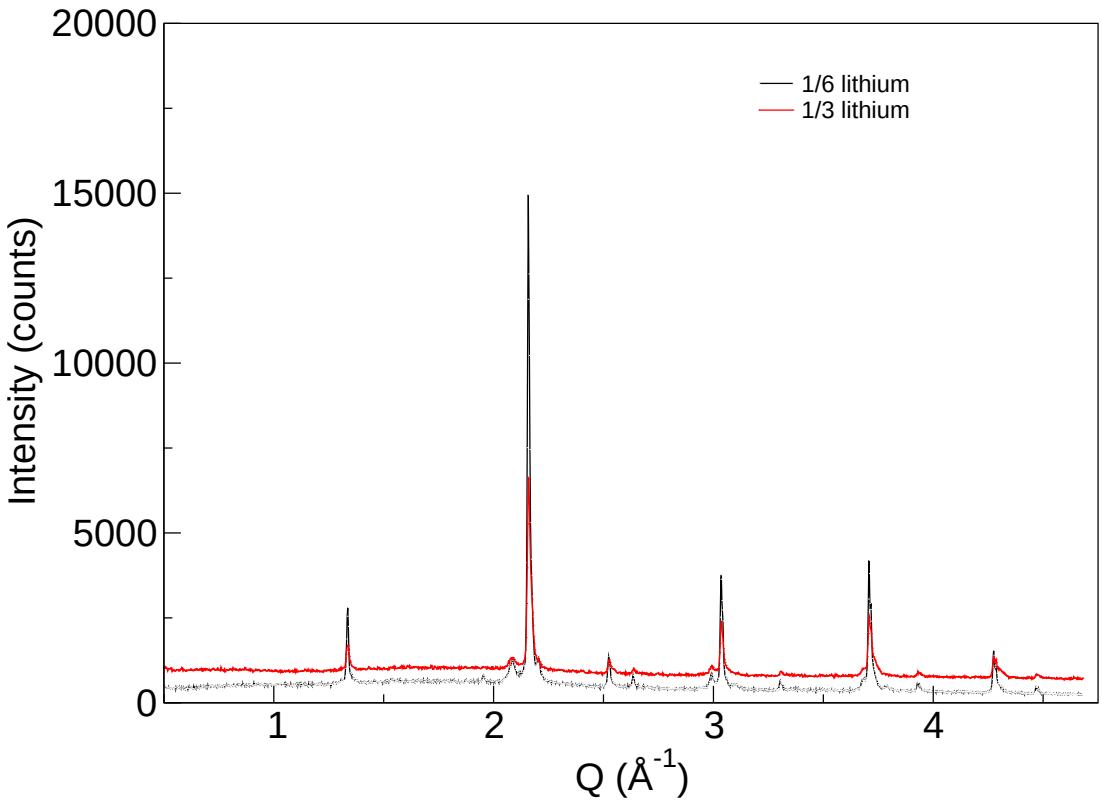

Figure 4.7 Change in diffraction pattern of $Ba_2Y_{\frac{2}{3}}WO_6$ after addition of $\frac{1}{6}$ and $\frac{1}{3}$ lithium equivalents.

Lithiated compounds

Due to the low electron count of lithium compared to the other elements present in the samples, the degree of lithiation of $Ba_2Y_{\frac{2}{3}}WO_6$ could not be determined by X-ray diffraction. The patterns are shown in Figure 4.7, which show no change in the structure of the compound upon sintering with lithium present, or with increased inclusion of lithium, except a degradation in the quality of the pattern. This suggests that lithiation stabilises the cubic phase, since comparison with Figure 4.3 suggests that two four-hour sinters should result in at least some visible splitting of the (111) peak. Confirmation of the inclusion of the lithium in the compound can be seen through the colour change in Figure 4.8, which shows the change from white $Ba_2Y_xWO_6$ to blue, with incorporation of lithium; however, the two lithiated compounds appear to be the same shade of blue. It is therefore impossible to tell whether the two compounds are indeed $Ba_2Li_{\frac{1}{6}}Y_{\frac{2}{3}}WO_6$ and $Ba_2Li_{\frac{1}{3}}Y_{\frac{2}{3}}WO_6$; only that *some* lithium has been included.

Figure 4.8 Left - right: $Ba_2Y_{\frac{2}{3}}WO_6$, $Ba_2Li_{\frac{1}{6}}Y_{\frac{2}{3}}WO_6$, $Ba_2Li_{\frac{1}{3}}Y_{\frac{2}{3}}WO_6$, showing colour change with addition of lithium to $Ba_2Y_{\frac{2}{3}}WO_6$. No significant change in colour is visible with increased target lithium content, however.

Ba_2NdWO_6

The X-ray diffraction pattern of Ba_2NdWO_6 is shown in Figure 4.9, with refinement results in Table 4.1. Since neodymium has a much higher electron count than yttrium, it is possible to accurately refine the occupancy of this ion, which was found to be 77.7(9) %.

This suggests that, as in $Ba_2Y_{0.78}WO_6$, the tungsten in Ba_2NdWO_6 is in the 5.67+ oxidation state, with one W(V) for every two W(VI) ions. Neutron diffraction on the sample would allow more confidence in this result, and also an examination of the effects of temperature on the structure. Since Nd^{3+} is magnetic, it is possible that ordering would be seen at low temperature, as the two B-site sublattices interact. However, no evidence of this is seen in magnetic susceptibility measurements: as Section 4.3.5 shows, no evidence of freezing is seen at any temperature. As discussed later, further magnetic measurements will be required in order to gain an understanding of the magnetism within Ba_2NdWO_6.

4.3.2 Neutron diffraction of $Ba_2Y_xWO_6$

Structural transition in $Ba_2Y_{0.75}WO_6$

Room-temperature and 10 K diffraction patterns can be seen in Figure 4.13. From the splitting of the peak at $Q = 3.000\,\text{Å}^{-1}$ (corresponding to (220) and (004) on a tetragonal unit cell, or (400) on the cubic unit cell), it can be seen that

Table 4.1 Refinement results of Ba_2NdWO_6 using Cu K_α radiation ($\lambda = 1.505\,\text{Å}$).

Temperature (K)	300
Space Group	$Fm\overline{3}m$
a (Å)	8.4923(2)
V (Å^3)	612.45(5)
Ba (0, 0.5, 0.25)	
B (Å^2)	0.02(15)
Nd (0, 0, 0)	
B (Å^2)	0.5(3)
W (0.5, 0, 0)	
B (Å^2)	1.9(1)
O (x, 0, 0)	
x	0.269(3)
B (Å^2)	1.8(6)
Y occupancy (%)	77.7(9)
R_p (%)	6.20
R_{wp} (%)	8.75
R_{exp} (%)	5.36
χ^2	2.694

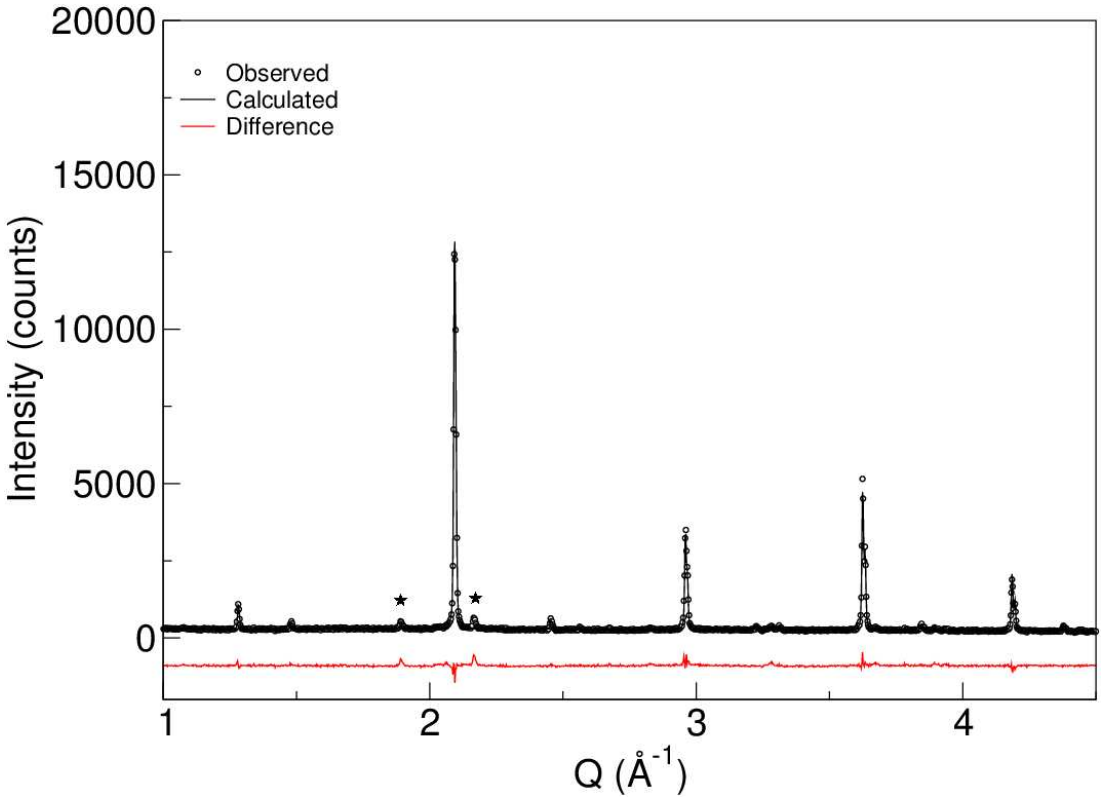

Figure 4.9 Fit of X-ray diffraction data of Ba_2NdWO_6, $\chi^2 = 2.694$. Impurities are shown by ★.

$Ba_2Y_{0.75}WO_6$ is tetragonal at low temperature, with $2\sqrt{c}/a = 0.996$ and space group I4/mmm. This small shift is visible due to the resolution of HRPD: $\frac{\delta d}{d} \approx 5 \times 10^{-4}$ for back-scattering data; $\frac{\delta d}{d} \approx 2 \times 10^{-3}$ for 90° data. Shorter scans were taken at 5 K intervals up to 300 K (Appendix B has a list of temperatures and acquisition times). Refinement of these allowed identification of the phase transition temperature within 5 K: 115(5) K.

Figure 4.10 shows the difference in M−O_{ax} and M−O_{eq} bond lengths as a function of temperature, whilst Figure 4.11 shows the geometry of the tetragonal unit cell ($\sqrt{2}c/a$) as a function of temperature: where this is equal to 1, the compound is cubic. Table 4.2 shows refinement parameters for the neutron diffraction scans taken at (10 K and 300 K), and Figure 4.12 shows the cubic structure of the compound at 300 K. The transition to I4/mmm is unusual, corresponding to small Jahn-Teller distortions of axial and octahedral bonds, and an absence of rotation of octahedra – in contrast to the tilted octahedra seen in the tetragonal (I4/m) Sr_2CuWO_6 discussed in Chapter 3, for instance. Figure 4.10 quantifies this small distortion, as the tungsten-oxygen axial bonds lengthen by approximately 0.06 Å compared to the cubic structure: this is accompanied by a contraction of

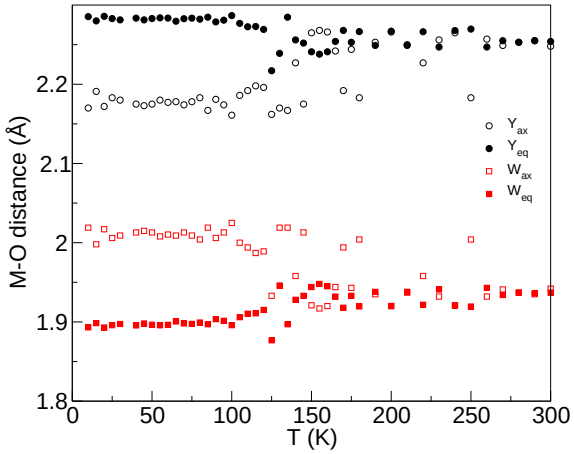

Figure 4.10 Change in M−O distance in Ba_2YWO_6 as a function of temperature.

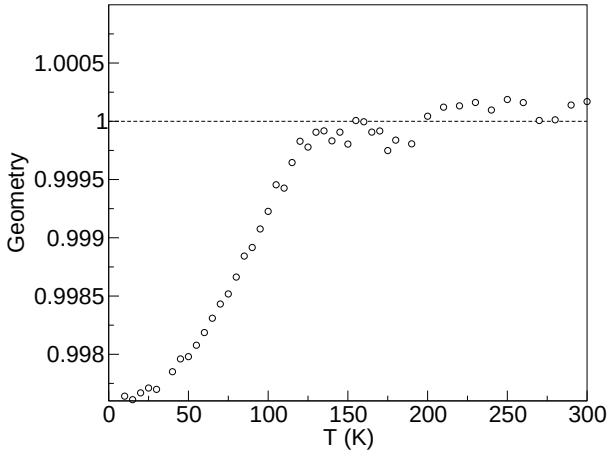

Figure 4.11 Change in geometry in Ba_2YWO_6 with temperature, identifying onset of small cubic to tetragonal transition at 115 K

equatorial tungsten-oxygen bonds of approximately 0.04 Å.

Structure of $Ba_2Y_{\frac{2}{3}}WO_6$

This compound was studied on the D2B beamline at ILL. From the patterns obtained (Figure 4.14), it can be seen that the cubic phase undergoes a transition to I4/mmm at low temperature, as was also seen in $Ba_2Y_{0.75}WO_6$. Scans at intermediate temperatures were not taken, so the temperature of the transition in this case is not known.

A room temperature scan of $Ba_2Y_{\frac{2}{3}}WO_6$ in the rhombohedral phase was also taken, and the structure refined. $Ba_2Y_{\frac{2}{3}}WO_6$ exists as an $R\bar{3}m$ compound, with an 18-layer unit cell arising from ordering of the yttrium vacancies. The pattern can

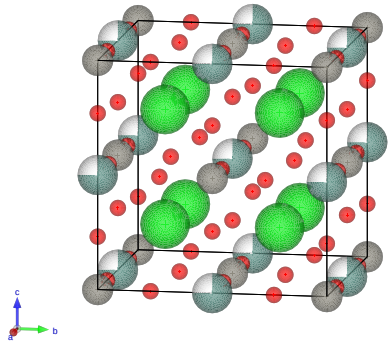

Figure 4.12 Cubic structure of $Ba_2Y_{0.75}WO_6$, showing partial occupancy of the yttrium sites, from refinement of neutron diffraction data at 300 K, $\chi^2 = 1.610$

Table 4.2 Refinement results of $Ba_2Y_{0.75}WO_6$ at 10 K and 300 K. Models were refined against data from two banks of HRPD.

T (K)	10	300
Space Group	I4 /mmm	Fm$\bar{3}$m
a (Å)	5.909 41(2)	8.381 20(12)
c (Å)	8.376 95(7)	
$\frac{\sqrt{2}a}{c}$	0.9976	
V (Å^3)	292.533(3)	588.734(25)
Ba (0, 0.5, 0.25)		
B (Å^2)	0.46(2)	1.59(6)
Y (0, 0, 0.5)		
B (Å^2)	0.20(5)	0.47(7)
Occupancy (%)	76(1)	76.9(4)
W (0, 0, 0)		
B (Å^2)	0.21(6)	0.86(10)
O1 (x, x, 0)		
x	0.2258(1)	0.230 85(13)
B (Å^2)	0.002(18)	1.36(6)
O2 (0, 0, z)		
z	0.2401(3)	
B (Å^2)	1.32(6)	
R_p (%)	3.94	9.82
R_{wp} (%)	4.63	10.14
R_{exp} (%)	2.75	9.14
χ^2	5.008	1.590

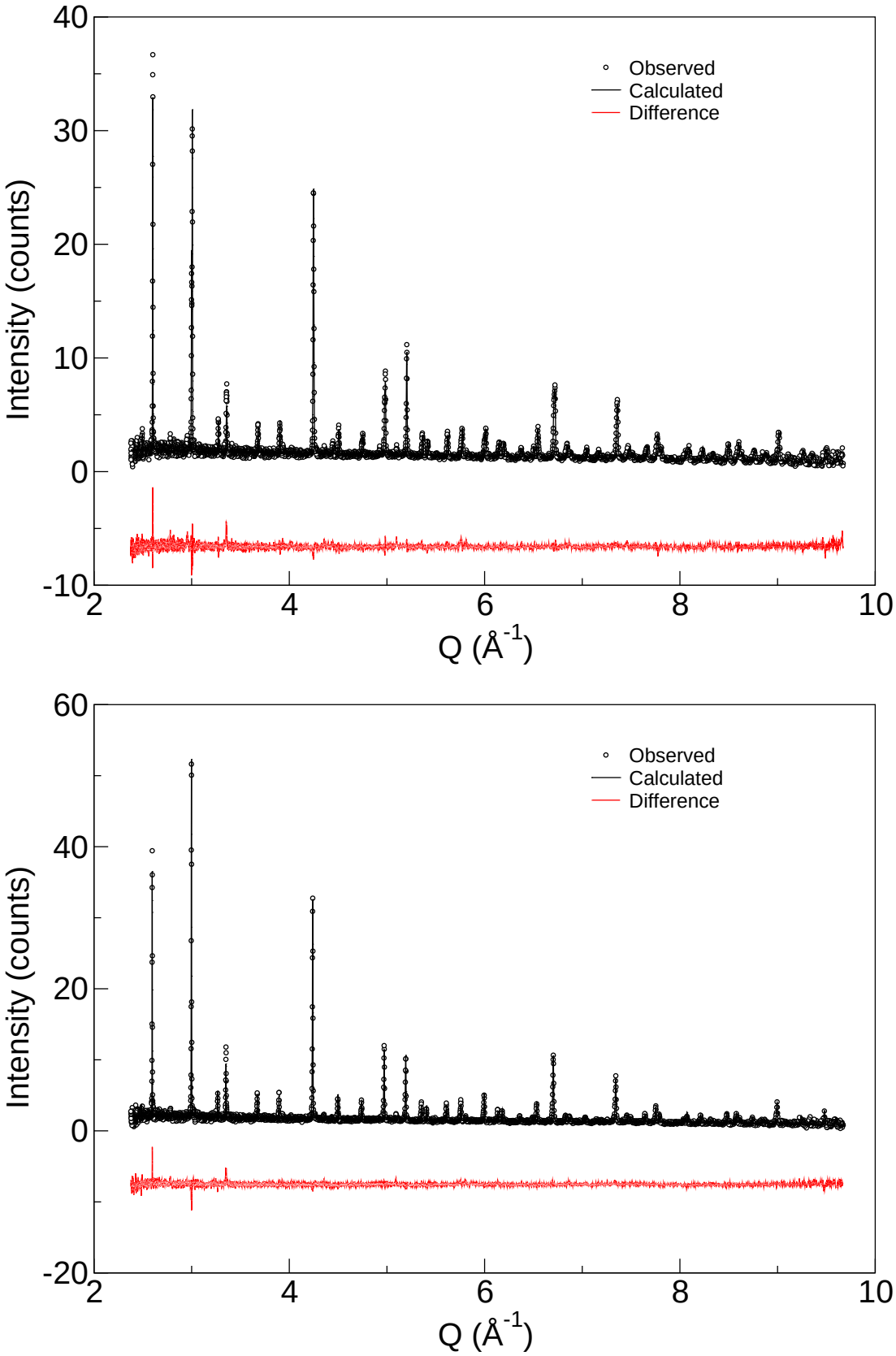

Figure 4.13 Neutron diffraction patterns of $Ba_2Y_{0.75}WO_6$ at 10 K (top, $\chi^2 = 1.735$) and 300 K (bottom, $\chi^2 = 1.610$), with fits to I4/mmm space group.

be seen in Figure 4.15, with obtained parameters in Table 4.3 and the structure shown in Figure 4.16. This phase exhibits $a^-a^-a^-$ octahedral tilting. The layers are stacked in a $(h_2c_4)_3$ "shifted"-type pattern.

Structure of $Ba_2Y_{\cdot 0.85 \cdot}WO_6$

The sample of $Ba_2Y_{0.85}WO_6$ (as refined from X-ray diffraction) was studied by neutron diffraction on the D2B beamline at ILL. Data were measured at 3.5 K, 100 K and 300 K. Neutrons of wavelengths 1.594 Å were used for the sample at 300 K; at the lower temperatures, 1.594 Å and 2.398 Å wavelength neutrons were used.

As can be seen from Figure 4.17, an impurity phase is visible at all temperatures. This can be fitted to a pattern of Ba_2YWO_6 with slightly different unit cell parameters; however, the low intensity of these broad peaks means the refinement of the yttrium occupancy of this phase is not possible. Details of the refinements of the dominant phase are given in Table 4.4.

From initial inspection of Table 4.4, it appears that there is no agreement between refinements regarding yttrium occupancy, which should be constant across different temperatures. From Figure 4.17, however, it can be seen that the data for the 100 K refinement is significantly poorer, statistically, then that for the 3.5 K and 300 K refinements: it is therefore likely that this pattern is not of high enough quality to accurately refine the yttrium occupancy. There is better agreement between the data at 3.5 K and 300 K: these patterns suggest an increased yttrium occupancy compared to that seen in the $Ba_2Y_{0.75}WO_6$ sample; possibly up to 78 % occupancy. This equates to an average tungsten oxidation state of 5.66+, which corresponds to one W^{5+} ion to every two W^{6+} ions (compared to a 1 : 3 ratio in $Ba_2Y_{0.75}WO_6$).

A transition from cubic $Fm\overline{3}m$ to tetragonal I4/mmm space group can be seen to occur between high and low temperature measurements. This is similar to that seen in $Ba_2Y_{0.75}WO_6$ and $Ba_2Y_{\frac{2}{3}}WO_6$; the exact temperature of the transition was not determined in this case, however.

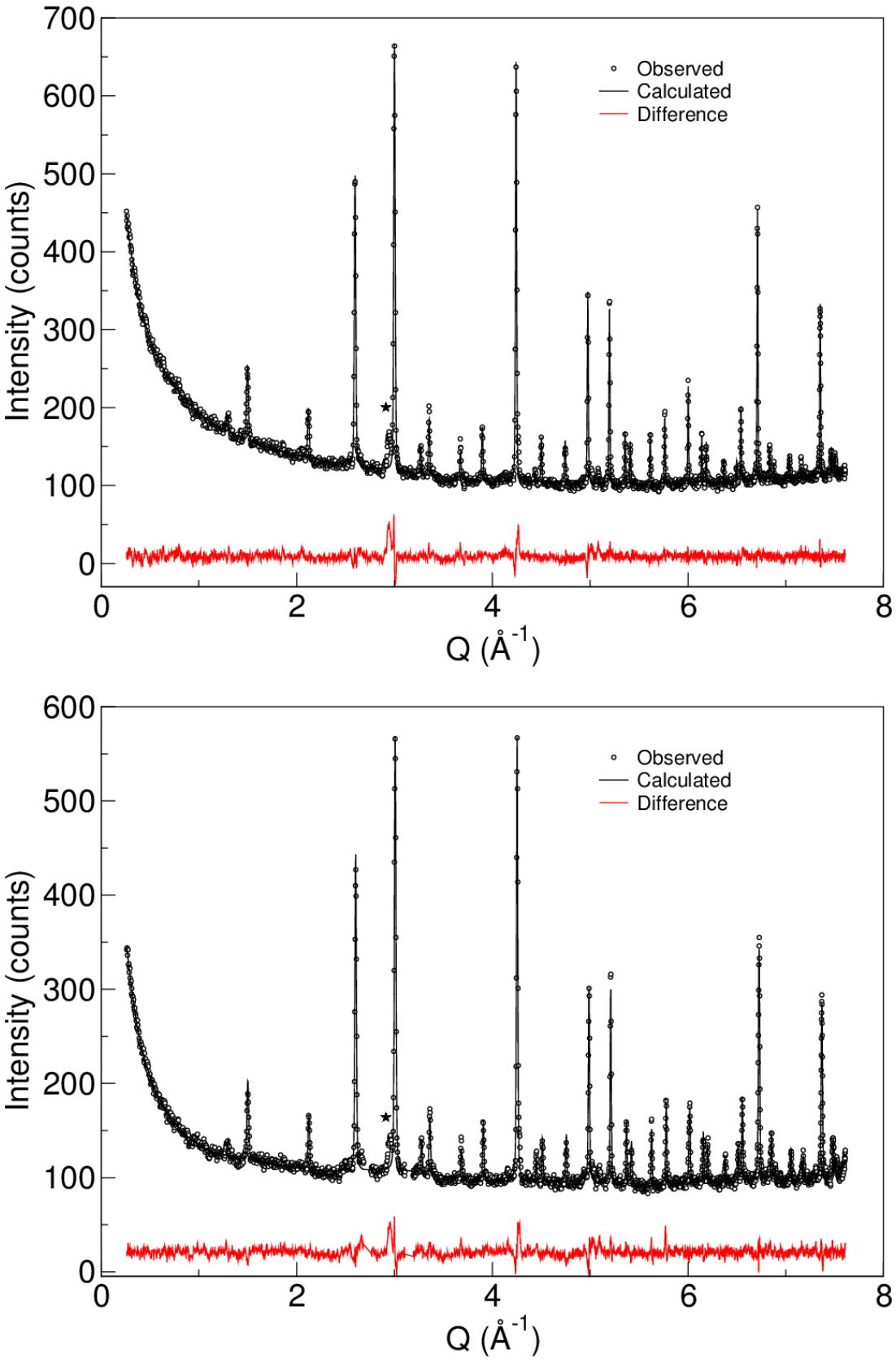

Figure 4.14 Neutron diffraction patterns of $Ba_2Y_{\frac{2}{3}}WO_6$ at 3.5 K (top, $\chi^2 = 1.827$) and 300 K (bottom, $\chi^2 = 2.167$), with fits to I4/mmm space group. Impurities are shown by ★.

Table 4.3 Refinement parameters of rhombohedral $Ba_2Y_{\frac{2}{3}}WO_6$.

T (K)	300
Space Group	R$\bar{3}$m
a (Å)	5.883 15(7)
c (Å)	42.7867(8)
V (Å^3)	1282.51(4)
Ba1 (0, 0, z)	
z	0.0871(2)
B (Å^2)	0.3(1)
Ba2 (0, 0, z)	
z	0.1875(2)
B (Å^2)	0.5(2)
Ba3 (0, 0, z)	
z	0.3650(2)
B (Å^2)	0.8(2)
Y (0, 0, z)	
z	0.2742(2)
B (Å^2)	0.83(8)
W1 (0, 0, 0)	
B (Å^2)	0.5(2)
W2 (0, 0, z)	
z	0.4499(2)
B (Å^2)	0.05(14)
O1 (x, $-x$, z)	
x	0.1743(5)
z	0.138 02(8)
B (Å^2)	0.49(5)
O2 (x, $-x$, z)	
x	0.1806(5)
z	0.2480(1)
B (Å^2)	1.00(8)
O3 (x, $-x$, z)	
x	0.1785(6)
z	0.6924(1)
B (Å^2)	0.33(6)
R_p (%)	6.04
R_{wp} (%)	7.81
R_{exp} (%)	5.00
χ^2	2.462

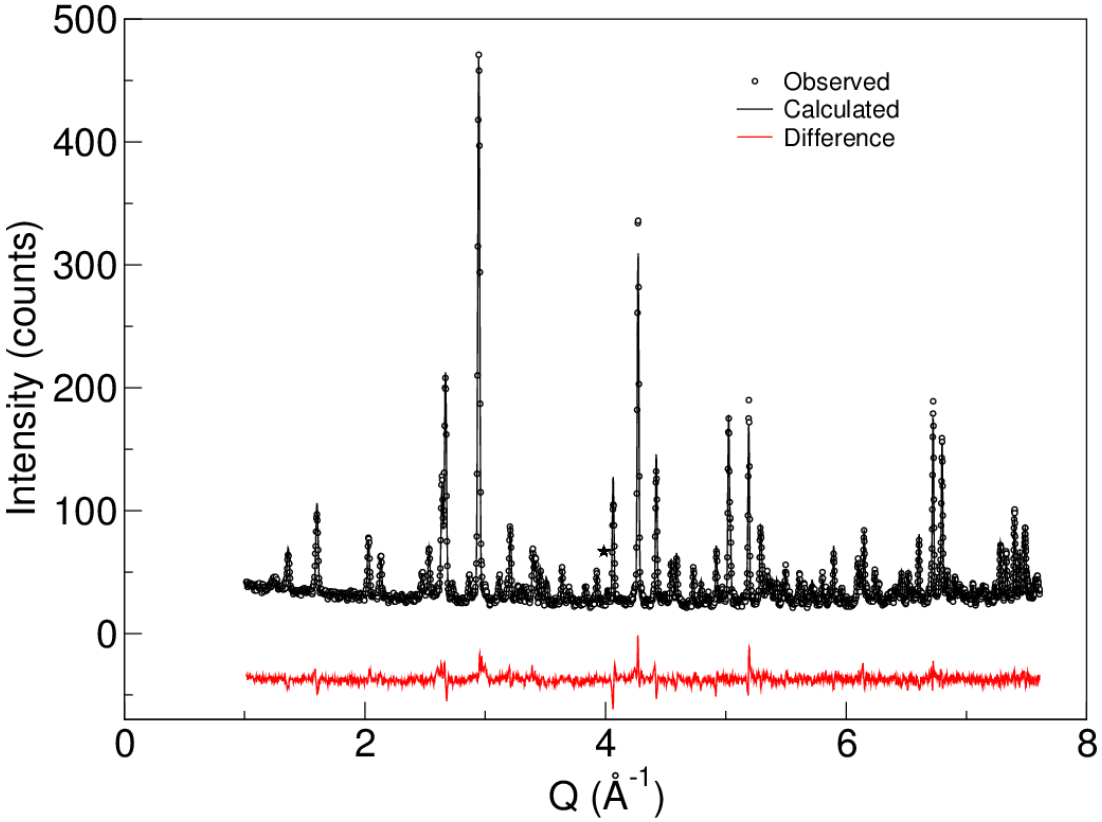

Figure 4.15 Rhombohedral phase of $Ba_2Y_{\frac{2}{3}}WO_6$, fitted to $R\bar{3}m$ space group. $\chi^2 = 2.444$. Impurities are shown by ★.

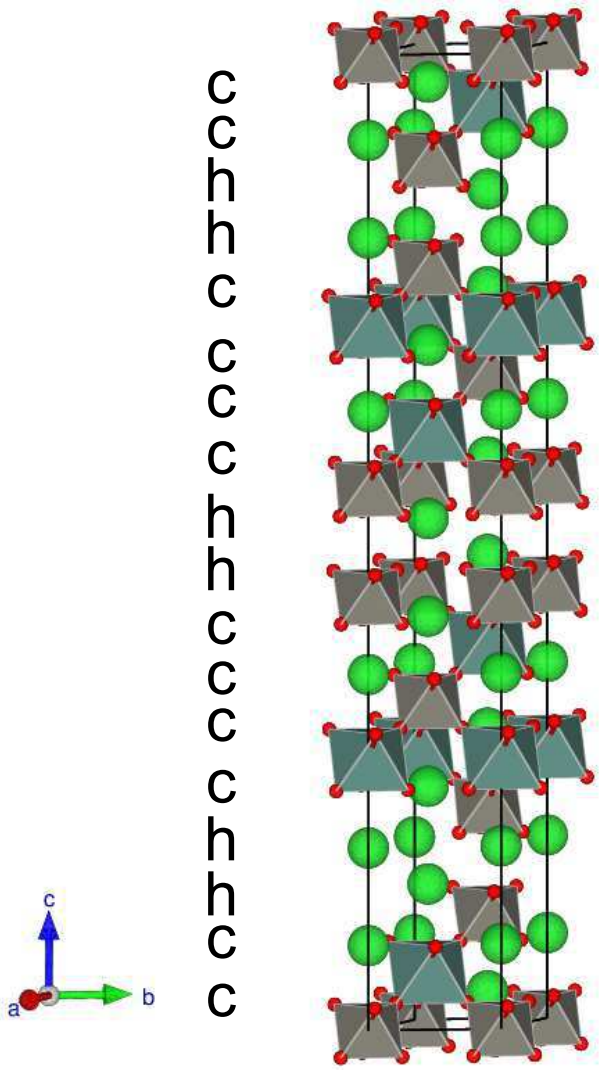

Figure 4.16 Structure of rhombohedral $Ba_2Y_{\frac{2}{3}}WO_6$, from neutron diffraction data at 300 K, $\chi^2 = 2.444$.

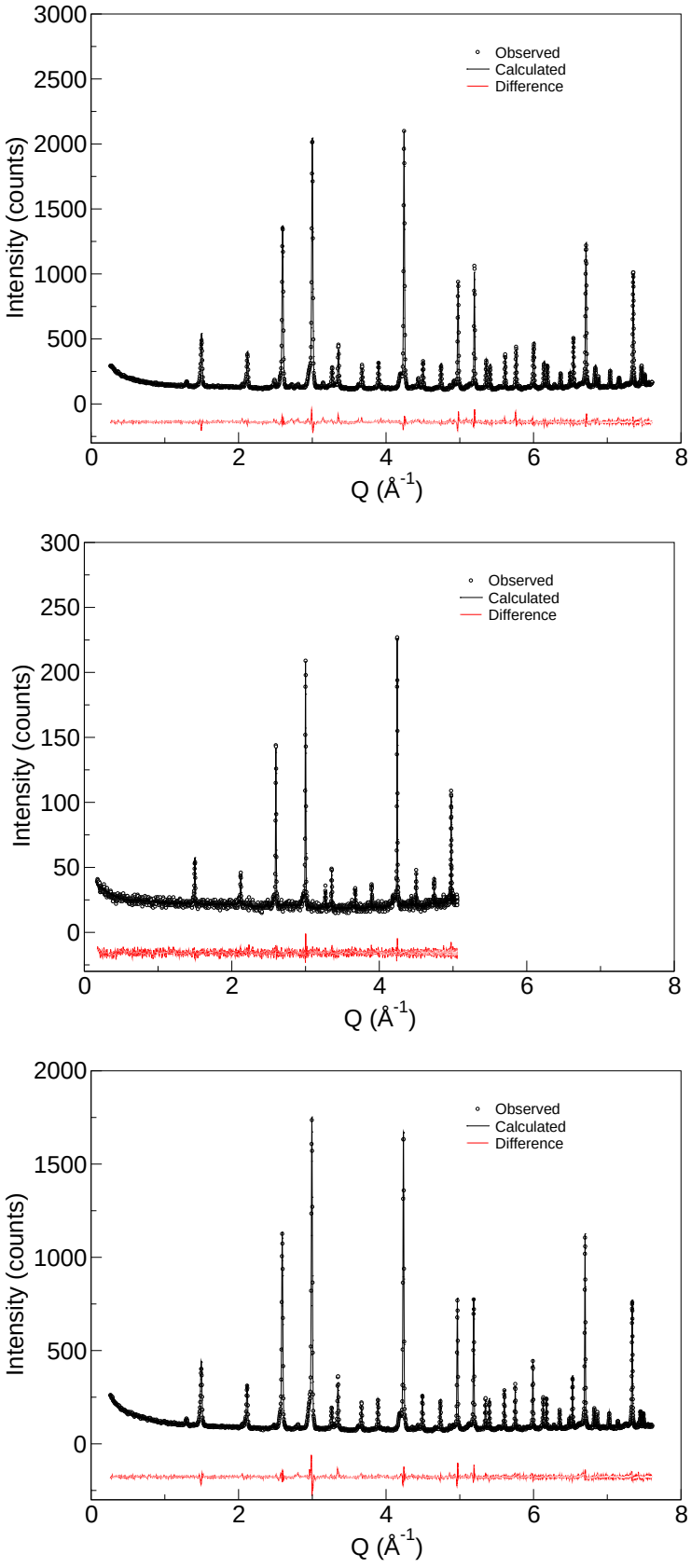

Figure 4.17 Neutron diffraction patterns of $Ba_2Y_{0.78}WO_6$ at 3.5 K (top, $\chi^2 = 2.527$), 100 K (middle, $\chi^2 = 0.7576$) and 300 K (bottom, $\chi^2 = 2.895$), with fits to I4/mmm space group. Note that the middle pattern is from neutrons of wavelength $\lambda = 2.4$ Å; top and bottom are of wavelength $\lambda = 1.5$ Å.

Table 4.4 Refinement results of $Ba_2Y_{0.78}WO_6$ at different temperatures. At 3.5 K, data from the two neutron wavelengths were refined simultaneously; at 100 K, the diffraction was of neutrons of wavlength 2.398 Å; and at 300 K, neutrons of wavelength 1.594 Å were used.

T (K)	3.5	100	300
Space Group	I4 /mmm	I4 /mmm	Fm$\bar{3}$m
a (Å)	5.918 153(4)	5.9235(3)	8.390 38(5)
c (Å)	8.382 89(9)	8.3794(6)	
Geometry ($\frac{\sqrt{2}a}{c}$, cubic is 1)	0.9475	0.9997	
V (Å^3)	293.645(4)	294.01(1)	590.669(10)
Ba (0, 0.5, 0.25)			
B (Å^2)	0.64(2)	0.5(1)	1.13(2)
Y (0, 0, 0.5)			
B (Å^2)	0.34(5)	0.9(3)	0.19(6)
W (0, 0, 0)			
B (Å^2)	0.04(4)	0.3(3)	0.42(5)
O1 (x, x, 0)			
x	0.2273(1)	0.2287(9)	0.231 06(9)
B (Å^2)	0.08(2)	0.2(3)	1.05(2)
O2 (0, 0, z)			
z	0.2397(4)	0.241(2)	
B (Å^2)	1.87(7)	1.5(9)	
Y occupancy (%)	77.8(5)	71(1)	75.5(6)
R_p (%)	3.44	5.69	3.55
R_{wp} (%)	4.77	6.96	4.74
R_{exp} (%)	3.96	7.99	2.84
χ^2	2.526	0.7692	2.810

4.3.3 Magnetic properties of $Ba_2Y_xWO_6$

Direct-current magnetic susceptibility measurements have been carried out on $Ba_2Y_{\frac{2}{3}}WO_6$, $Ba_2Y_{0.75}WO_6$ and $Ba_2Y_{0.78}WO_6$, in a range of fields. Scans of M(H) and M(T) were taken for all samples: a full list can be found in Appendix B, Table B.5.

The magnetic response in $Ba_2Y_xWO_6$ is derived from four separate components:

$$\begin{aligned} M(H,T) &= M_0 + \chi(T)H \\ \chi(T) &= \chi_{\mathrm{D}} + \chi_{\mathrm{CW}}(T) + \chi_{\mathrm{TIP}} \end{aligned} \tag{4.3}$$

Where $\chi(T)$ is the overall magnetic moment as a function of temperature, χ_{Dia} is the temperature-independent diamagnetic response of the sample, $\chi_{C-W}(T)$ is the temperature-dependent Curie-Weiss paramagnetic response of the sample, and χ_{TIP} is temperature-independent paramagnetism. M_0 is a soft ferromagnetic contribution, which saturates at $H \sim 10\,\mathrm{kOe}$ in each sample, and possibly arises from an impurity phase (a similar contribution is seen in Ba_2YMoO_6 [19]). In order to determine the overall nature of the magnetism in this family of compounds, therefore, multiple magnetic susceptibility measurements were carried out. $M(H)$ sweeps on $Ba_2Y_{\frac{2}{3}}WO_6$ allowed measurement of χ_{D}, whilst the soft ferromagnetic contribution was handled by taking a gradient between $M(T)$ measurements at 40 kOe and 60 kOe.

Determination of diamagnetic contribution to magnetic susceptibility

By measuring the $M(H)$ response in $Ba_2Y_{\frac{2}{3}}WO_6$ at a range of temperatures, the diamagnetic contribution to overall magnetisation in the $Ba_2Y_xWO_6$ series can be determined. $M(H)$ measurements were carried out at 100 K, 200 K, 300 K and 400 K, and can be seen in Figure 4.18. Straight-line fits to these data can also be seen ($M(H) = \chi_{\mathrm{D}} + M_0$), with the values of M_0 determined here listed in Table 4.5. Data were fitted only above 10 kOe, as a small soft ferromagnetic component can be seen at lower fields.

From these data, it can be seen that the diamagnetic susceptibility is, as expected, approximately constant with changing temperature, and has an

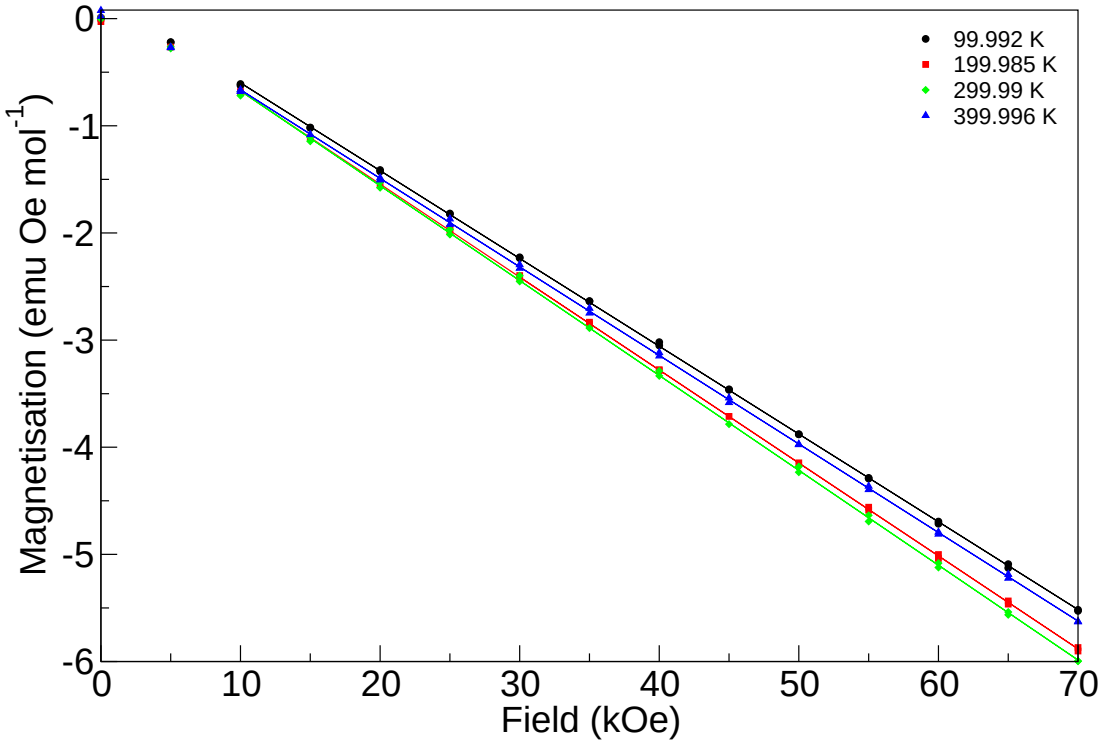

Figure 4.18 M(H) measurements on $Ba_2Y_{\frac{2}{3}}WO_6$, showing fits (straight lines) at each temperature to in fields above 10 kOe.

Temperature (K)	$\chi_{\mathrm{Dia}} \times 10^{-5}$(emu mol^{-1})	M_0 (emu mol^{-1})
100	−8.19(1)	0.220(6)
200	−8.68(2)	0.191(7)
300	−8.85(3)	0.212(12)
400	−8.26(2)	0.162(8)
Average	−8.5(4)	0.19(3)

Table 4.5 Parameters of the fit to the diamagnetic susceptibility in $Ba_2Y_{\frac{2}{3}}WO_6$.

average of $-8.5(4) \times 10^{-5}$ emu mol^{-1}. This can be compared with the theoretical diamagnetic susceptibility, calculated from Pascal's constants [82] shown in Table 4.6, which can be used to estimate diamagnetic susceptibilities:

$$\chi_{\mathrm{D}}(\mathrm{Total}) = \sum_i n_i * \chi_{\mathrm{D}_i} = -14.6 \times 10^{-5}\,\mathrm{emu\,mol^{-1}} \tag{4.4}$$

Although these values are in rough agreement, it can be clearly seen that, where the diamagnetic susceptibility is of interest itself (rather than simply as a correction to a further measurement), Pascal's constants do not give a sufficiently accurate value for χ_{Dia} to be used in further calculations.

Element	$\chi_{\mathrm{Dia}} \times 10^{-6} (\mathrm{emu\,mol^{-1}})$
Ba	-26.5
Y	-12
W	-16
O	-12

Table 4.6 Pascal's constants.

The value of χ_{Dia} will not change significantly with yttrium occupancy. According to Pascal's constants, $\chi_{\mathrm{Dia}}(\mathrm{Y}) = -12 \times 10^{-6}\,\mathrm{emu\,mol^{-1}}$; an increase from $x = \frac{2}{3}$ to $x = 0.8$ would therefore result in an increase in χ_{Dia_Y} of $1.6 \times 10^{-6}\,\mathrm{emu\,mol^{-1}}$, which is well within the error of the fit determined above.

Hence, for subsequent analysis it will be assumed that the diamagnetic susceptibility of the samples is $-8.5 \times 10^{-5}\,\mathrm{emu\,mol^{-1}}$, the χ_{D} for $\mathrm{Ba_2Y_{\frac{2}{3}}WO_6}$, as this sample does not have any paramagnetic spins.

Treatment of soft ferromagnetic moment

M(H) measurements on $\mathrm{Ba_2Y_{0.78}WO_6}$ show a soft ferromagnetic moment present in the sample at low field ($H < 10\,\mathrm{kOe}$)) As shown on the graph, this leads to inaccurate determination of χ as a function of field; however, above this field, the magnetisation follows a straight line. This soft ferromagnetic moment, labelled M_0, can be eliminated by taking a gradient between $M(T)$ data measured at 20 kOe and 60 kOe. Therefore, from Equation 4.3:

$$\begin{aligned} M(H,T) &= \chi(T)H + M_0 \\ \frac{\Delta M(H,T)}{\Delta H} &= \frac{M(H_1,T) - M(H_2,T)}{H_1 - H_2} \end{aligned} \tag{4.5}$$

This yields the magnetic susceptibility, χ, the components of which are described above.

It should be noted that this approach is not valid at low temperatures, as Figure 4.19 shows that magnetisation at 2 K is not linear with increasing field; rather, a Brillouin-like curve is seen. Furthermore, M_0 is very small compared to moment per mole, even in small fields and low temperature.

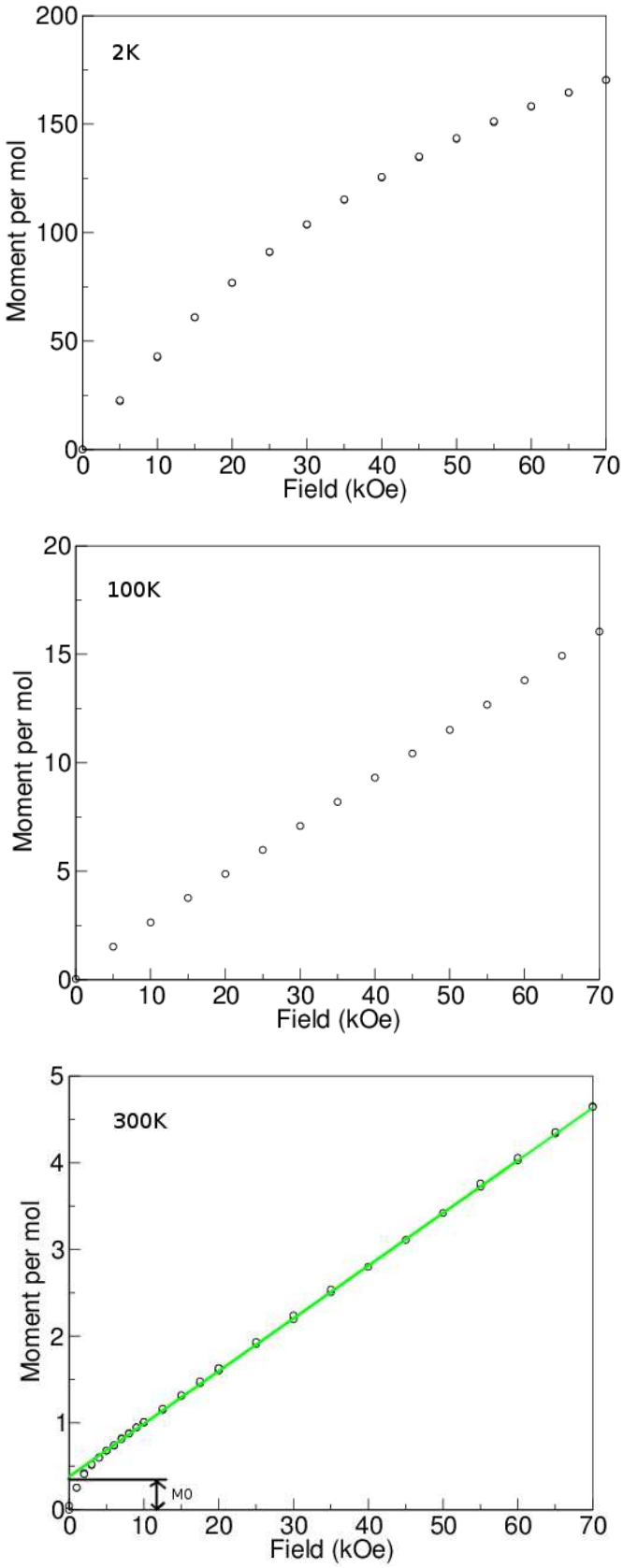

Figure 4.19 $M(H)$ graphs for $Ba_2Y_{0.78}WO_6$ at 2 K (top), 100 K(middle), and 300 K (bottom). Low-field detail on the 300 K graph shows the soft ferromagnetic contribution to magnetisation (green line).

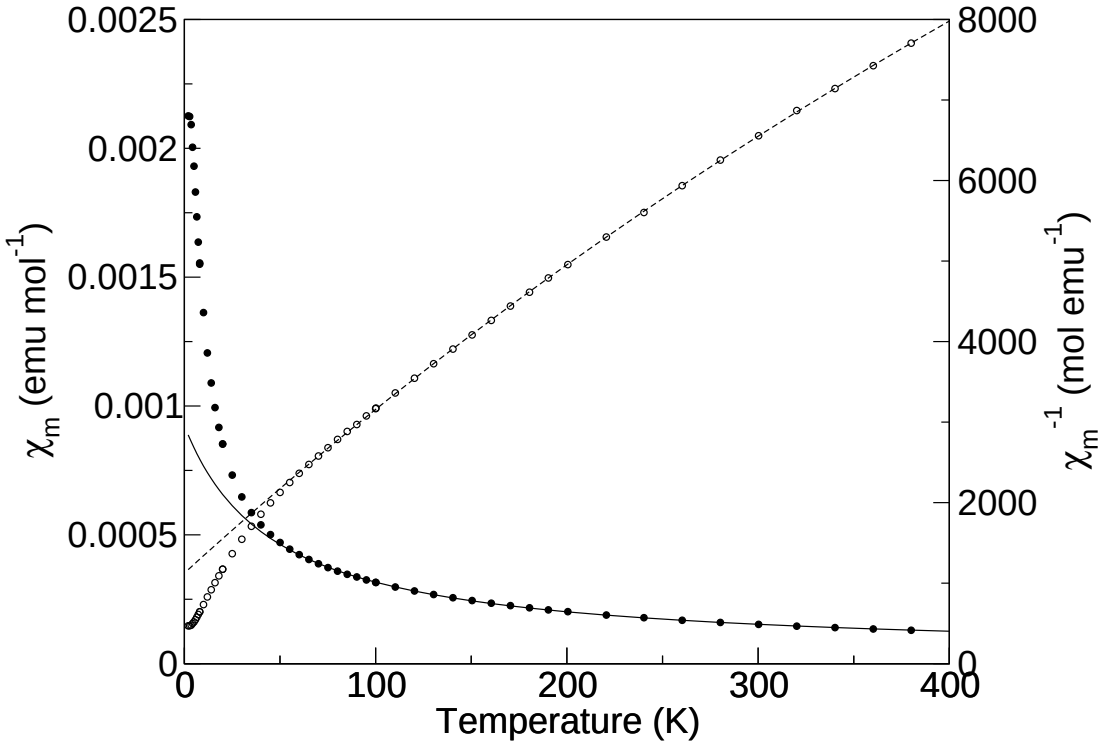

Figure 4.20 Magnetic susceptibility (filled circles, left axis) and inverse susceptibilty (open circles, right axis) of $Ba_2Y_{0.78}WO_6$ after subtraction of diamagnetic and soft ferromagnetic contributions, with fits to Equation 4.6 above 50 K

Fitting Curie-Weiss and temperature-independent paramagnetism

Following subtraction of M_0, it is possible to fit the magnetic susceptibility, χ_{Total} (Figure 4.20). Above 50 K, this can be fitted to a combination of Curie Weiss paramagnetism and a temperature-independent contribution, arising from the diamagnetic susceptibility and temperature-independent paramagnetism:

$$\begin{aligned} \chi_{\text{Total}} &= \chi_{\text{CW}} + \chi_0 \\ &= \frac{C}{T-\theta} + \chi_0, \end{aligned} \tag{4.6}$$

where the Curie constant, $C = 0.0403(6)\,\text{emu mol(f.u.)}^{-1}$, the Weiss constant, $\theta = -44(1)\,\text{K}$ and the temperature independent paramagnetic contribution, $\chi_{\text{TIP}} = 3.6(2) \times 10^{-5}\,\text{emu/mol}$ above 50 K. Attempting to fit the area below 50 K using the same method, with χ_{TIP} fixed, was not successful: this is not surprising because even at high temperature $\chi^{-1}(T)$ is clearly non-linear.

The value obtained for the Curie constant here, $0.0403(6)\,\text{emu mol(f.u.)}^{-1}$, is expressed in moles per formula unit. As described above, one in three tungsten ions in $Ba_2Y_{0.78}WO_6$ is W(V): the Curie constant per mole of magnetic ion is thus $0.121(2)\,\text{emu K mol(W)}^{-1}$, equating to an effective magnetic moment $\mu_{\text{eff}} = 1.0(1)\,\mu_B$ for W(V).

4.3.4 Heat capacity of $Ba_2Y_xWO_6$

Heat capacity measurements were carried out on a sample of $Ba_2Y_{0.75}WO_6$, and compared with data from the diamagnetic analogue, Ba_2TaWO_6 [83] (Figure 4.21). Comparing these allows the contribution to heat capacity from the single unpaired W^{5+} electron to be estimated. Figure 4.21 (top) shows $\frac{C_v}{T}$ for $Ba_2Y_{0.75}WO_6$, with the data for Ba_2TaWO_6 scaled so that the two are equal at 200 K (at which point the contribution from the unpaired electron on W^{5+} is taken to be negligible). The difference between these is also shown, and is integrated in the inset to the figure to give an estimation of the entropy derived from the magnetic contribution at 200 K: $S_{\text{mag}} = 15.4(4)\,\text{J K}^{-1}\,\text{mol(f.u.)}^{-1}$. This equates to a value per mole of W(V) of $61.6\,\text{J K}^{-1}\,\text{mol(W)}^{-1}$, suggesting a *much* higher magnetic entropy than expected for $J = \frac{3}{2}$ magnetic moments: $S = R\ln 4 = 11.56\,\text{J K}^{-1}\,\text{mol}^{-1}$. This increase in apparent magnetic entropy could be due to the fact that Ba_2TaWO_6, whilst a proposed diamagnetic analogue for $Ba_2Y_1WO_6$, is *not* a good analogue for the compound measured here, $Ba_2Y_{0.75}WO_6$. In fact, cubic $Ba_2Y_{\frac{2}{3}}WO_6$ would appear to be a closer analogue, having a smaller difference in the yttrium occupancy as well as tungsten, rather than tantalum, as the second B-site element. This raises its own difficulties, however: Figure 4.3 shows that obtaining pure cubic $Ba_2Y_{\frac{2}{3}}WO_6$ is difficult, and rhombohedral $Ba_2Y_{\frac{2}{3}}WO_6$, with layered ordering of vacancies, is expected to have a very different phonon spectrum from the vacancy-disordered cubic compounds.

Schottky anomaly in $Ba_2Y_{0.75}WO_6$

Between 2 K and 15 K, a small field dependence can be seen in the heat capacity (Figure 4.21). This can be modelled by a Schotkky anomaly, where the energy splitting between two or more discrete energy levels depends on the applied magnetic field.

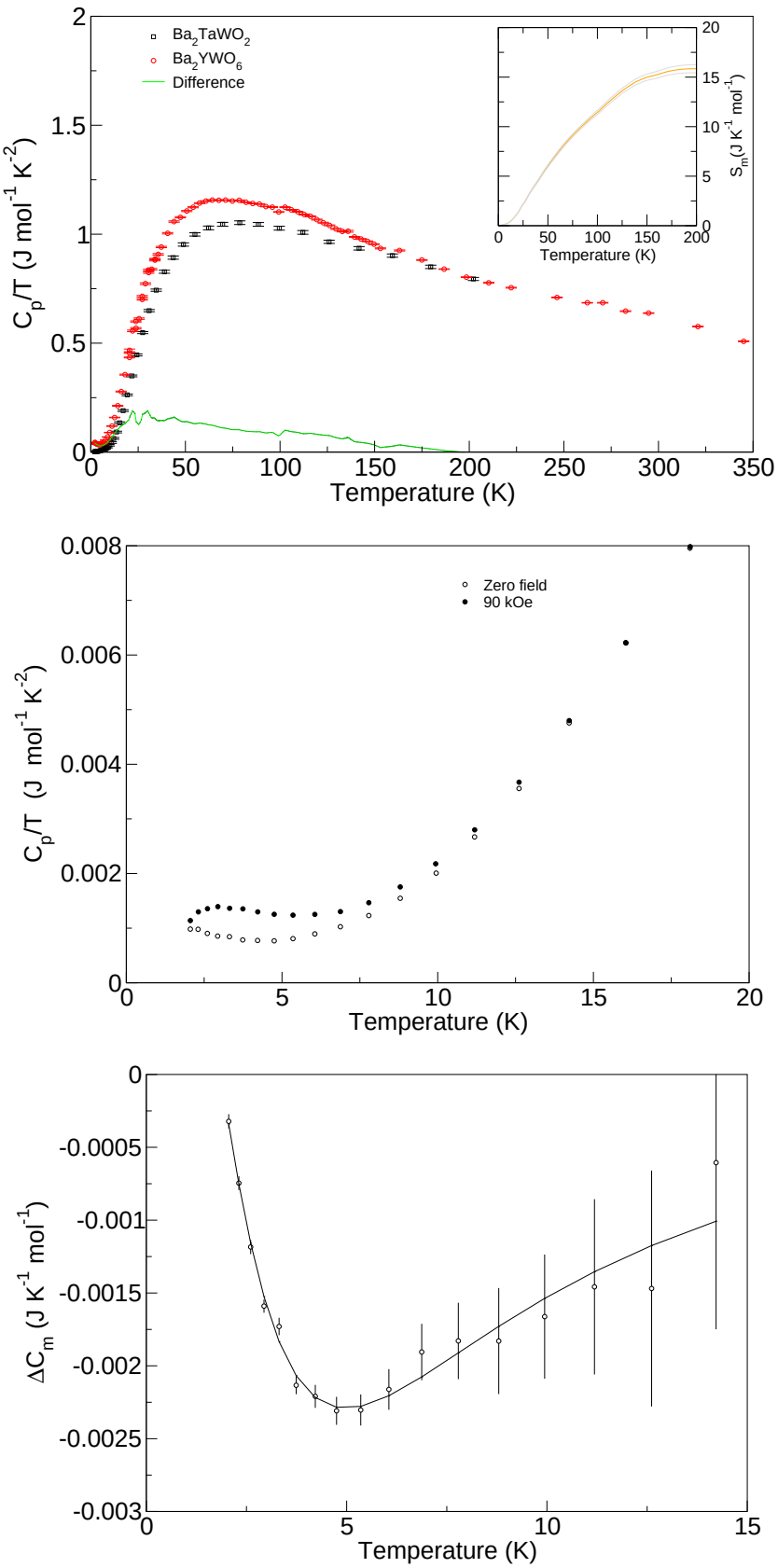

Figure 4.21 Top: Heat capacity of $Ba_2Y_{0.75}WO_6$, with subtraction of Ba_2TaWO_6 data and magnetic entropy (inset). Middle: Splitting arising due to Schottky anomaly in $Ba_2Y_{0.75}WO_6$. Bottom: Fit to Schottky anomaly in $Ba_2Y_{0.75}WO_6$.

f	0.041(2)
$E(0)$	0.08(4) K
$E(90)$	9.1(6) K

Table 4.7 Parameters of the fit to the Schottky anomaly in the heat capacity data of $Ba_2Y_{0.75}WO_6$. E_0 and E_90 represent the energy of splitting at0 kOe and 90 kOe, respectively.

The difference between the zero-field and 90 kOe data can be fitted by:

$$\Delta C_m = f\left(C_m(0) - C_m(90)\right) \tag{4.7}$$

where f is a scaling factor relating to the number of spins, and $C_m(H)$ is the Schottky anomaly contribution with appropriate energy level splitting in zero field and 90 kOe. Since the non-magnetic contributions are subtracted, the heat capacity with constant pressure, C_p, becomes the magnetic heat capacity, C_m. At low temperatures, C_m can be expressed as [84]:

$$C_m(H) \simeq \left(\frac{E(H)}{T}\right)^2 e^{-\frac{E(H)}{T}} \tag{4.8}$$

The fit is shown in Figure 4.21 (bottom), with the parameters in Table 4.7, and shows that 4.1(2) % of W spins are unpaired, relating to 16.4(8) % (4.1 % $\div \frac{1}{4}$) of W^{5+} spins. This is somewhat higher than the 8 % of spins which remain unpaired in Ba_2YMoO_6 [19]: the difference can be explained by the fact that the spins in $Ba_2Y_{0.75}WO_6$ are much more dilute, resulting in fewer viable near-neighbour pairings.

The energy of the splitting at 90 kOe is 9.1(6) K. The large error bars in the data at this point are a consequence of subtracting two data sets with a small difference.

4.3.5 Magnetic measurements on Ba_2NdWO_6

Preliminary magnetic susceptibility measurements were carried out on Ba_2NdWO_6, with the M(T) data shown in Fig. 4.22. M(T) data were taken in fields of 1 kOe and 10 kOe: based on more recent measurements on $Ba_2Y_{0.78}WO_6$, it is likely that these fall within the region below the saturation field of any soft ferromagnetic

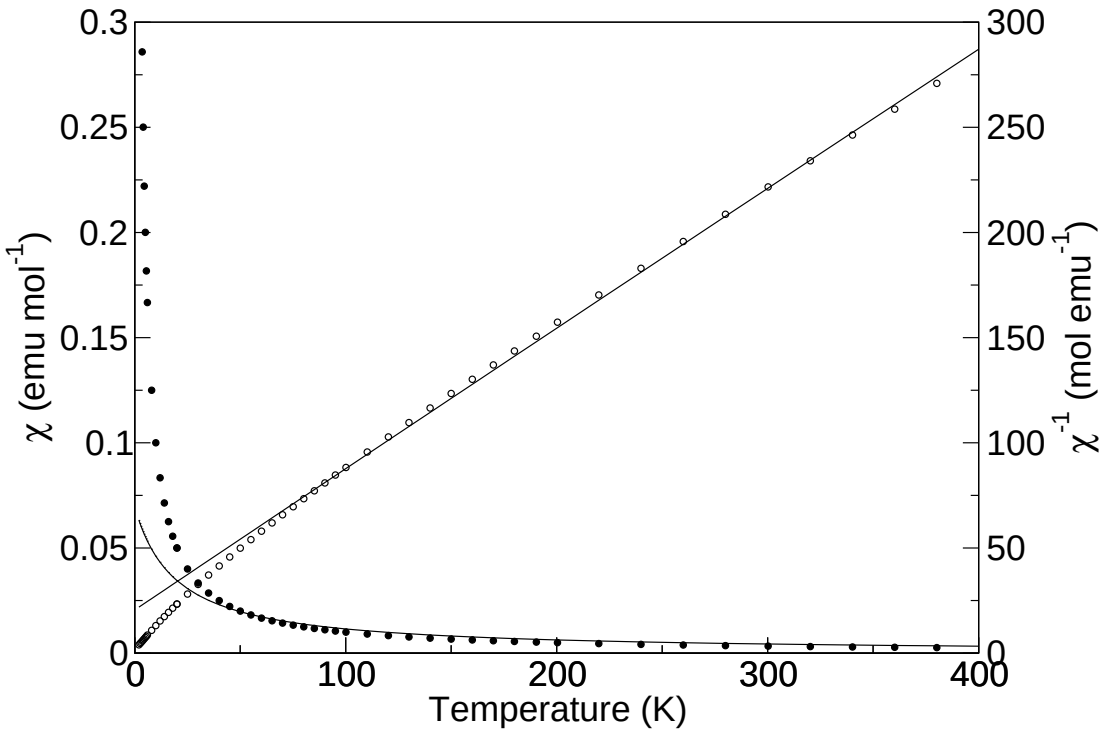

Figure 4.22 M(T) sweep of $Ba_2Nd_{0.77}WO_6$, showing fits (straight lines) to χ (left axis, closed circles) and χ^{-1} (right axis, open circles), as described in Equation 4.9.

moment present, similar to that seen in Ba_2YWO_6 and Ba_2YMoO_6 [19].

A linear combination of tungsten and neodymium contributions was used to fit these data, as follows:

$$\chi_m = \frac{C(\mathrm{W})}{T - \theta(\mathrm{W})} + \frac{C(\mathrm{Nd})}{T - \theta(\mathrm{Nd})} + \chi_{\mathrm{TIP}} \tag{4.9}$$

Fitting both χ and χ^{-1} according to this yielded slightly different parameters, shown in Table 4.8. $C(\mathrm{W})$, $\theta(\mathrm{W})$ and χ_{TIP} were fixed to their values determined from the fits to $Ba_2Y_{0.78}WO_6$ data. As can be seen from the figure, the fits are relatively poor at all temperatures. Further measurements, particularly at higher field, may allow for a better treatment of the data: it is likely that a soft ferromagnetic moment affects the data, as seen in $Ba_2Y_{0.75}WO_6$, resulting in an additional component. This accounts for the different shapes of the χ^{-1} data and fit: neither are linear (due to the addition of χ_{TIP}), but the shapes of the curves are different.

This discrepancy likely relates to the very low value of χ at high temperature,

	χ	χ^{-1}
C(Nd) (emu mol(f.u.)$^{-1}$)	1.34 ± 0.01	1.444 ± 0.009
C(Nd) (emu mol(Nd)$^{-1}$)	1.74 ± 0.01	1.88 ± 0.01
θ(Nd)(K)	-19.5 ± 0.9	-30 ± 1
μ_{eff}(Nd) (μ_{B})	3.7 ± 0.3	3.9 ± 0.3

Table 4.8 Parameters of fits to Ba_2NdWO_6 magnetic susceptibility data.

as well as the problems in fitting the data mentioned above. This is consistent with the poor fit at higher temperatures in χ^{-1} seen in Fig. 4.22. However, despite the relatively large difference in values for θ, μ_{eff} is consistent across the two fits. The value for μ_{eff}, $(3.7 \pm 0.3)\,\mu_{\text{B}}$, is in line with the expected value of $3.62\,\mu_{\text{B}}$ for neodymium [85]. Despite this agreement with expectations, further measurements would be required in order to improve confidence in the accuracy of these results, given the poor fit quality.

4.4 Discussion

4.4.1 Thermodynamic limits on the synthesis of $Ba_2Y_1WO_6$

From neutron diffraction measurements on $Ba_2Y_{0.78}WO_6$, it can be seen that two distinct phases of $Ba_2Y_xWO_6$ are synthesised in a 7.5 % H_2/N_2 reducing atmosphere. The yttrium occupancy of the second phase cannot be determined, due to the quality of peaks which make up this phase; however, from the results of other synthetic methods, it is unlikely that this second phase represents fully occupied yttrium sites. This suggests that, as attempts are made to synthesise $Ba_2Y_1WO_6$, at least two different phases of $Ba_2Y_xWO_6$ are formed, with different lattice parameters. The unit cell parameters (on an I4/mmm cell) for the secondary phase are $a = 5.9833(9)$ Å, $c = 8.52(1)$ Å, and thus $\frac{\sqrt{2}a}{c} = 0.993$. This suggests a larger unit cell than seen for the $Ba_2Y_{0.78}WO_6$ phase, and also a shift from the cubic ($\frac{\sqrt{2}a}{c} = 1$) geometry. It is therefore possible that this phase represents under-occupied Y sites, and the shift from cubic is caused by ordering of vacancies, as seen in $Ba_2Y_{\frac{2}{3}}WO_6$. This cannot be conclusively determined from the pattern, however, as the quality of the second phase is far too poor. It is unlikely that this second phase represents ordering of vacancies within $Ba_2Y_{0.78}WO_6$ itself: if this were the case, it would be expected that a similar impurity would be seen in $Ba_2Y_{0.75}WO_6$, which does not appear.

Entropic considerations in $Ba_2Y_1WO_6$

The entropy related to occupancies of yttrium sites, and consequently to positioning of W^{5+} within the lattice, can be expressed as the sum of entropies of mixing of yttrium/yttrium vacancies, and W(V)/W(VI) ions :

$$\Delta S_{\text{mix}}(Total) = \Delta S_{\text{mix}}\,(\text{Y}) + \Delta S_{\text{mix}}\,(\text{W})\,, \tag{4.10}$$

where the entropy of mixing, ΔS_{mix} can be determined by [84]:

$$\Delta S_{\text{mix}} = -nR\,(x_1 \ln x_1 + x_2 \ln x_2) \tag{4.11}$$

with x_1 and x_2 the molar fractions of the two components. Thus, $x_2 = 1 - x_1$, and so, for $\Delta S_{\text{mix}}\,(\text{Y})$:

$$\Delta S_{\text{mix}}\,(\text{Y}) = -nR\,(x_1 \ln x_1 + (1 - x_1)\,\ln\,(1 - x_1)\,) \tag{4.12}$$

Because the oxidation state of tungsten is dependent on the yttrium occupancy, a relationship can be drawn up. If y_1 is the proportion of W(VI) in $Ba_2Y_xWO_6$, then $y_1 = 3\,(1 - x_1)$. As with the yttrium sites, $y_2 = 1 - y_1 = 1 - 3\,(1 - x_1) = 3x_1 - 2$, and thus:

$$\Delta S_{\text{mix}}\,(\text{W}) = -nR\,(3\,(1 - x_1)\,\ln\,(3\,(1 - x_1)\,) + (3x_1 - 2)\,\ln\,(3x_1 - 2)\,) \tag{4.13}$$

Substituting Equations 4.12 and 4.13 into Equation 4.10 yields ΔS in terms of x_1:

$$\begin{aligned}\Delta S_{\text{mix}}(\text{Total}) = -nR(\,&(x_1 \ln x_1 + (1 - x_1)\,\ln\,(1 - x_1)\,) + \\ &(3\,(1 - x_1)\,\ln\,(3\,(1 - x_1)\,) + (3x_1 - 2)\,\ln\,(3x_1 - 2)\,)\,)\end{aligned} \tag{4.14}$$

This can then be plotted as a function of yttrium occupancy, the result of which is in Fig. 4.23. The maximum entropy of mixing is shown in the figure to fall

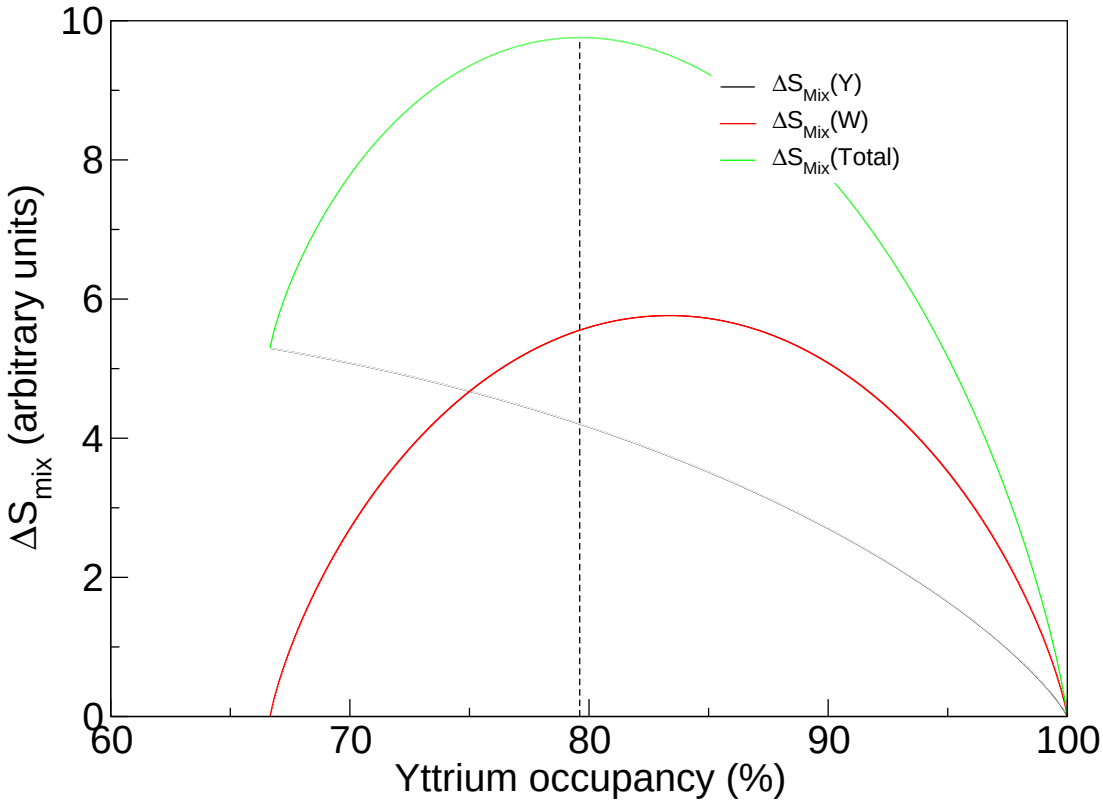

Figure 4.23 Entropic considerations in composition of $Ba_2Y_xWO_6$.

at $x = 0.80$, suggesting that with respect to entropy, the most favourable yttrium occupancy of $Ba_2Y_xWO_6$ is $Ba_2Y_{0.80}WO_6$. The findings presented here, with numerous unsuccessful attempts to synthesise $Ba_2Y_1WO_6$ described, suggest that this entropic contribution is a key factor in the thermodynamic stability of $Ba_2Y_xWO_6$. This also explains the difficulty in synthesising pure cubic $Ba_2Y_{\frac{2}{3}}WO_6$: that compound is entropically unfavourable, whereas the rhombohedral phase is stabilised thermodynamically (though not through ΔS_{mix}, as vacancies are ordered and no W(V) is present), and so begins to form as soon as some $Ba_2Y_{\frac{2}{3}}WO_6$ is present, albeit slower than the cubic phase.

4.4.2 Magnetic properties of the $Ba_2Y_xWO_6$ series of double perovskites

Derived values for the magnetic susceptibilities in $Ba_2Y_{0.78}WO_6$ are given in Table 4.9.

A Weiss temperature of $-44(1)$ K suggests strong antiferromagnetic interactions, though weaker than the $\sim$ 160 K seen in Ba_2YMoO_6 [18]. Above 50 K

χ_{Dia}	$(-8.5 \pm 0.4) \times 10^{-5}\,\mathrm{emu\,mol^{-1}}$
χ_{TIP}	$(3.6 \pm 0.2) \times 10^{-5}\,\mathrm{emu\,mol^{-1}}$
C	$(0.121 \pm 0.002)\,\mathrm{emu\,K\,mol(W)^{-1}}$
μ_{eff}	$(1.0 \pm 0.1)\,\mu_{\mathrm{B}}$
θ	$(-44 \pm 1)\,\mathrm{K}$

Table 4.9 Magnetic susceptibility parameters for $Ba_2Y_{0.78}WO_6$

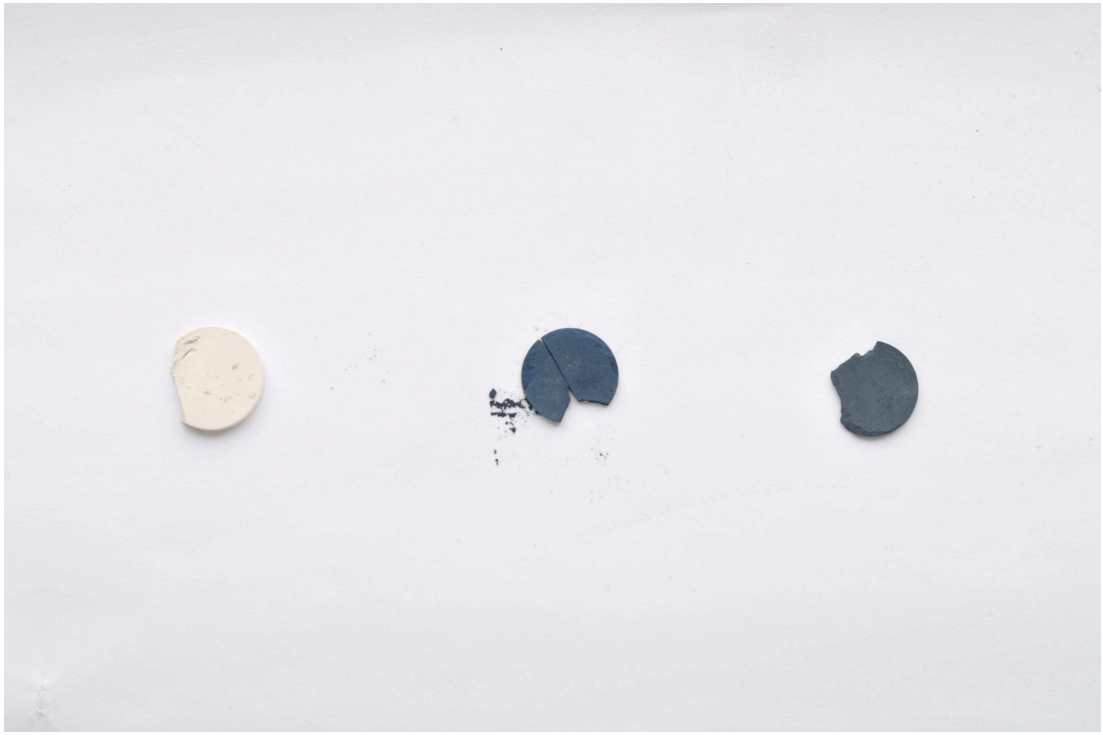

Figure 4.24 Change in colour in $Ba_2Y_xWO_6$ with decreasing tungsten oxidation state. Left-right: $Ba_2Y_{\frac{2}{3}}WO_6$, $Ba_2Y_{0.75}WO_6$, $Ba_2Y_{0.78}WO_6$.

the compound is closer in magnetic properties to the compound Ba_2NaOsO_6, which has Os^{7+} as the single magnetic ion, and $\mu_{eff} \sim 0.6\,\mu_{\mathrm{B}}$ [86]. Unlike $Ba_2Y_{0.78}WO_6$, however, Ba_2NaOsO_6 shows a strong transition in heat capacity measurements, with a magnetic transition at 6.8(3) K.

4.4.3 Colour changes in $Ba_2Y_xWO_6$

Figure 4.24 shows the change in colour of $Ba_2Y_xWO_6$ with increasing x (decreasing tungsten oxidation state). $Ba_2Y_{\frac{2}{3}}WO_6$, with W(VI), is a white band insulator: there are no unpaired electrons in the compound, and tungsten has configuration $[\mathrm{Xe}]5d^04s^0$. In the centre is $Ba_2Y_{0.75}WO_6$, with average tungsten oxidation state 5.75+, and one W(V) ($[\mathrm{Xe}]5d^14s^0$) to three W(VI). A dramatic

colour change can be seen between these two compounds as the tungsten oxidation state decreases. It has been suggested from studies on Li_xWO_3 that this is due to the filling of the W 5*d*–O 2*p* conduction band on reduction of tungsten [87].

The colour observed in $Ba_2Y_{0.78}WO_6$, which is very dark grey, is unlikely to be due to the further decreased tungsten oxidation state compared to $Ba_2Y_{0.75}WO_6$. Rather, it is probable that this black colouration arises from the W^0 impurity in the sample: powdered tungsten metal is dark grey. It is not, therefore, likely that colouration of pellets could be used as an indicator of the level of tungsten reduction, save in determining whether or not it has occurred: a $Ba_2Y_xWO_6$ sample in which no reduction from W(VI) has taken place will be white, one in which some reduction to W(V) has taken place will be blue, and one with strong W^0 impurities will be charcoal.

4.4.4 Rhombohedral structure of $Ba_2Y_{\frac{2}{3}}WO_6$

The thermodynamically stable structure of $Ba_2Y_{\frac{2}{3}}WO_6$ has been found to be rhombohedral: this is obtained via a kinetically favoured cubic structure, before the vacancies order into a shifted type structure with layering in an $(h_2c_4)_3$ pattern, and $a^-a^-a^-$ tilting (using Glazer notation [33]), as shown in Fig. 4.16. This is as expected for an $A_nB_{n-1}C_{3n}$ double perovskite with $n = 6$, as discussed by Trolliard *et al.* [74].

$Ba_2Y_{0.75}WO_6$ can also be thought of as a member of the $A_nB_{n-1}C_{3n}$ family, with $n = 8$ ($Ba_8Y_3W_4O_{24}$). Unlike $Ba_2Y_{\frac{2}{3}}WO_6$, however, $Ba_2Y_{0.75}WO_6$ showed no signs of vacancy ordering, despite multiple sinters over long time periods. The $n = 8$ double perovskite $Ba_8Ti_3Ta_4O_{24}$, however, *does* show vacancy ordering, with phase purity achieved after a ~ 100 hour sinter in air [88]. That compound is hexagonal, with space group $P6_3/mcm$, and a superstructure caused by the vacancy ordering. The cubic nature of $Ba_2Y_{0.75}WO_6$ suggests that no such ordering would be seen, even were longer sinters to be carried out ($Ba_2Y_{\frac{2}{3}}WO_6$, for instance, shows a phase corresponding to vacancy ordering within four hours).

4.4.5 Lithiation of $Ba_2Y_{\frac{2}{3}}WO_6$

The cubic structure of $Ba_2Li_{\frac{1}{6}}Y_{\frac{1}{3}}WO_6$ appears to be stable with repeated sintering steps on incorporation of lithium ions, unlike cubic $Ba_2Y_{\frac{2}{3}}WO_6$ with vacancies.

It is likely that the addition of lithium stabilises the ordering of vacancies (if any remain). No divergence from a cubic unit cell could be seen from the X-ray diffraction patterns reported here: neutron diffraction patterns would allow determination of any deviation from $Fm\bar{3}m$ symmetry to be seen, along with any ordering of lithium ions.

Lithiation of $Ba_2Y_{\frac{2}{3}}WO_6$ is expected to result in tungsten oxidation states of 5.67+ (in the case of one-third lithiation) and 5.83+ (where lithiation is one-sixth). Figure 4.8 shows a grey-blue pellet, rather than the darker blue seen in $Ba_2Y_{0.78}WO_6$. If the colour of the compound is due largely to the tungsten oxidation state – as appears likely due to the colour change between the white band insulator $Ba_2Y_{\frac{2}{3}}WO_6$ and the dark blue Mott insulator $Ba_2Y_{0.78}WO_6$ – an estimation can be made from the colour of lithiated $Ba_2Y_{\frac{2}{3}}WO_6$ that the tungsten oxidation state has *not* reached 5.67+, as it is in $Ba_2Y_{0.78}WO_6$, or even the 5.75+ present in $Ba_2Y_{0.75}WO_6$. Even before neutron diffraction measurements are made, it can be deduced that complete occupation of the *B*-site in this compound is not attained.

4.5 Conclusions

The target compound, the stoichiometric $Ba_2Y_1WO_6$ has not been synthesised. Numerous attempts using different methods have allowed the creation of a speculative phase diagram, from which a miscibility gap in the four-element system can be proposed. It is suggested that the difficulty in synthesising $Ba_2Y_1WO_6$ arises in part due to the entropic advantage of a partially occupied system. The most reduced compound successfully synthesised in $Ba_2Y_{0.78}WO_6$, which has an average tungsten oxidation state of 5.67+, suggesting one W^{5+} for every two W^{6+} ions.

The mixed-valence compounds $Ba_2Y_{0.75}WO_6$ and $Ba_2Y_{0.78}WO_6$ show no magnetic freezing at any temperature in magnetic susceptibility measurements, remaining paramagnetic at all temperatures. This is further confirmed by the lack of any signature of a transition in heat-capacity measurements (in the case of $Ba_2Y_{0.75}WO_6$) or neutron diffraction measurements (carried out on both $Ba_2Y_{0.75}WO_6$ and $Ba_2Y_{0.78}WO_6$). High-resolution neutron diffraction measurements on $Ba_2Y_{0.75}WO_6$ show a transition from cubic $Fm\bar{3}m$ to tetragonal I4/mmm space group with cooling. Neutron diffraction scans taken at small

intervals have allowed the temperature of this transition to be determined as 115 K, and the change in geometry ($\frac{\sqrt{2}a}{c}$)of the unit cell from 300 K to 9 K is only 0.24 %, a very small lengthening in the c axis. In $Ba_2Y_{0.78}WO_6$ at 3.5 K, a larger change of 5.25 % is seen. It is likely that this change arises due to the larger proportion of W(V), an ion with one unpaired electron (and therefore Jahn-Teller active) in the compound: no tilting of octahedra, such as is seen in Sr_2CuWO_6 [52], is observed in this compound.

Lithiation of $Ba_2Y_{\frac{2}{3}}WO_6$ appears, from a strong colour change and stabilisation of the cubic phase, to have been successful, with at least partial occupancy of the B site by lithium ions. This raises the possibility of lithium ion mobility within the compound, as inspection of the colour of the compound compared to $Ba_2Y_{0.75}WO_6$ suggests that some B sites remain vacant. Neutron diffraction studies on the two lithiated compounds would allow accurate determination of the level of lithium incorporation into the $Ba_2Y_{\frac{2}{3}}WO_6$ structure.

Chapter 5

Synthesis of $LaSrMgWO_6$

5.1 Introduction

Like Ba_2YWO_6, $LaSrMgWO_6$ is a double perovskite with the heavy W^{5+} magnetic ($5d^1$) ion, where strong spin-orbit coupling is expected to be seen in magnetic properties. The compound was first reported by Yoshimura *et al.* [89]: this is the same group as initially synthesised Ba_2YWO_6. This compound has a tolerance factor $t = 0.85$, much lower than the $t = 0.91$ of Ba_2YWO_6.

$LaSrMgWO_6$ was of interest because it also presented the possibility of *A*-site ordering in a double perovskite: whilst *B*-site-ordered double perovskites are common, *A*-site ordering is less frequent [31], and tends to be layered rather than rocksalt ordered. The compound had been previously reported as "pseudo-cubic" (with $a = 7.922\,\text{Å}$). The aim of the current synthesis was to determine the reproducibility of these previous studies, in an attempt to synthesise a W^{5+} double perovskite. Neutron diffraction would then be used to study the physical and (if applicable) magnetic structure at a range of temperatures, and magnetic measurements would allow probing of magnetic properties below 80 K, the limit of the measurements made in previous studies.

5.1.1 A-site ordering in double perovskites

Rocksalt ordering of B-site cations in double perovskites is relatively common, occurring in compounds where the two B-site ions have a charge difference of

greater than three, or a difference in atomic radius of 0.26 Å or greater [29, 30]. In compounds with differing atoms on the A-site, such as $LaSrMgWO_6$, *A*-site ordering is possible, but rarely seen [31].

When considering ions in double perovskites, three types of ordering can be seen. The most commonly observed where *B* ions order is rocksalt ordering, with alternating B and B' ions throughout the lattice. Columnar ordering, with columns of *B* and *B*′ (or *A* and *A*′) extending along one axis, is also observed, though this is less common. Finally, layered ordering has alternating layers of *B* and *B*′ (or *A* and *A*′) ions throughout the compound.

Rocksalt ordering

This is described by King and Woodward as "0D" ordering, as each *B* ion is separated from similar ions by intermediate *B*′ ions. It can also be considered (111) ordered, as this is the plane along which like ions lie. *B*/*B*' rocksalt ordering is the most commonly seen order in double perovskites, as it is stabilised by electrostatic and steric considerations, arising from a difference in size and charge of the different B-site ions [31]. *A*-site rocksalt ordering is much less common, however. This discrepancy can be explained by examining the environment of the anion in rocksalt-ordered $AA'B_2O_6$ and $A_2BB'O_6$ double perovskites (Figure 5.1). In each case, the anion is surrounded by four *A* sites and two *B* sites. Where *B*-site rocksalt ordering occurs (Figure 5.1b), the anion can move closer to the smaller *B*-site ion; however, in the case of *A*-site rocksalt order (Figure 5.1a), the anion is unable to move closer to one *A*4 ion without moving farther from the other [31]. This case is seen rarely, for example in $NaBaLiNiF_6$ [90], where a difference in charge between the two A-site atoms stabilises this ordering.

Columnar ordering

Columnar ordering, with similar ions arranging themselves in alternating columns, can also be considered "1D" or (110) ordering, as it is along this plane which similar ions will lie, in a one-dimensional chain. This is rare in both *A*- and *B*-site-ordered double perovskites, as it gives rise to multiple oxygen sites, as shown in Figure 5.3. In the case of *A*-site ordered double perovskites, such as $CaFeTi_2O_6$ [91], the two oxygen sites are *cis*- and *trans*-co-ordinated by the different *A* ions. Where the *A* and *A*′ ions are of different sizes,

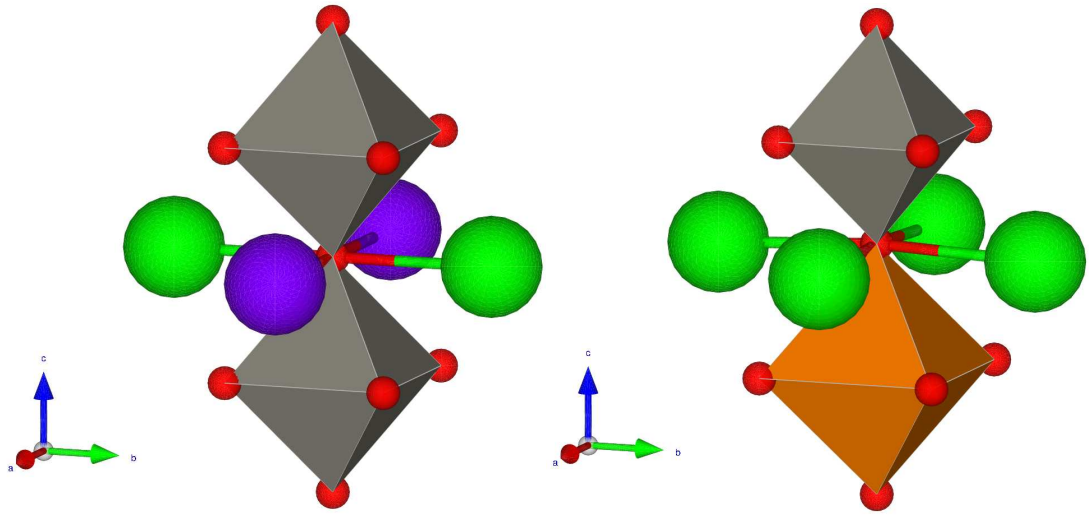

Figure 5.1 Rocksalt ordering of A-site and B-site cations. Relevant bonds are shown. a) Rocksalt ordering of A-site atoms (green and purple) does not allow oxygen atoms (red) to optimise bond lengths. b)Rocksalt ordering of B-site atoms (grey and orange octahedra) allows shifting of oxygen atoms towards the smaller ion

this allows optimisation of bond length through BO_6 octahedral tilting: an $a^+a^+c^+$-tilting. Where B-site ions are columnar, such as in the charge-ordered $NdSrMn^{3+}Mn^{4+}O_6$ [92, 93], three different oxygen positions are found: B-O-B, B'-O-B', and B-O-B': this is unfavourable, as the B-O-B or B'-O-B' oxygen sites must be under- or over-bonded. Charge ordering and first-order Jahn-Teller distortions are required to stabilise the arrangement.

Layered ordering

Layered ordering can be considered "2D" by the definition given by King and Woodward, or (100), as the ions align in a sheet. This is the least common form of ordering in B-site ions, as it is least favourable from an electrostatic point of view, as each B-site cation will have four similar nearest neighbours, and only two different. This arrangement is also least favourable from a bonding point of view: where one-third of oxygen ions in columnar perovskites are over- or under-bonded, here, two-thirds will have unfavourable valence bond sums. This ordering requires octahedral tilting in conjunction with Jahn-Teller-active cations. La_2CuSnO_6 is an example of a B-site-ordered double perovskite with layered ordering [94]. In contrast, layered ordering is the most common where A-site ordering is seen, particularly where there is a rocksalt arrangement of B-site

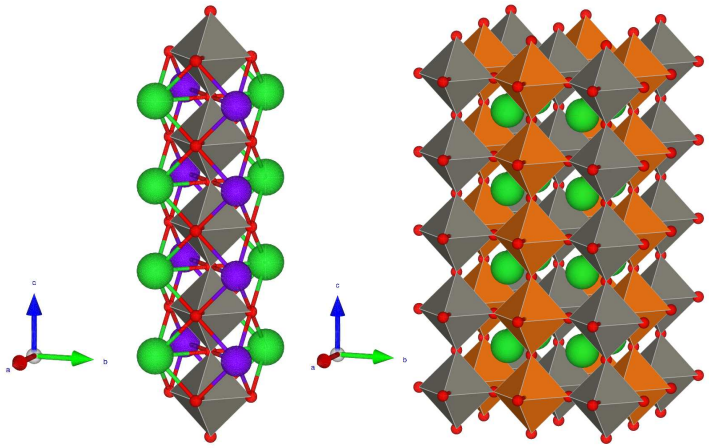

(a) (b)

Figure 5.2 Columnar ordering of A-site and B-site cations, showing three different oxygen environments: B-O-B, B'-O-B' and B-O-B'. a) Columnar ordering of A-site atoms (green and purple). Oxygen ions are *cis*-bonded to A-site ions in the ac and bc planes and *trans*-bonded in the ab plane. They can shift (via $a^+a^+c^-$ BO_6 octahedral tilting [91]) to optimise A-O and A'-O bond lengths. b) Columnar ordering of B-site atoms (grey and orange octahedra).

ions, and second-order Jahn Teller distortions arising on one of the B-site ions. This difference in frequency of occurrence arises from anion or A-site vacancies, in conjunction with a size difference between A and A' ions. Second-order Jahn-Teller effects on rocksalt-ordered B-site cations can also stabilise this arrangement of A-site ions, as is seen in the doubly-ordered $NaLaMgWO_6$ [95] (Figure 5.4). This compound is related to the $SrLaMgWO_6$ studied in this chapter; however, the ordered material has a larger charge difference between the A-site ions, and no magnetic ion (tungsten in $NaLaMgWO_6$ is in the 6+ oxidation state).

5.2 Synthesis of $LaSrMgWO_6$

$LaSrMgWO_6$ was synthesised using standard solid state techniques from La_2O_3, $SrCO_3$, MgO and WO_3. Stoichiometric quantities of each reagent were ground together and pressed into a pellet, before being calcined at 900 °C for 2 h. The pellet was then re-ground and pressed, then sintered at 1200 °C for 12 h under flowing 10 % H_2/N_2 gas. The quality of the sample was examined by X-ray diffraction, and the sintering step repeated until no further improvement was seen.

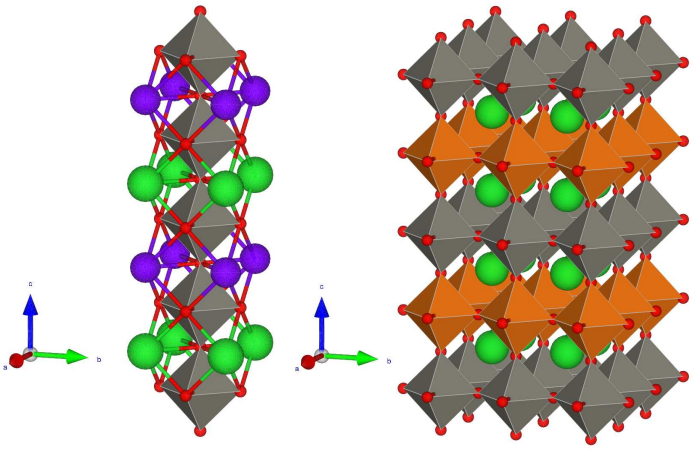

Figure 5.3 Layered ordering of a) *A*-site (green and purple) and b) *B*-site (grey and orange) cations. Relevant bonds are shown.

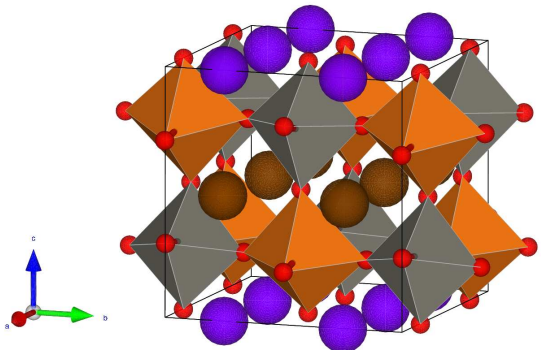

Figure 5.4 Structure of $NaLaMgWO_6$, showing layered-ordered sodium and lanthanum (brown, purple) atoms on the *A*-site, and rocksalt-ordered magnesium and tungsten (orange, grey) atoms on the B site.

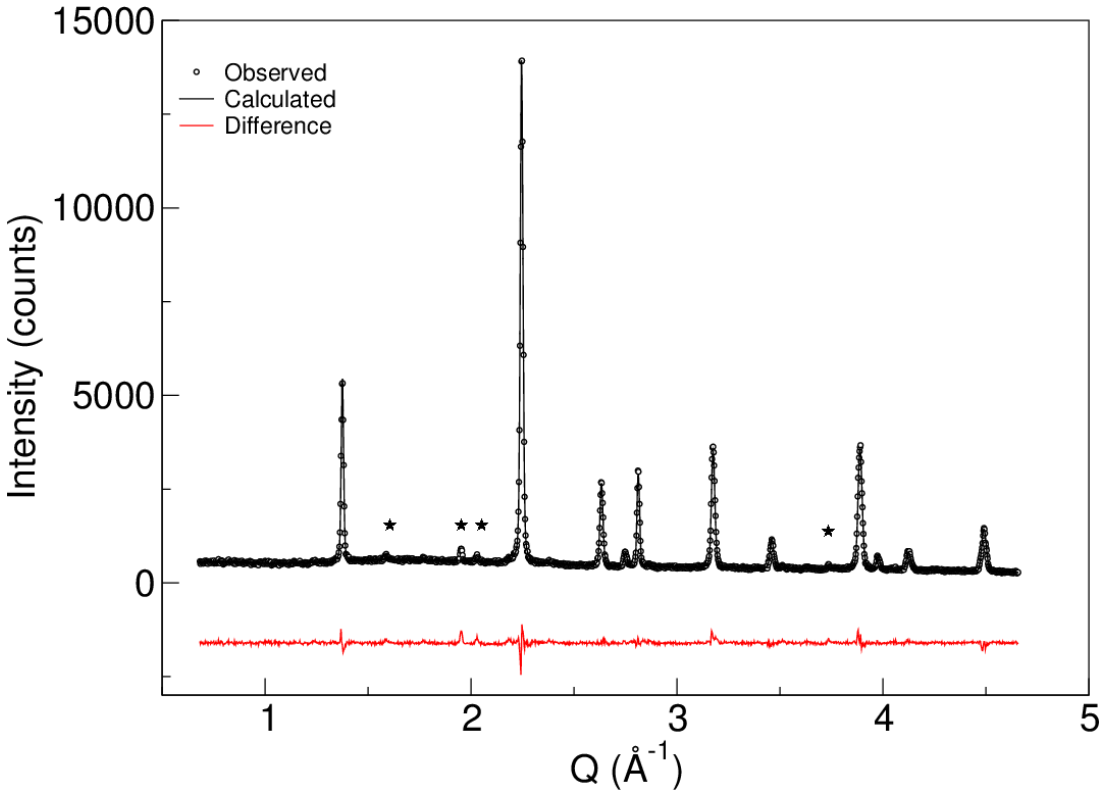

Figure 5.5 X-ray diffraction pattern of $LaSrMgWO_6$, with $Fm\bar{3}m$ fit. Incident X-rays are Cu-K_α, $\lambda = 1.54\,Å$. Impurities are shown by ★.

5.3 Structural characterisation

5.3.1 X-Ray diffraction

Initial X-ray diffraction patterns of the sample show the presence of a tungsten impurity: attempts to synthesise the compound in a less reducing atmosphere (5 % H_2/N_2) were unsuccessful. Figure 5.5 shows the refinement to $Fm\bar{3}m$ unit cell for the X-ray data, with Table 5.1 showing the quality of this cubic fit.

5.3.2 Neutron diffraction

Initial examination of the room temperature neutron diffraction pattern of $LaSrMgWO_6$ indicated a very poor sample, with broad peaks, a large background, and poor fit to the $Fm\bar{3}m$ unit cell refined from the X-ray data. A fit to the monoclinic $P2_1/c$ space group yields a significantly better fit (Figure 5.6), particularly at high Q.

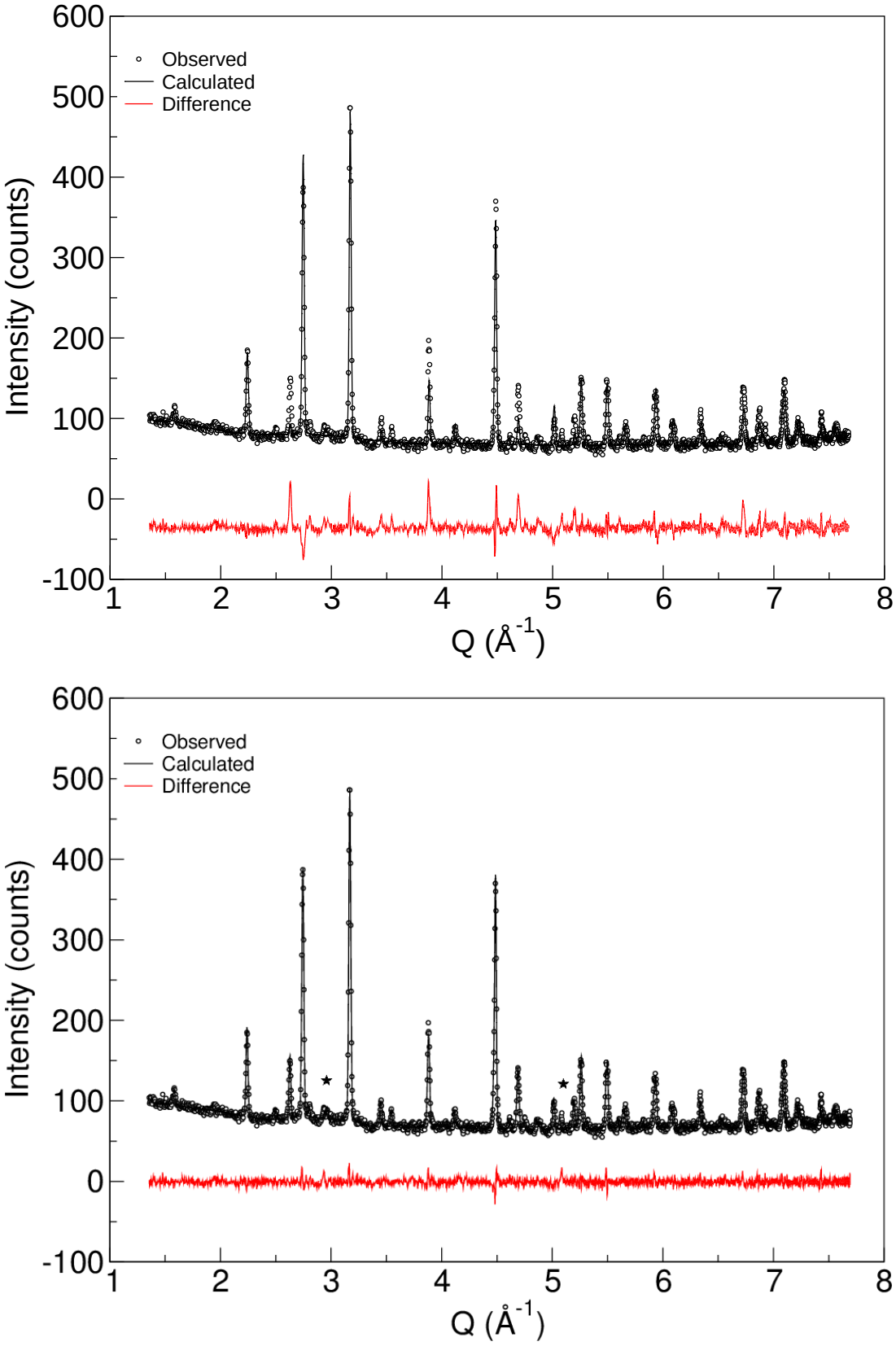

Figure 5.6 Comparison of cubic $Fm\bar{3}m$ (top, $\chi^2 = 3.898$) and monoclinic $P2_1/c$ (bottom, $\chi^2 = 1.310$) fits to neutron diffraction data of $LaSrMgWO_6$ at 300 K. Impurities are shown by ★.

Table 5.1 Comparison of refinement to $Fm\bar{3}m$ structure with previous results from Yoshimura*et al.* [89]

	This Study	Previous work [89]
a (Å)	7.9212(2)	7.922
V (Å^3)	497.02(4)	497.1
La, Sr (0.25, 0.25, 0.25)		
B (Å^2)	0.6(2)	Not reported
Mg (0.5, 0, 0)		
B (Å^2)	1.0(7)	Not reported
W (0, 0, 0)		
B (Å^2)	0.5(1)	Not reported
O1 (x, 0, 0)		
x	0.748(1)	Not reported
B (Å^2)	2.7(3)	Not reported
W impurity (mol%)	15.4	Not reported
R_p (%)	4.58	Not reported
R_{wp} (%)	6.04	Not reported
R_{exp} (%)	4.00	Not reported
χ^2	2.326	Not reported

The results from the monoclinic fit, along with those to data taken at 3.5 K, are detailed in Table 5.2, and the structure of the unit cell in Figure 5.7.

5.4 Discussion

Neutron diffraction results on $LaSrMgWO_6$ show that the compound is monoclinic at room temperature and 3.5 K. This is an improvement on the "pseudo-cubic" structure described by Yoshimura *et al.* [89]. Attempted refinement of magnesium occupancy yields no improvement in χ^2; indeed, setting the occupancy of magnesium to a lower value resulted in refinement back up to 100 % occupancy.

Inclusion of anisotropic atomic displacement parameters improves the fit of the model ($\chi^2 = 1.094$ versus $\chi^2 = 1.354$); however, examination of these factors show that they do not make physical sense, as root mean square displacement of the atoms is negative.

The tungsten impurity present in the sample is on the order of 12 %: this value is in agreement across both neutron diffraction measurements, and the initial

Table 5.2 Refinement results of $LaSrMgWO_6$ to a $P2_1/c$ unit cell at different temperatures. Neutron wavelength is 1.59 Å

T (K)	3.5	300
a (Å)	7.9001(3)	7.9121(4)
b (Å)	5.5891(2)	5.5985(3)
c (Å)	9.6877(10)	9.7002(13)
β (°)	144.609(2)	144.593(3)
V (Å^3)	247.738	248.948
La, Sr (x, y, z)		
x	0.2482(24)	0.251(3)
y	0.0174(9)	0.009(2)
z	0.9996(11)	0.991(1)
B (Å^2)	0.59(6)	0.94(5)
Sr on A site (%)	76(6)	73(6)
Mg (0, 0, 0)		
B (Å^2)	1.98(3)	1.0(1)
W (0, 0.5, 0)		
B (Å^2)	1.1(1)	1.9(3)
O1 (x, y, z)		
x	0.315(3)	0.312(3)
y	0.496(1)	0.497(2)
z	0.063(1)	0.064(1)
B (Å^2)	0.7(1)	0.9(1)
O2 (x, y, z)		
x	0.762(2)	0.756(3)
y	0.264(2)	0.265(2)
z	0.736(2)	0.737(2)
B (Å^2)	1.1(2)	0.9(2)
O3 (x, y, z)		
x	0.178(2)	0.187(2)
y	0.283(2)	0.280(2)
z	0.712(2)	0.722(2)
B (Å^2)	0.6(2)	0.8(2)
W impurity (mol%)	11.3	12.7
R_p (%)	3.21	3.50
R_{wp} (%)	4.35	4.44
R_{exp} (%)	1.82	3.91
χ^2	5.827	1.310

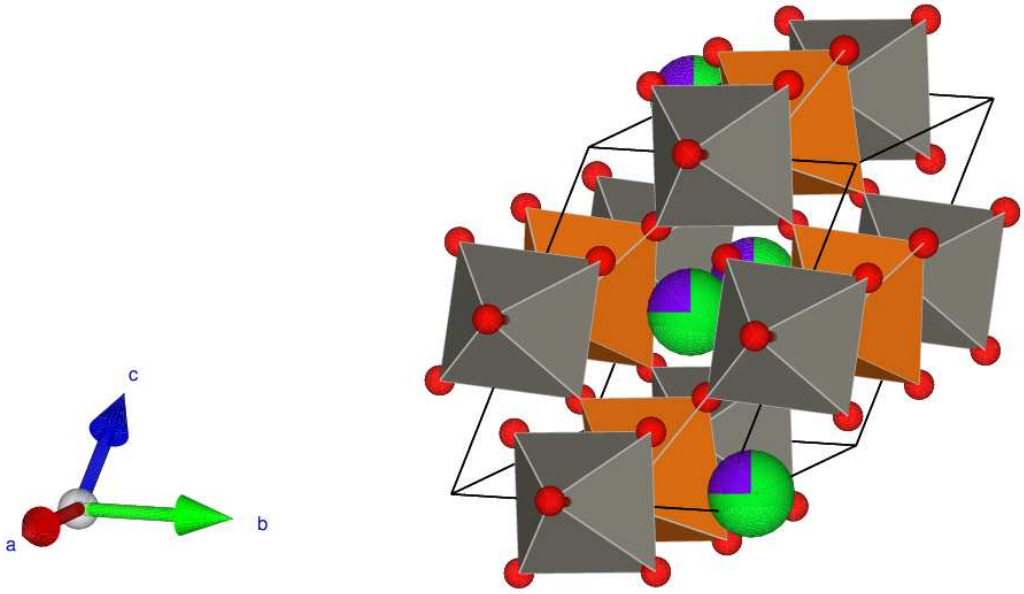

Figure 5.7 Refined structure of $LaSrMgWO_6$ at 3.5 K. Green/purple circles are Sr/La; orange and grey octahedra are MgO_6 and WO_6, respectively.

characterisation carried out by X-ray diffraction.

No ordering of strontium and lanthanum is observed on the A site: this is as expected, as a larger charge difference would be required for the layered ordering seen in the related compound $LaNaMgWO_6$. Refinement of A-site occupancy shows a slight improvement in fit ($\chi^2 = 1.341$ versus $\chi^2 = 1.310$ at 300 K) if the site is 74.3 % strontium occupied, rather than a 50:50 ratio of strontium to lanthanum. A similar improvement is seen in the 3.5 K data, with similar occupancies. It is therefore probable that, rather than a 1:1 La:Sr ratio, this compound has a 1:3 ratio of the two elements.

This imbalance in A-site atoms implies that, despite the fully occupied magnesium site, the tungsten ions in this compound are not in the 5+ oxidation state. Rather, the charge balance suggests an overall 5.5+ oxidation state, equating to a 1:1 ratio of W^{5+}:W^{6+}.

Although the $LaSrMgWO_6$ peaks are sharp and symmetrical, some amorphous background is visible, particularly at low Q – it is likely that this arises from unincorporated lanthanum in the sample. Further sintering might improve this; however, it is more likely that these impurities, along with the tungsten impurity, will require a different method of synthesis altogether, possibly in a quartz tube, as was attempted for Ba_2YWO_6. This would allow closer control of the oxidation

state of the tungsten throughout the reaction, and integration of all reagents: from the current synthesis, it can be seen that some lanthanum is not included in the final compound, leading to an imbalance on the A site and mixed tungsten oxidation states.

5.5 Conclusions

The compound $La_{0.5}Sr_{1.5}MgWO_6$, with fully occupied Mg site, has been synthesised. The structure has been refined as being in the monoclinic $P2_1/c$ space group, rather than "pseudo-cubic" as described by Yoshimura *et al.* [89].

The overall tungsten oxidation state is 5.5+: this represents only a small improvement over the 5.67+ oxidation state seen in $Ba_2Y_{0.78}WO_6$. Further work will be necessary in order to improve the quality of sample; however, the full oxidation of the magnesium site in this compound is a promising sign. If the 1:1 $LaSrMgWO_6$ can be synthesised and purified, magnetic and physical property measurements should be carried out: these will allow investigation of the effect of magnetic frustration on a strongly spin-orbit-coupled compound.

Chapter 6

Conclusions and Outlook

This thesis has detailed the synthesis and study of a variety of double perovskites, with magnetic ions of $3d^9$ and $5d^1$ electron configurations. The structural and magnetic properties of these materials have been investigated, and conclusions drawn from the data. A summary of the findings is given here, along with a brief examination of potential future work in the area.

Chapter 3 detailed the properties of the Jahn-Teller-distorted tetragonal double perovskite Sr_2CuWO_6, with the magnetic Cu^{2+} ($3d^9$) ion. It was hoped that the large degree of separation between copper ions in the z axis would give rise to solely in-plane interactions between magnetic moments, leading to quantum spin liquid behaviour at base temperature. However, high-resolution neutron diffraction studies indicated the existence of long-range magnetic order in the compound: a peak at $0.68\,\text{Å}^{-1}$ indexed to a k-vector of $\left(\frac{1}{2}, 0, \frac{1}{2}\right)$, suggesting type-2 antiferromagnetic order with moments aligned along the b axis, and an orthorhombic magnetic space group of $P_s\bar{1}$. Muon spin resonance and inelastic neutron diffraction studies on Sr_2CuWO_6 indicated that electron spins were strongly correlated in two dimensions, but remained dynamic down to a T_N of 24 K, below which magnetic moments are predicted to be static. This strong correlation of spins persists up to 100 K, above which paramagnetic behaviour was observed. This regime between T_N and 100 K can be described as a "thermal spin liquid": that is, a phase above the ground state of the compound in which spins are dynamic, but strongly correlated to one another, with the correlation length gradually decreasing with increasing temperature until paramagnetism is observed.

Future work on this compound could involve the synthesis of Dion-Jacobson phases of $Sr_nCu_{\frac{n}{2}}W_{\frac{n}{2}}O_{3n+1}$. These compounds have layers of A-site atoms between the BO_6 octahedra, leading to greater separation of the layers: this may reduce or eliminate inter-layer coupling of Cu^{2+} ions, leading to purely 2D interactions in the *ab* plane. [96, 97]

The examination of the series $Ba_2Y_xWO_6$ undertaken in Chapter 4 explores the effect of vacancies on the B site of the $A_2BB'O_6$ double perovskite structure. At the low-occupancy limit, $Ba_2Y_{\frac{2}{3}}WO_6$ has a kinetically favoured cubic structure, with longer sintering times leading to the formation of a vacancy-ordered rhombohedral structure. Addition of lithium into the synthesis mixture allowed incorporation of Li^+ ions, and stabilisation of the cubic structure; the precise degree of lithiation could not be determined from X-ray diffraction studies, however.

It was found that variation of the sintering atmosphere allowed for incorporation of increased amounts of yttrium into the double perovskite structure, with a sintering atmosphere of 7.5 % H_2/N_2 leading to the maximum observed occupancy of $Ba_2Y_{0.78}WO_6$. Despite experimentation with multiple synthesis methods, no improvement on this level of occupancy was achieved. An entropic consideration of the mixing of W(V) with W(VI) on the B' site, and of yttrium ions with vacancies on the B site, was undertaken, and the maximum entropically favourable occupancy was found to be 0.8. It was therefore proposed that the fully occupied compound could not be synthesised by the standard double perovskite synthesis method; rather, high pressure syntheses may be required.

Neutron diffraction studies on the intermediate compound $Ba_2Y_{0.75}WO_6$ showed a small shift from cubic ($Fm\bar{3}m$) to tetragonal (I4/mmm) structure at 115 K. Heat capacity measurements on this compound suggest that at low temperature, 16 % of W^{5+} spins are unpaired. Magnetic susceptibility measurements on $Ba_2Y_{0.75}WO_6$ suggest the presence of multiple contributing components to the overall magnetic susceptibility.

This series of compounds could be better understood by undertaking dielectric measurements of the materials. This may allow a study of the conductivity properties, along with an indication of the grain size within the composites. In addition, the mobility of Li ions within $Ba_2Li_xY_{\frac{2}{3}}WO_6$ could be explored, as it is possible that this may be an ionic conductor.

Finally, Chapter 5 detailed the synthesis and study of $La_{0.5}Sr_{1.5}MgWO_6$, a

compound with $W^{5.5+}$ ions and full occupancy of the Mg site. The space group of this compound was refined through neutron diffraction as monoclinic $P2_1/c$, an improvement on the "pseudo-cubic" structure previously reported. Extended attempts were not made to synthesise the 1:1 compound $LaSrMgWO_6$ during the course of this thesis: such a synthesis would allow study of a truly frustrated W^{5+} material, which was not achieved with the $Ba_2Y_xWO_6$ compounds reported here.

Appendix A

Python code used in fitting data

A.1 Fitting of μSR spectroscopy data

```
from datatls3 import *
from graceinterface2 import *
from grace_np import *
from numpy import *
from scipy import *
from lmfit import minimize, Parameters, Parameter, report_fit


#Takes three-column Time, Asymmetry, Error, returns polarized data.
def polarize(data):
    Time=data[0]
    Asymmetry=data[1]
    Error=data[2]
    Pz=[]
    PzErr=[]
    Abg=0
    Ainit=28.632
    for p in range(1026):
        Pz.append((Asymmetry[p]-Abg)/(Ainit-Abg))
        PzErr.append((Error[p]/Asymmetry[p])*Pz[p])
    return array([Time, Pz, PzErr])

#Sums errors with appropriate weighting
def sum_errors(list_of_errors):
    if len(list_of_errors) > 0:
        return sqrt(sum(list_of_errors*list_of_errors))/len(list_of_errors)
    else:
        return 0


#Rebins from three-column (Time, Pz, Err)
def rebin(data,firstbin):
    t=data[0]
```

```
    p=data[1]
    e=data[2]
    pb=[]
    eb=[]
    tb=[]
    binsize=int(firstbin)
    index = int(firstbin)
    pb.append(average(p[0:binsize],axis=0,weights=1/e[0:binsize]))
    eb.append(sum_errors(e[0:binsize]))
    tb.append(mean(t[0:binsize]))
    while index+binsize < len(p) and binsize< 100*firstbin:
        while sum_errors(e[index:index+binsize]) > 2*eb[0] and binsize< 20*
            firstbin:
            binsize+=1
        pb.append(average(p[index:index+binsize],axis=0,weights=1/e[index:index+
            binsize]))
        if binsize > 5:
            eb.append(1*sqrt(std(e[index:index+binsize])/binsize))
        else:
            eb.append(sum_errors(e[index:index+binsize]))
        tb.append(mean(t[index:index+binsize]))
        index+=binsize
    pb=array(pb)
    eb=array(eb)
    tb=array(tb)
    return array([tb,pb,eb])


#Fits data to a compressed exponential function.  See below for parameters
def StretchedExpFitFunction(params,x,data):
    T=x
    K1=params['K1'].value
    K2=1-params['K1'].value
    sig=params['sig'].value
    lam=params['lam'].value
    bet=params['bet'].value
    gam=85.16*10**3
    Fit=[]
    for time in T:
        Fit.append(K1*exp(-(lam*time))+K2*exp(-((sig*time)**bet)))
    resids = Fit - data
    weighted = sqrt(resids**2/PzErr**2)
    return weighted

#Plots compressed exponential
def StretchedExpToPlot(params,x):
    T=x
    K1=params['K1'].value
    K2=1-params['K1'].value
    sig=params['sig'].value
    lam=params['lam'].value
    bet=params['bet'].value
    Plotting=[]
    for time in T:
        Plotting.append(K1*exp(-(lam*time))+K2*exp(-((sig*time)**bet)))
    return Plotting
```

```
#Initialises plot for final data and fits
g = grace("Time (microseconds)","Pz",leg=[1.2,0.9])

K1s = []
K1errs = []
K2s = []
K2errs = []
sigs = []
sigerrs = []
lams = []
lamerrs = []
Temps = []
bets = []
beterrs = []
blines = []
blerrs = []

#Datasets used.  Run number:Run temperature.  Split into high- and low-
    temperature data sets, reflecting different relaxation models
DatasetsHT = {45480:99.2,45481:149,45482:199}
DatasetsLT =
    {45473:1.92,45474:19.7,45475:22.7,45476:23.7,45477:24.7,45478:34.7,45479:49.8}



for runnr in DatasetsLT.keys():
    cw=getdata(str(runnr)+".txt")
    cw=polarize(cw)
    cw=rebin(cw,3)
    t=cw[0]
    Pz=cw[1]
    PzErr=cw[2]
    ToPlot=[]
    GLParams=Parameters()
    GLParams.add('K1',vary=True,value=0.7,min=0,max=1)
    GLParams.add('bet',vary=True,value=1.5,min=0,max=2)
    GLParams.add('sig',vary=True,value=0.05,min=0)
    GLParams.add('lam',vary=True,value=5,min=0.5)
    fit=minimize(StretchedExpFitFunction,GLParams, args=(t,Pz))

    ToPlot=StretchedExpToPlot(fit.params,t)

    g.add([t,Pz,PzErr],str(DatasetsLT[runnr])+ " K",sz=0.5,l=0)
    g.add([t,ToPlot],str(DatasetsLT[runnr])+" K fit",sz=0)


    print("\n\n\nTemperature = "+str(DatasetsLT[runnr]))
    report_fit(fit.params)

    K1s.append(GLParams['K1'].value)
    K1errs.append(GLParams['K1'].stderr)
    K2s.append(1-GLParams['K1'].value)
    K2errs.append(GLParams['K1'].stderr)
    bets.append(GLParams['bet'].value)
    beterrs.append(GLParams['bet'].stderr)
    sigs.append(GLParams['sig'].value)
    sigerrs.append(GLParams['sig'].stderr)
```

```
    lams.append(GLParams['lam'].value)
    lamerrs.append(GLParams['lam'].stderr)
    Temps.append(DatasetsLT[runnr])

#High-temperature data has no input from lambda: this is therefore fixed at a low value (K2 fits to zero independently)
for runnr in DatasetsHT.keys():
    cw=getdata(str(runnr)+".txt")
    cw=polarize(cw)
    cw=rebin(cw,3)
    t=cw[0]
    Pz=cw[1]
    PzErr=cw[2]
    ToPlot=[]
    #K1 and lambda are lorentzian. K2 (defined as 1-K1), beta and sigma are stretched exponential (exp(-((sigma*time)**beta))).
    GLParams=Parameters()
    GLParams.add('K1',vary=True,value=0.3,min=0,max=0.7)
    GLParams.add('bet',vary=True,value=1.5,min=0,max=2)
    GLParams.add('sig',vary=True,value=0.05,min=0)
    GLParams.add('lam',vary=False,value=0,min=0.5,max=10)
    fit=minimize(StretchedExpFitFunction,GLParams, args=(t,Pz))

    ToPlot=StretchedExpToPlot(fit.params,t)

    g.add([t,Pz,PzErr],str(DatasetsHT[runnr])+ " K",sz=0.5,l=0)
    g.add([t,ToPlot],str(DatasetsHT[runnr])+" K fit",sz=0)


    print("\n\n\nTemperature = "+str(DatasetsHT[runnr]))
    report_fit(fit.params)

    K1s.append(GLParams['K1'].value)
    K1errs.append(GLParams['K1'].stderr)
    K2s.append(1-GLParams['K1'].value)
    K2errs.append(GLParams['K1'].stderr)
    bets.append(GLParams['bet'].value)
    beterrs.append(GLParams['bet'].stderr)
    sigs.append(GLParams['sig'].value)
    sigerrs.append(GLParams['sig'].stderr)
    lams.append(GLParams['lam'].value)
    lamerrs.append(GLParams['lam'].stderr)
    Temps.append(DatasetsHT[runnr])

g.scale(x=[0,16],y=[0,1],dy=0.2,dx=4)
g.save("Afits")

#Plot of lorentzian vs Comp. Exp.
h=grace("Temperature (K)","K1",leg="topright")
h.add([Temps,K1s,K1errs],"K1 (lorentzian)",l=0)
h.add([Temps,K2s,K2errs],"K2 (compressed exponential)",l=0)
h.save("BK1")


#Str. Exp. sigma
j=grace("Temperature (K)","sigma")
j.add([Temps,sigs,sigerrs],"Heating",l=0)
```

```
j.save("Csigma")


#Lorentzian lambda
k=grace("Temperature␣(K)","lambda")
k.add([Temps,lams,lamerrs],"Heating",l=0)
k.save("Dlambda")


#Comp. Exp. exponent beta
m=grace("Temperature␣(K)","beta")
m.add([Temps,bets,beterrs],"Heating",l=0)
m.save("Ebeta")

#Baseline data
#l=grace("Temperature (K)","baseline")
#l.add([Temps,blines,blerrs])
```

Appendix B

Data Collected

B.1 Sr_2CuWO_6

B.1.1 Neutron diffraction data

Table B.1 Details of measurements taken on D2B at ILL on a sample of Sr_2CuWO_6.

Run number	Temperature (K)	Wavelength (Å
505823 – 505828	3.5	1.59
505829 – 505848	3.5	2.398
505849 – 505868	50	2.398
505820 – 505822	298	1.59

B.1.2 Inelastic neutron scattering data

Table B.2 Details of measurements taken on MARI at ISIS on a sample of Sr_2CuWO_6.

Run number	Temperature (K)	μA.h recorded
18349	Cooling	231
18350	5	2194

Run number	Temperature (K)	μA.h recorded
18351	10	3647
18352	20	3000
18353	50	3000
18354	100	3000
18355	200	3000
18356	35	3000
18357	75	3000

B.1.3 Muon spin relaxation data

Table B.3 Details of measurements taken on MuSR at ISIS on a sample of Sr_2CuWO_6.

Run number	Temperature (K)	Field (G)	Muon counts (Million events)
45462	Cooling	20	4
45463	2	100	19.2
45464	2	100	48
45465	2	0	19.3
45466	2	50	19.2
45467	2	200	19.3
45468	2	500	19.3
45469	2	1000	19.2
45470	2	1500	19.3
45471	20	0	19.2
45472	23	0	1.01
45473	2	0	38.5
45474	20	0	38.4
45475	23	0	38.4
45476	24	0	38.4
45477	25	0	38.4
45478	35	0	38.4
45479	50	0	38.4
45480	100	0	38.4
45481	150	0	38.4

Run number	Temperature (K)	Field (G)	Muon counts (Million events)
45482	200	0	38.5
45483	200	100	38.3
45484	200	100	38.4
45485	200	0	38.5
45486	42	0	38.4
45487	30	100	4.86
45488	25	100	4.88
45489	25	100	14.6
45490	23	100	28.8
45491	23	500	19.2
45492	23	1000	19.3
45493	23	1500	19.3
45494	23	2000	19.2
45495	22	100	28.9
45496	21	100	28.9
45497	20	100	28.8
45498	11	100	28.9
45499	24	100	≈ 0

B.2 $Ba_2Y_xWO_6$

B.2.1 Neutron diffraction data

$Ba_2Y_{\frac{2}{3}}WO_6$

$Ba_2Y_{0.75}WO_6$

Table B.4 Details of measurements taken at HRPD on a 4.7 g sample of $Ba_2Y_{0.75}WO_6$.

Run number	Temperature (K)	Measuring time (μA.h)	Notes
58337	300	1	Initial pattern

Run number	Temperature (K)	Measuring time (μA.h)	Notes
58338	N/A	46	Cooling: 300 K to 190 K
58339	N/A	56	Cooling: 196 K to 46 K
58340	N/A	14	Cooling: 46 K to 9 K
58341	9	160	Long scans, to give good
58342	100	160	statistics on data.
58343	200	160	
58344	300	160	
58347	10	8	Short scans, to determine
58348	20	8	position of transition.
58349	30	8	
58350	40	8	
58351	50	8	
58352	60	8	
58353	70	8	
58354	80	8	
58355	90	8	
58356	100	8	
58357	110	8	
58358	120	8	
58359	130	8	
58360	140	8	
58361	150	8	
58362	160	8	
58363	170	8	
58364	180	8	
58365	190	8	
58366	200	8	
58367	210	8	
58368	220	8	
58369	230	8	
58370	240	8	
58371	250	8	
58372	260	8	
58373	270	8	
58374	280	8	

Run number	Temperature (K)	Measuring time (μA.h)	Notes
58375	290	8	
58376	300	8	
58377	295	8	
58378	285	8	
58379	275	8	
58380	265	8	
58381	255	8	
58382	245	8	
58383	235	8	
58384	225	8	
58385	215	8	
58386	205	8	
58387	195	8	
58388	185	8	
58389	175	8	
58390	165	8	
58391	155	16	
58392	145	16	
58393	135	16	
58394	125	16	
58395	115	16	
58396	105	16	
58397	95	16	
58398	85	16	
58399	75	16	
58400	65	16	
58401	55	16	
58402	45	16	
58403	35	16	
58404	25	16	
58405	15	8	
58406	50	160	

B.2.2 Magnetic susceptibility measurements

Table B.5 Details of magnetic susceptibility measurements taken on a Quantum Design MPMS (SQUID) on $Ba_2Y_xWO_6$.

Sample	Scan type	Temperature (K)	Field (oersted)
$Ba_2Y_{\frac{2}{3}}WO_6$	M(H)		
$Ba_2Y_{\frac{2}{3}}WO_6$	M(T)		
$Ba_2Y_{0.75}WO_6$	M(H)		
$Ba_2Y_{0.75}WO_6$	M(T)		
$Ba_2Y_{0.78}WO_6$	M(H)		
$Ba_2Y_{0.78}WO_6$	M(T)		
Ba_2NdWO_6			
Ba_2NdWO_6			

Bibliography

[1] P. W. Anderson, "More Is Different," *Science*, vol. 177, pp. 393–396, Aug. 1972.

[2] S. Blundell, *Magnetism in condensed matter*. No. 4 in Oxford master series in condensed matter physics, Oxford: Oxford Univ. Press, reprint ed., 2014. OCLC: 898266646.

[3] P. Atkins and J. de Paula, *Atkins' Physical Chemistry*. OUP Oxford, 8 ed., Mar. 2006.

[4] A. M. Cook, S. Matern, C. Hickey, A. A. Aczel, and A. Paramekanti, "Spin-orbit coupled j_{eff}=1/2 iridium moments on the geometrically frustrated fcc lattice," *Physical Review B*, vol. 92, pp. 020417–020422, July 2015.

[5] J. B. Goodenough, "Theory of the Role of Covalence in the Perovskite-Type Manganites [La, M(II)]MnO_3," *Physical Review*, vol. 100, pp. 564–573, Oct. 1955.

[6] J. B. Goodenough, "An interpretation of the magnetic properties of the perovskite-type mixed crystals $La_{1-x}Sr_xCoO_{3-\lambda}$," *Journal of Physics and Chemistry of Solids*, vol. 6, pp. 287–297, Aug. 1958.

[7] J. Kanamori, "Superexchange interaction and symmetry properties of electron orbitals," *Journal of Physics and Chemistry of Solids*, vol. 10, pp. 87–98, July 1959.

[8] W. Pauli, "Exclusion Principle and Quantum Mechanics," *Nobel Lectures, Physics*, vol. 1942-1962, 1964.

[9] A. P. Ramirez, "Strongly Geometrically Frustrated Magnets," *Annual Review of Materials Science*, vol. 24, no. 1, pp. 453–480, 1994.

[10] A. Harrison, "First catch your hare: the design and synthesis of frustrated magnets," *Journal of Physics: Condensed Matter*, vol. 16, pp. S553–S572, Mar. 2004.

[11] P. Anderson, "Resonating valence bonds: A new kind of insulator?," *Materials Research Bulletin*, vol. 8, pp. 153–160, Feb. 1973.

[12] A. Kekulé, "Sur la constitution des substances aromatiques," *Bulletin de la Societe Chimique de Paris*, vol. 3, no. 2, pp. 98–110, 1865.

[13] A. Kekulé, "Untersuchungen über aromatische Verbindungen Ueber die Constitution der aromatischen Verbindungen. I. Ueber die Constitution der aromatischen Verbindungen.," *Annalen der Chemie und Pharmacie*, vol. 137, no. 2, pp. 129–196, 1866.

[14] M. A. de Vries, J. R. Stewart, P. P. Deen, J. O. Piatek, G. J. Nilsen, H. M. Rønnow, and A. Harrison, "Scale-Free Antiferromagnetic Fluctuations in the s=1/2 Kagome Antiferromagnet Herbertsmithite," *Physical Review Letters*, vol. 103, pp. 237201–237204, Dec. 2009.

[15] T.-H. Han, J. S. Helton, S. Chu, D. G. Nocera, J. A. Rodriguez-Rivera, C. Broholm, and Y. S. Lee, "Fractionalized excitations in the spin-liquid state of a kagome-lattice antiferromagnet," *Nature*, vol. 492, pp. 406–410, Dec. 2012.

[16] Y. Shimizu, K. Miyagawa, K. Kanoda, M. Maesato, and G. Saito, "Spin Liquid State in an Organic Mott Insulator with a Triangular Lattice," *Physical Review Letters*, vol. 91, pp. 107001–107004, Sept. 2003.

[17] A. N. Vasiliev, O. S. Volkova, E. A. Zvereva, A. V. Koshelev, V. S. Urusov, D. A. Chareev, V. I. Petkov, M. V. Sukhanov, B. Rahaman, and T. Saha-Dasgupta, "Valence-bond solid as the quantum ground state in honeycomb layered urusovite $CuAl(AsO_4)O$," *Physical Review B*, vol. 91, pp. 144406–144414, Apr. 2015.

[18] M. A. de Vries, A. C. Mclaughlin, and J.-W. G. Bos, "Valence Bond Glass on an fcc Lattice in the Double Perovskite Ba_2YMoO_6," *Physical Review Letters*, vol. 104, p. 177202, Apr. 2010.

[19] M. A. de Vries, J. O. Piatek, M. Misek, J. S. Lord, H. M. Rønnow, and J.-W. G. Bos, "Low-temperature spin dynamics of a valence bond glass in Ba_2YMoO_6," *New Journal of Physics*, vol. 15, p. 043024–043033, Apr. 2013.

[20] A. Mclaughlin, M. A. de Vries, and J.-W. Bos, "Persistence of the valence bond glass state in the double perovskites $Ba_{2-x}Sr_xYMoO_6$," *Physical Review B*, vol. 82, pp. 094424–094428 Sept. 2010.

[21] S. A. J. Kimber, I. I. Mazin, J. Shen, H. O. Jeschke, S. V. Streltsov, D. N. Argyriou, R. Valentí, and D. I. Khomskii, "Valence bond liquid phase in the honeycomb lattice material Li_2RuO_3," *Physical Review B*, vol. 89, p. 081408–081412, Feb. 2014.

[22] S. T. Bramwell and M. J. P. Gingras, "Spin Ice State in Frustrated Magnetic Pyrochlore Materials," *Science*, vol. 294, pp. 1495–1501, Nov. 2001.

[23] N. F. Mott, "The Basis of the Electron Theory of Metals, with Special Reference to the Transition Metals," *Proceedings of the Physical Society. Section A*, vol. 62, pp. 416–422, July 1949.

[24] J. Hubbard, "Electron Correlations in Narrow Energy Bands," *Proceedings of the Royal Society A: Mathematical, Physical and Engineering Sciences*, vol. 276, pp. 238–257, Nov. 1963.

[25] W. Witczak-Krempa, G. Chen, Y. B. Kim, and L. Balents, "Correlated Quantum Phenomena in the Strong Spin-Orbit Regime," *Annual Review of Condensed Matter Physics*, vol. 5, no. 1, pp. 57–82, 2014.

[26] G. Rose, "Beschreibung einiger neuen Mineralien des Urals," *Annalen der Physik und Chemie*, vol. 124, no. 12, pp. 551–573, 1839.

[27] K.-I. Kobayashi, T. Kimura, H. Sawada, K. Terakura, and Y. Tokura, "Room-temperature magnetoresistance in an oxide material with an ordered double-perovskite structure," *Nature*, vol. 395, pp. 677–680, Oct. 1998.

[28] B. J. Kennedy, C. J. Howard, K. S. Knight, Z. Zhang, and Q. Zhou, "Structures and phase transitions in the ordered double perovskites $Ba_2Bi^{III}Bi^{V}O_6$ and $Ba_2Bi^{III}Sb^{V}O_6$," *Acta crystallographica. Section B, Structural science*, vol. 62, pp. 537–546, Aug. 2006.

[29] F. Galasso, L. Katz, and R. Ward, "Substitution in the Octahedrally Coördinated Cation Positions in Compounds of the Perovskite Type1,2," *Journal of the American Chemical Society*, vol. 81, pp. 820–823, Mar. 1959.

[30] F. Galasso and J. Pyle, "Ordering in Compounds of the $A(B'_{0.33}Ta_{0.67})O_3$ Type," *Inorganic Chemistry*, vol. 2, pp. 482–484, June 1963.

[31] G. King and P. M. Woodward, "Cation ordering in perovskites," *Journal of Materials Chemistry*, vol. 20, pp. 5785–5796, July 2010.

[32] V. M. Goldschmidt, "Die Gesetze der Krystallochemie," *Naturwissenschaften*, vol. 14, pp. 477–485, May 1926.

[33] A. M. Glazer, "The classification of tilted octahedra in perovskites," *Acta Crystallographica Section B Structural Crystallography and Crystal Chemistry*, vol. 28, pp. 3384–3392, Nov. 1972.

[34] M. E. Straumanis, "The Sodium Tungsten Bronzes. I. Chemical Properties and Structure," *Journal of the American Chemical Society*, vol. 71, pp. 679–683, Feb. 1949.

[35] A. Sweedler, C. Raub, and B. Matthias, "Superconductivity of the alkali tungsten bronzes," *Physics Letters*, vol. 15, pp. 108–109, Mar. 1965.

[36] N. Haldolaarachchige, Q. Gibson, J. Krizan, and R. J. Cava, "Superconducting properties of the K_xWO_3 tetragonal tungsten bronze and the superconducting phase diagram of the tungsten bronze family," *Physical Review B*, vol. 89, pp. 104520-104525, vol. 14, pp. 113-115, Mar. 2014.

[37] K. Onnes, "Further Experiments with Liquid Helium," *Koninklijke Akademie von Wetenschappen te Amsterdam*, 1911.

[38] "Superconductivity: Present and Future Applications," *published by CCAS*.

[39] J. Bardeen, L. N. Cooper, and J. R. Schrieffer, "Theory of Superconductivity," *Physical Review*, vol. 108, pp. 1175–1204, Dec. 1957.

[40] P. Kapitza, "Viscosity of Liquid Helium below the λ-Point," *Nature*, vol. 141, pp. 74–74, Jan. 1938.

[41] J. F. Allen and A. D. Misener, "Flow Phenomena in Liquid Helium II," *Nature*, vol. 142, pp. 643–644, Oct. 1938.

[42] D. S. Sivia, *Elementary scattering theory: for X-ray and neutron users*. Oxford ; New York: Oxford University Press, 2011.

[43] H. M. Rietveld, "A profile refinement method for nuclear and magnetic structures," *Journal of Applied Crystallography*, vol. 2, pp. 65–71, June 1969.

[44] K. A. Olive and P. D. Group, "Review of Particle Physics," *Chinese Physics C*, vol. 38, no. 9, p. 090001, 2014.

[45] P. Bakule and E. Morenzoni, "Generation and applications of slow polarized muons," *Contemporary Physics*, vol. 45, pp. 203–225, May 2004.

[46] A. C. Larson and R. B. Von Dreele, "General Structure Analysis System (GSAS)," Tech. Rep. LAUR 86-748, Los Alamos National Laboratory, 1994.

[47] B. H. Toby, "EXPGUI, a graphical user interface for GSAS," *Journal of Applied Crystallography*, vol. 34, pp. 210–213, 2001.

[48] F. Perez and B. E. Granger, "IPython: A System for Interactive Scientific Computing," *Computing in Science & Engineering*, vol. 9, no. 3, pp. 21–29, 2007.

[49] P. Turner and E. Stambulchik, "Grace," 2007.

[50] G. Chen, R. Pereira, and L. Balents, "Exotic phases induced by strong spin-orbit coupling in ordered double perovskites," *Physical Review B*, vol. 82, p. 174440, Nov. 2010.

[51] G. Blasse, "New compounds with perovskite-like structures," *Journal of Inorganic and Nuclear Chemistry*, vol. 27, pp. 993–1003, May 1965.

[52] M. Gateshki, J. M. Igartua, and E. Hernández-Bocanegra, "X-ray powder diffraction results for the phase transitions in Sr_2MWO_6 (M = Ni, Zn, Co, Cu) double perovskite oxides," *Journal of Physics: Condensed Matter*, vol. 15, p. 6199, Sept. 2003.

[53] S. Vasala, J.-G. Cheng, H. Yamauchi, J. B. Goodenough, and M. Karppinen, "Synthesis and Characterization of $Sr_2Cu(W_{1-x}Mo_x)O_6$: A Quasi-Two-Dimensional Magnetic System," *Chemistry of Materials*, vol. 24, pp. 2764–2774, July 2012.

[54] Y. Todate, W. Higemoto, K. Nishiyama, and K. Hirota, "Magnetic ordering in ordered complex Cu perovskite probed by μSR and neutron diffraction," *Journal of Physics and Chemistry of Solids*, vol. 68, pp. 2107–2110, Nov. 2007.

[55] S. Vasala, H. Saadaoui, E. Morenzoni, O. Chmaissem, T.-S. Chan, J.-M. Chen, Y.-Y. Hsu, H. Yamauchi, and M. Karppinen, "Characterization of magnetic properties of Sr_2CuWO_6 and Sr_2CuMoO_6," *Physical Review B*, vol. 89, pp. 1134419–134427, Apr. 2014.

[56] N. D. Mermin and H. Wagner, "Absence of Ferromagnetism or Antiferromagnetism in One- or Two-Dimensional Isotropic Heisenberg Models," *Physical Review Letters*, vol. 17, pp. 1133–1136, Nov. 1966.

[57] E. Manousakis, "The spin-1/2 Heisenberg antiferromagnet on a square lattice and its application to the cuprous oxides," *Rev. Mod. Phys.*, vol. 63, pp. 1–62, Jan. 1991.

[58] B. Keimer, N. Belk, R. J. Birgeneau, A. Cassanho, C. Y. Chen, M. Greven, M. A. Kastner, A. Aharony, Y. Endoh, R. W. Erwin, and G. Shirane, "Magnetic excitations in pure, lightly doped, and weakly metallic La_2CuO_4," *Phys. Rev. B*, vol. 46, pp. 14034–14053, Dec. 1992.

[59] H. M. Rønnow, D. F. McMorrow, R. Coldea, A. Harrison, I. D. Youngson, T. G. Perring, G. Aeppli, O. Syljuåsen, K. Lefmann, and C. Rischel, "Spin Dynamics of the 2D Spin 1/2 Quantum Antiferromagnet Copper Deuteroformate Tetradeuterate (CFTD)," *Phys. Rev. Lett.*, vol. 87, pp. 037202–037205, June 2001.

[60] B. Dalla Piazza, M. Mourigal, N. B. Christensen, G. J. Nilsen, P. Tregenna-Piggott, T. G. Perring, M. Enderle, D. F. McMorrow, D. A. Ivanov, and H. M. Rønnow, "Fractional excitations in the square-lattice quantum antiferromagnet," *Nature Physics*, vol. 11, pp. 62–68, Jan. 2015.

[61] M. Greven, R. J. Birgeneau, Y. Endoh, M. A. Kastner, M. Matsuda, and G. Shirane, "Neutron scattering study of the two-dimensional spin S=1/2 square-lattice Heisenberg antiferromagnet $Sr_2CuO_2Cl_2$," *Zeitschrift für Physik B Condensed Matter*, vol. 96, pp. 465–477, Dec. 1995.

[62] H. M. Rønnow, D. F. McMorrow, and A. Harrison, "High-Temperature Magnetic Correlations in the 2D S=1/2 Antiferromagnet Copper Formate Tetradeuterate," *Phys. Rev. Lett.*, vol. 82, pp. 3152–3155, Apr. 1999.

[63] J. Rodríguez-Carvajal, "Recent advances in magnetic structure determination by neutron powder diffraction," *Physica B: Condensed Matter*, vol. 192, pp. 55–69, Oct. 1993.

[64] D. Iwanaga, Y. Inaguma, and M. Itoh, "Crystal Structure and Magnetic Properties of B-Site Ordered Perovskite-type Oxides $A_2CuB'O_6$ (A=Ba, Sr;

B′=W, Te)," *Journal of Solid State Chemistry*, vol. 147, pp. 291–295, Oct. 1999.

[65] B. E. Warren, "X-Ray Diffraction in Random Layer Lattices," *Physical Review*, vol. 59, pp. 693–698, May 1941.

[66] A. S. Wills, N. P. Raju, C. Morin, and J. E. Greedan, "Two-Dimensional Short-Range Magnetic Order in the Tetragonal Spinel $Li_2Mn_2O_4$," *Chemistry of Materials*, vol. 11, pp. 1936–1941, July 1999.

[67] Y. J. Uemura, A. Keren, K. Kojima, L. P. Le, G. M. Luke, W. D. Wu, Y. Ajiro, T. Asano, Y. Kuriyama, M. Mekata, H. Kikuchi, and K. Kakurai, "Spin Fluctuations in Frustrated Kagome Lattice System $SrCr_8Ga_4O_{19}$ Studied by Muon Spin Relaxation," *Physical Review Letters*, vol. 73, pp. 3306–3309, Dec. 1994.

[68] P. Mendels, F. Bert, M. A. de Vries, A. Olariu, A. Harrison, F. Duc, J. C. Trombe, J. S. Lord, A. Amato, and C. Baines, "Quantum Magnetism in the Paratacamite Family: Towards an Ideal Kagomé Lattice," *Physical Review Letters*, vol. 98, pp. 077204–077207, Feb. 2007.

[69] S. Vasala, M. Avdeev, S. Danilkin, O. Chmaissem, and M. Karppinen, "Magnetic structure of Sr_2CuWO_6," *Journal of Physics: Condensed Matter*, vol. 26, pp. 496001–496005, Dec. 2014.

[70] T. Aharen, J. E. Greedan, C. A. Bridges, A. A. Aczel, J. Rodriguez, G. MacDougall, G. M. Luke, T. Imai, V. K. Michaelis, S. Kroeker, H. Zhou, C. R. Wiebe, and L. M. D. Cranswick, "Magnetic properties of the geometrically frustrated S=1/2 antiferromagnets, La_2LiMoO_6 and Ba_2YMoO_6, with the B-site ordered double perovskite structure: Evidence for a collective spin-singlet ground state," *Physical Review B*, vol. 81, pp. 224409–224421, June 2010.

[71] K. Kamata, M. Yoshimura, T. Nakamura, and T. Sata, "Synthesis and Properties of Ordered Perovskites $A_2(Ln^{3+}M^{5+})O_6$ (A=Ba, Sr, Ln=Y, Gd, Dy, Er, M=Mo, W)," *Chemistry Letters*, vol. 1, no. 12, pp. 1201–1206, 1972.

[72] L. Katz and R. Ward, "Structure Relations in Mixed Metal Oxides," *Inorganic Chemistry*, vol. 3, pp. 205–211, Feb. 1964.

[73] C. Vineis, P. K. Davies, T. Negas, and S. Bell, "Microwave dielectric properties of hexagonal perovskites," *Materials Research Bulletin*, vol. 31, pp. 431–437, May 1996.

[74] G. Trolliard, N. Ténèze, P. Boullay, and D. Mercurio, "TEM study of cation-deficient-perovskite related $A_nB_{n-1}O_{3n}$ compounds: the twin-shift option," *Journal of Solid State Chemistry*, vol. 177, pp. 1188–1196, Apr. 2004.

[75] H. C. van Duivenboden, H. W. Zandbergen, and D. J. W. IJdo, "Hexabarium titanium(IV) tetraniobate(V); a Rietveld refinement of neutron powder

diffraction data," *Acta Crystallographica Section C Crystal Structure Communications*, vol. 42, pp. 266–268, Mar. 1986.

[76] N. Teneze, P. Boullay, V. Petricek, G. Trolliard, and D. Mercurio, "Structural study of the cation ordering in the ternary oxide $Ba_8Ti_3Nb_4O_{24}$," *Solid State Sciences*, vol. 4, pp. 1129–1136, Sept. 2002.

[77] A. M. Abakumov, G. V. Tendeloo, A. A. Scheglov, R. V. Shpanchenko, and E. V. Antipov, "The Crystal Structure of $Ba_8Ta_6NiO_{24}$: Cation Ordering in Hexagonal Perovskites," *Journal of Solid State Chemistry*, vol. 125, pp. 102–107, Aug. 1996.

[78] W. Wischert, H.-J. Schittenhelm, and S. Kemmler-Sack, "Über Hexagonale Perowskite mit Kationenfehlstellen. V. Strukturbestimmungen an H-$Ba_2Lu_{2/3}\square_{1/3}WO_6$ — eine neue rhomboedrische Stapelvariante mit 18 Schichten," *Zeitschrift für anorganische und allgemeine Chemie*, vol. 448, pp. 119–125, Jan. 1979.

[79] H.-J. Schittenhelm and S. Kemmler-Sack, "Uber geordnete Perowskite mit Kationenfehlstellen Die Systeme Ba_2MgWO_6-$Ba_2Y_{0,67}WO_6$ und Ba_2CaWO_6-$Ba_2Y_{0,67}WO_6$," *Zeitschrift fur anorganische und allgemeine Chemie*, vol. 431, pp. 144–152, June 1977.

[80] "Basic Flowmeter Principles," *published by Matheson Gas*.

[81] W. R. Gardner and G. C. Danielson, "Electrical Resistivity and Hall Coefficient of Sodium Tungsten Bronze," *Physical Review*, vol. 93, pp. 46–51, Jan. 1954.

[82] G. A. Bain and J. F. Berry, "Diamagnetic Corrections and Pascal's Constants," *Journal of Chemical Education*, vol. 85, pp. 532–536, Apr. 2008.

[83] T. Aharen, J. E. Greedan, C. A. Bridges, A. A. Aczel, J. Rodriguez, G. MacDougall, G. M. Luke, V. K. Michaelis, S. Kroeker, C. R. Wiebe, H. Zhou, and L. M. D. Cranswick, "Structure and magnetic properties of the S=1 geometrically frustrated double perovskites La_2LiReO_6 and Ba_2YReO_6," *Physical Review B*, vol. 81, pp. 064436–064444, Feb. 2010.

[84] C. Kittel and H. Kroemer, *Thermal physics*. San Francisco: W. H. Freeman, 2 ed., 1980.

[85] N. N. Greenwood and A. Earnshaw, *Chemistry of the elements*. Oxford ; Boston: Butterworth-Heinemann, 2nd ed ed., 1997.

[86] A. Erickson, S. Misra, G. Miller, R. Gupta, Z. Schlesinger, W. Harrison, J. Kim, and I. Fisher, "Ferromagnetism in the Mott Insulator Ba_2NaOsO_6," *Physical Review Letters*, vol. 99, pp. 016404–016407, July 2007.

[87] M. V. Limaye, J. S. Chen, S. B. Singh, Y. C. Shao, Y. F. Wang, C. W. Pao, H. M. Tsai, J. F. Lee, H. J. Lin, J. W. Chiou, M. C. Yang, W. T.

Wu, J. S. Chen, J. J. Wu, M. H. Tsai, and W. F. Pong, "Correlation between electrochromism and electronic structures of tungsten oxide films," *RSC Advances*, vol. 4, no. 10, pp. 5036–5045, 2014.

[88] R. V. Shpanchenko, L. Nistor, G. Van Tendeloo, J. Van Landuyt, S. Amelinckx, A. M. Abakumov, E. V. Antipov, and L. M. Kovba, "Structural Studies on New Ternary Oxides $Ba_8Ta_4Ti_3O_{24}$ and $Ba_{10}Ta_{7.04}Ti_{1.2}O_{30}$," *Journal of Solid State Chemistry*, vol. 114, pp. 560–574, Feb. 1995.

[89] M. Yoshimura, K. Kamata, and T. Nakamura, "Preparation and Properties of Ordered Perovskites $(LaSr)(MnW)O_6$ and $(LaSr)(MgW)O_6$," *Chemistry Letters*, vol. 1, no. 8, pp. 737–740, 1972.

[90] M. Ducau, K. S. Suh, J. Senegas, and J. Darriet, "Crystal structure and NMR studies of a cubic perovskite: The fluoride $NaBaLiNiF_6$," *Materials Research Bulletin*, vol. 27, pp. 1115–1123, Sept. 1992.

[91] K. Leinenweber and J. Parise, "High-Pressure Synthesis and Crystal Structure of $CaFeTi_2O_6$, a New Perovskite Structure Type," *Journal of Solid State Chemistry*, vol. 114, pp. 277–281, Jan. 1995.

[92] P. M. Woodward, D. E. Cox, T. Vogt, C. N. R. Rao, and A. K. Cheetham, "Effect of Compositional Fluctuations on the Phase Transitions in $(Nd_{1/2}Sr_{1/2})MnO_3$," *Chemistry of Materials*, vol. 11, pp. 3528–3538, Dec. 1999.

[93] M. W. Lufaso and P. M. Woodward, "Jahn–Teller distortions, cation ordering and octahedral tilting in perovskites," *Acta Crystallographica Section B Structural Science*, vol. 60, pp. 10–20, Feb. 2004.

[94] M. T. Anderson and K. R. Poeppelmeier, "Lanthanum copper tin oxide (La_2CuSnO_6): a new perovskite-related compound with an unusual arrangement of B cations," *Chemistry of Materials*, vol. 3, pp. 476–482, May 1991.

[95] M. C. Knapp and P. M. Woodward, "A-site cation ordering in $AA'BB'O_6$ perovskites," *Journal of Solid State Chemistry*, vol. 179, pp. 1076–1085, Apr. 2006.

[96] M. Dion, M. Ganne, and M. Tournoux, "Nouvelles familles de phases $M^IM^{II}{}_2Nb_3O_{10}$ a feuillets "perovskites"," *Materials Research Bulletin*, vol. 16, pp. 1429–1435, Nov. 1981.

[97] A. J. Jacobson, J. W. Johnson, and J. T. Lewandowski, "Interlayer chemistry between thick transition-metal oxide layers: synthesis and intercalation reactions of $K[Ca_2Na_{n-3}Nb_nO_{3n+1}]$ $(3 \leq n \leq 7)$," *Inorganic Chemistry*, vol. 24, pp. 3727–3729, Nov. 1985.